WL-TR-92-1006

AD-A255 855

SCATTERER MODELING/CALIBRATION STUDY

R.J. Marhefka, J.D. Young, N. Akhter, T.J. Brinkley
L.P. Ivrissimtzis, J.S. Gwynne, S.M. Scarborough and B. Chan
THE OHIO STATE UNIVERSITY
ELECTROSCIENCE LABORATORY
1320 KINNEAR ROAD
COLUMBUS, OHIO 43212

June 1992

DTIC
S ELECTE
SEP 2 5 1992
A D

FINAL Report for Period August 1988 – May 1991

Approved for public release; distribution is unlimited.

AVIONICS DIRECTORATE
WRIGHT LABORATORY
AIR FORCE SYSTEMS COMMAND
WRIGHT-PATTERSON AIR FORCE BASE, OHIO 45433-6543

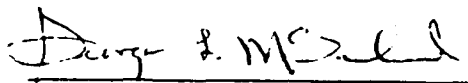**92 9 23 042**

92-25726

NOTICE

When Government drawings, specifications, or other data are used for any purpose other than in connection with a definitely Government-related procurement, the United States Government incurs no responsibility or any obligation whatsoever. The fact that the government may have formulated or in any way supplied the said drawings, specifications, or other data, is not to be regarded by implication, or otherwise in any manner construed, as licensing the holder, or any other person or corporation; or as conveying any rights or permission to manufacture, use, or sell any patented invention that may in any way be related thereto.

This report is releasable to the National Technical Information Service (NTIS). At NTIS, it will be available to the general public, including foreign nations.

This technical report has been reviewed and is approved for publication.

RICHARD J. KOESEL
PROJECT ENGINEER

DONALD H. CAMPBELL, CHIEF
TECHNOLOGY DEVELOPMENT GROUP

GEORGE L. McFARLAND, JR.
ACTG DIRECTOR
MISSION AVIONICS DIVISION
AVIONICS DIRECTORATE

50272-101

REPORT DOCUMENTATION PAGE	1. REPORT NO. WL-TR-92-1006	2.	3. Recipient's Accession No.
4. Title and Subtitle Scatterer Modeling/Calibration Study			5. Report Date June 1992
			6.
7. Author(s) R.J. Marhefka, J.D. Young, N. Akhter, T.J. Brinkley, L.P. Ivrissimtzis, J.S. Gwynne, S.M. Scarborough, B. Chan			8. Performing Org. Rept. No. 721198-6
9. Performing Organization Name and Address The Ohio State University ElectroScience Laboratory 1320 Kinnear Road Columbus, OH 43212			10. Project/Task/Work Unit No. 76220760
			11. Contract(C) or Grant(G) No. (C) F33615-88-C-1792 (G)
12. Sponsoring Organization Name and Address Richard Koesel (513/255-6427) Avionics Directorate (WL/AARM), Wright Laboratory Wright-Patterson AFB, OH 45433-6543			13. Report Type/Period Covered Final/Aug 88–May 91
			14.

15. Supplementary Notes

16. Abstract (Limit: 200 words)

This is the final report on Contract No. F33615-88-C-1792 for Wright-Patterson Air Force Base over the period August 1988 through May 1991. The overall goals and accomplishments are summarized. The goal of this contract is the investigation of monostatic and bistatic polarization and electromagnetic phenomenology at various low and high frequencies such as L, X and Ka bands for the purpose of enhancing the performance of synthetic aperture ground imaging radars for automatic target detection/classification. This is accomplished via measurements and analytic modeling of simple scatterers and complex targets comprising an ensemble of simple scatterers. Specific radar scattering data are obtained in the frequency range 2–18 GHz on scale model targets and at frequencies below 2 GHz for full size targets. In both cases, coherent magnitude and phase signal versus target orientation, frequency and polarization are collected.

17. Document Analysis a. Descriptors
UTD
SCATTERING
MEASUREMENTS

b. Identifiers/Open-Ended Terms

c. COSATI Field/Group

18. Availability Statement A. Approved for public release; Distribution is unlimited.	19. Security Class (This Report) Unclassified	21. No. of Pages 98
	20. Security Class (This Page) Unclassified	22. Price

(See ANSI-Z39.18)   *See Instructions on Reverse*   OPTIONAL FORM 272 (4-77)
Department of Commerce

i

Contents

List of Figures

Chapter 1

Introduction

This is the final report on Contract No. F33615-88-C-1792 for Wright-Patterson Air Force Base over the period August 1988 through May 1991. The overall goals and accomplishments are summarized. Some of the highlights of the major technical findings are presented in the various chapters. More detailed information can be found in the reports and papers listed below.

1.1   Statement of Problem

The overall goal of this program is to assess the use of the polarization response of a scattering object as added information along with modern SAR techniques in order to identify or discriminate a radar target. In particular, the program has three major tasks. First, to provide high quality calibrated measurements on a set of basic targets for the complete scattering matrix and both backscatter and bistatic scattering using The Ohio State University ElectroScience Laboratory (OSU-ESL) compact range. Second, to measure specific scale model targets in the OSU-ESL compact range in the frequency range 2–18 GHz and full-scale targets at the Big Ear range at frequencies below 2 GHz. In both cases, coherent magnitude and phase signal versus target orientation, frequency and polarization are collected. Third, to analytically model the basic targets in order to provide insight into the characteristics of the individual scattering mechanisms. The modeling effort is based on the Uniform Geometrical

Theory of Diffraction (UTD). Computer codes for the various basic targets have resulted.

The basic targets of concern are flat plates, dihedrals, trihedrals, top-hats, "cake pans," bruderhedrals, bi-cones, and toruses. Some of these objects are chosen for their usefulness as calibration targets. It is also assumed that real targets of interest as they appear in Synthetic Aperture Radar (SAR) are composed of similar objects.

1.2 Accomplishments

Modern UTD techniques have been used to study basic shapes applicable to target identification. First order terms related to simpler physical optics approximations, and higher order terms have been developed to model the structures. The higher order terms are important to obtain more complete lower frequency behavior. In some cases correct amplitude information in lower cross section regions is totally lost without this type of component. Potential characteristic "arcs" in the SAR images also can be associated with these terms.

Analysis of the rectangular and triangular dihedral has been completed. A computer code that provides patterns and swept frequency information has been written and validated against method of moments and the above mentioned measurements. It can be used to validate measurements, identify physical mechanisms in the results, perform parametric studies in designing dihedrals of various edge shapes, and conduct component studies of more general real targets.

The analytic techniques have been extended to top-hats and the concave shape of a "cake pan," which can represent a wheel hub. Bruderhedrals and bi-cones have also been studied. Preliminary results for torus shapes, representing tires, have been obtained. Computer codes have been written to validate the analysis. In addition, simpler formulae have been obtained to help provide insight into possible target identification characteristics.

Simple flat plate structures have been extensively studied to obtain amplitude and frequency behavior over wide bands and angles. A much more complete depiction for scattering from the corners has been obtained. In addition, the higher terms that propagate across the plates from corner to edges and corners to corners have been studied. The results have been validated against other analyses and high resolution measurements.

The analytic results obtained have been used to obtain a better understanding of SAR images. They have also been used to help design calibration targets in SAR scenes. The analysis and measurements, help clarify phenomenology pertinent to target identification.

A radar measurement system for obtaining Ultra-Wideband (UWB) scattering data over the 47- to 2000-MHz band has been developed and used on full size ground vehicle targets up to 70 ft long. Data have been gathered on several targets over a wide range of radar look angles.

A technique for calibration of UWB ranges using dihedrals and trihedrals has been developed. The technique has been used for comparison measurements of three diagnostic scattering systems.

A UWB linear imaging process has been developed and implemented. Diagnostic images have been produced for ground vehicles (both models and full size), as well as for several of the fundamental scattering targets which have been analyzed by this study. It has been shown that the images have sufficient resolution and sensitivity to resolve higher order scattering mechanisms, which are the subject of our advances in GTD analysis.

An image windowing algorithm which permits the extraction of the pattern and spectrum of a single scattering mechanism has been developed and demonstrated. The characteristics of several higher order scattering mechanisms have been verified using this algorithm.

3

Details of the above accomplishments and more are summa ed in this report and in the following reports and papers.

The following reports have been generated relative to this contract:

- "Far Zo e Scattering from Rectangular and Triangular Dihedrals in the Principal Plane," by N. Akhter and R. J. Marhefka, Technical Report 721198-1, February 1989. (Also a M.Sc. Thesis)

- "Ultra-Wideband Ra ar Imaging and the Diagnosis of Scattering Centers," by S. M. Scarborough, Technical Report 721198-2, September 1990. (Also a M.Sc. Thesis)

- "An Assessment of Three Experimental Radar Scattering Measurement Systems Operating Below 2 GHz," by J. S. Gwynne, Technical Report 721198-3, March 1991. (Also a M.Sc. Thesis)

- "High Frequency Electromagnetic Scattering by Polygonal Structures," by L. P. Ivrissimtzis and R. J. Marhefka, Technical Report 721198-4, March 1991. (Also a Ph.D. Dissertation)

- " urrent Near the Vertex of a Perfectly Conducting Angular Sector," by T. J. Brinkley and R. J. Marhefka, Technical Report 721198-5, June 1991. (Also a Ph.D. Dissertation)

The foll ving or l papers have been presented in association with this contract:

- "Polarimetric ISAR Imaging to Identify Basic Scattering Mechanisms of Geometrically Complicated Objects," G. Dural, J.D. Young and D.L. Moffatt, 1989 IEEE APS-URSI Meeting, San Jose, California.

- "Comparison of Three Low-Frequency Measurement Techniques and Calculations for Small Dihedral Backscattering," J.S. Gwynne and J.D. Young, 1989 IEEE APS-URSI Meeting, San Jose, California.

4

- "Image Processing for Diagnosis of Dispersive Scattering Centers," S.M. Scarborough and J.D. Young, 1989 IEEE APS-URSI Meeting, San Jose, California.

- "A Study of Scattering from Edge Waves Using High Resolution Radar Images," J.D. Young, 1990 IEEE APS-URSI Meeting, Dallas, Texas.

- "Ultra-Wideband Diagnostic Target Imaging," J.D. Young and S.M. Scarborough, First Los Alamos Symposium on Ultra-Wideband Radar, May 1990.

- "UTD Scattering from Dihedrals," by R. J. Marhefka and N. Akhter," 5th Annual Review, Applied Computational Electromagnetics Society, Naval Postgraduate School, Monterey, California, March 21–24, 1989.

The following written papers have been submitted in association with this contract:

- "Current Near the Vertex of a Perfectly Conducting Angular Sector," by T. J. Brinkley and R. J. Marhefka submitted to *IEEE Transactions on Antennas and Propagation*.

- "Far Zone Field Scattered by a Perfectly Conducting Angular Sector," by T. J. Brinkley and R. J. Marhefka submitted to *IEEE Transactions on Antennas and Propagation*.

1.3 Overview

The following report discusses both the measurements and analysis performed on this contract. Chapter 2 discusses the UTD analysis of a two-dimensional dihedral. The application of UTD to a top-hat and bi-cone is given in Chapter 3. Chapter 4 presents a newly developed diffraction coefficient for the scattering from a corner of a plate. The higher order terms on a plate are briefly discussed in Chapter 5. An ultra-wideband imaging technique for characterizing the frequency and pattern

behavior of local scattering centers is presented in Chapter 6. The calibration and performance of three measurement systems and the various results of simple targets obtained are outlined in Chapter 7. Chapter 8 gives the conclusions.

Chapter 2

Two-Dimensional Dihedral

2.1 Introduction

UTD is used to analyze backscatter and bistatic scattering from an arbitrary angled dihedral. The solution contains interactions of up to third order, which provides excellent results for dihedrals of 60° or greater and for sizes larger than one wavelength in extent. Parallel ray formulation of the UTD is used here for the far zone problem. This means that only edge diffractions, their images, and various combinations of double diffractions are needed. This is a very efficient and accurate means of analyzing the far zone problem. It avoids any integrations and nonphysical "imposed" edge conditions.

The UTD interactions that have been included in the analysis and contained in the 2-D computer code are shown in Figure 2.1. The single interaction fields included are simply edge diffraction (D) terms. The second order interaction fields are the reflected - diffracted (RD), diffracted - reflected (DR), and diffracted - diffracted (DD) (double diffracted) terms. The third order interaction fields are the reflected - reflected - diffracted (RRD), diffracted - reflected - reflected (DRR), reflected - diffracted - reflected (RDR), reflected -diffracted - diffracted (RDD), diffracted - diffracted - reflected (DDR), and diffracted - reflected - diffracted (DRD) terms. Triple diffractions have not been included.

(1) D   (2) RD   (3) DR

(4) DD   (5) RRD   (6) DRR

(7) RDR   (8) RDD   (9) DDR

(10) DRD
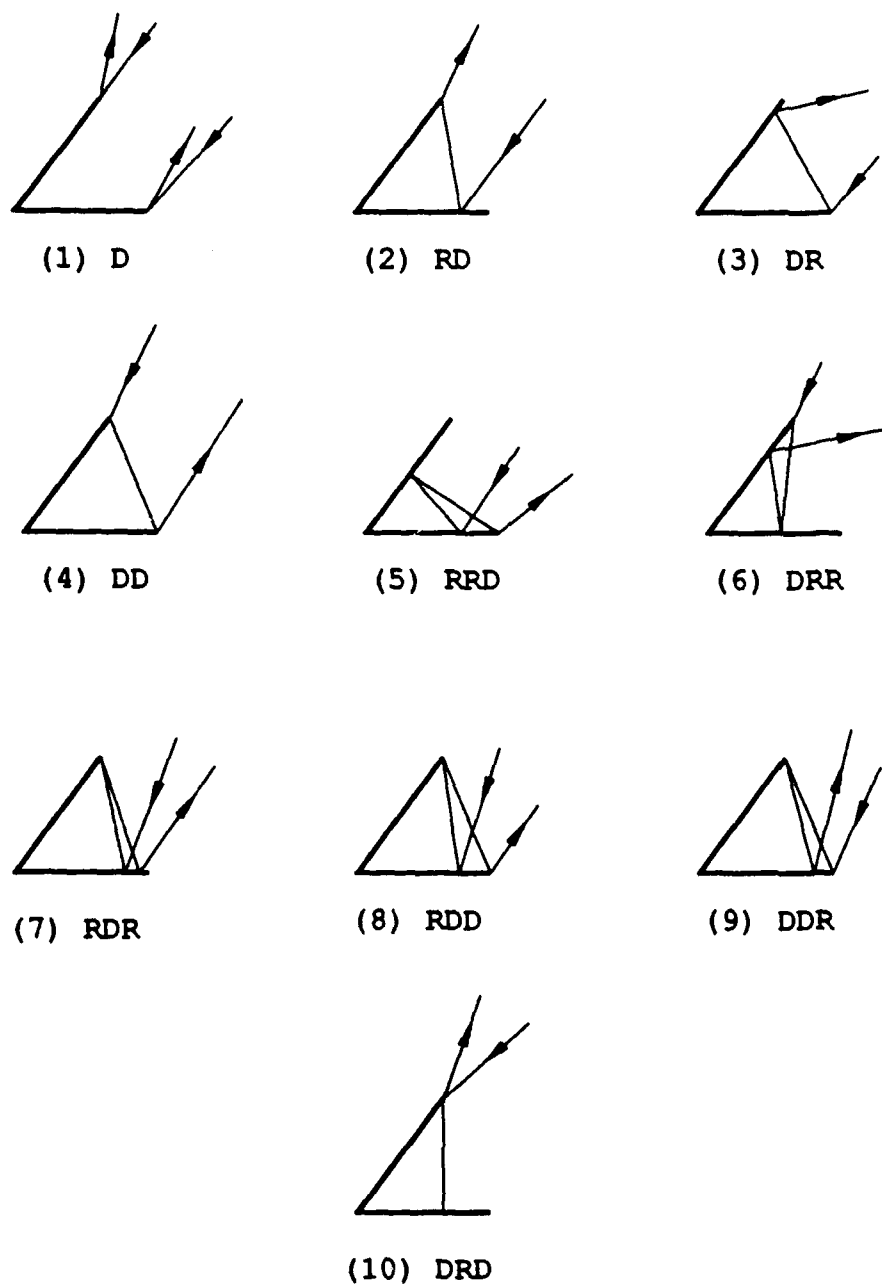
Figure 2.1: The interactions considered.

8

2.2 Basic Dihedral UTD Mechanisms

The main beam of the pattern is formed by the fields from RD and the DR UTD terms along with the single diffracted (D) field from the wedge formed at the junction between the two intersecting strips providing the necessary fields. The double diffraction (DD) across the face of the dihedral can also be important.

For angles derived from Figure 2.2 for bistatic scattering from a general angled dihedral, the diffracted term from the junction is

$$U^D = U^i_{s,h} D_{s,h}. \tag{2.1}$$
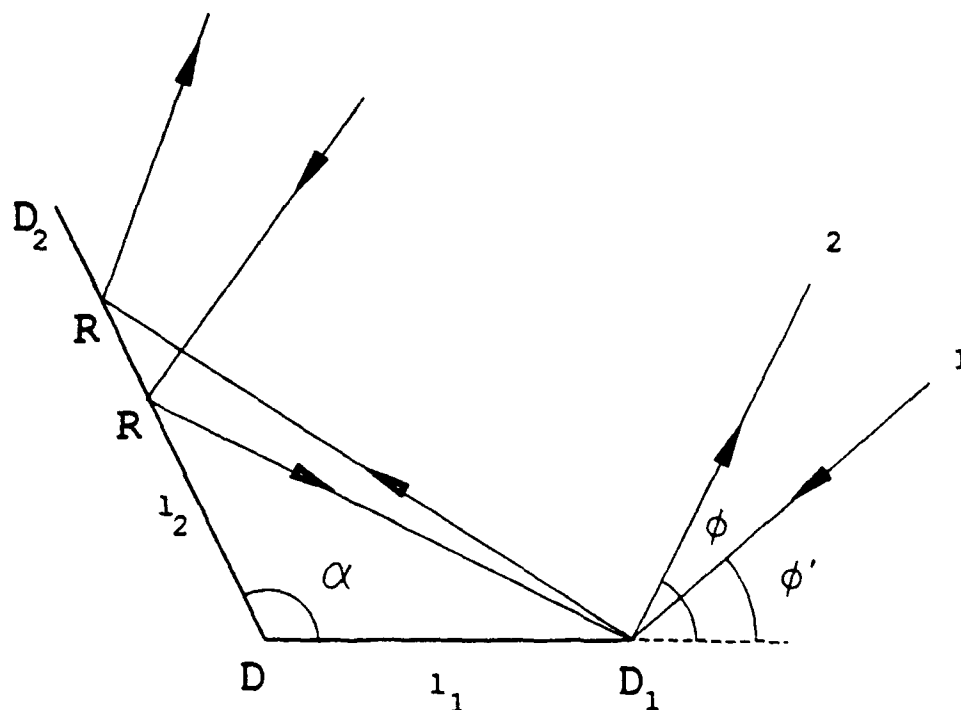
Figure 2.2: The DR and the RD terms (only D_1R and RD_1 shown).

D_1R and RD_1 result due to reflection from strip 2 and the terms D_2R and RD_2 result due to reflection from strip 1. The RD and DR fields are given by

$$U^{D_1R} + U^{RD_1} = U^i_{s,h} R_{s,h} \frac{-e^{-j\pi/4}}{2\sqrt{2\pi k}} \tag{2.2}$$

9

$$\cdot \left[\left(\frac{1}{\cos\left(\frac{\phi+\phi'-2\alpha}{2}\right)} - R_{s,h}\frac{1}{\cos\left(\frac{\phi-\phi'-2\alpha}{2}\right)} \right) e^{2jkl_1 \cos\left(\frac{\phi+\phi'-2\alpha}{2}\right)\cos\left(\frac{\phi-\phi'-2\alpha}{2}\right)} \right.$$

$$\left. + \left(\frac{1}{\cos\left(\frac{\phi+\phi'-2\alpha}{2}\right)} - R_{s,h}\frac{1}{\cos\left(\frac{\phi-\phi'+2\alpha}{2}\right)} \right) e^{2jkl_1 \cos\left(\frac{\phi+\phi'-2\alpha}{2}\right)\cos\left(\frac{\phi-\phi'+2\alpha}{2}\right)} \right]$$

and

$$U^{RD_2} + U^{D_2R} = U_{s,h}^i R_{s,h}\frac{-e^{-j\pi/4}}{2\sqrt{2\pi k}} \tag{2.3}$$

$$\cdot \left[\left(\frac{1}{\cos\left(\frac{\phi+\phi'}{2}\right)} - R_{s,h}\frac{1}{\cos\left(\frac{\phi-\phi'-2\alpha}{2}\right)} \right) e^{2jkl_2 \cos\left(\frac{\phi+\phi'}{2}\right)\cos\left(\frac{\phi-\phi'-2\alpha}{2}\right)} \right.$$

$$\left. + \left(\frac{1}{\cos\left(\frac{\phi+\phi'}{2}\right)} - R_{s,h}\frac{1}{\cos\left(\frac{\phi-\phi'+2\alpha}{2}\right)} \right) e^{2jkl_2 \cos\left(\frac{\phi+\phi'}{2}\right)\cos\left(\frac{\phi-\phi'+2\alpha}{2}\right)} \right]$$

where, the reflection coefficient, $R_{s,h} = \mp 1$.

It is noted that the term D_1R is present in the region

$$\alpha - \frac{\pi}{2} < \phi < \arctan\left[\frac{l_2\sin(\alpha) - l_1\sin(2\alpha)}{l_2\cos(\alpha) - l_1\cos(2\alpha)}\right], \tag{2.4}$$

and D_2R is present in the region

$$\arctan\left[\frac{l_2\sin(\alpha)}{l_1 - l_2\cos(\alpha)}\right] < \phi < \pi - \alpha. \tag{2.5}$$

Also, RD_1 and RD_2 are present in the regions given by Equations (2.4) and (2.5), respectively, with ϕ replaced by ϕ'.

These terms, in general, look quite complicated. In some special cases, they can be reduced to simpler formulas. Consider the case of $\alpha = 90°$. Using

$$\cos\left(\frac{\phi \pm \phi'}{2} \pm \frac{\pi}{2}\right) = \mp \sin\left(\frac{\phi \pm \phi'}{2}\right) \tag{2.6}$$

in Equation (2.2), we have

$$U^{D_1R} + U^{RD_1} = U_{s,h}^i \frac{-e^{-j\pi/4}}{2\sqrt{2\pi k}}$$

$$\cdot \left\{ 2R_{s,h}\frac{\cos\left[2kl_1\sin\left(\frac{\phi+\phi'}{2}\right)\sin\left(\frac{\phi-\phi'}{2}\right)\right]}{\sin\left(\frac{\phi+\phi'}{2}\right)} \right.$$

$$\left. -2j\frac{\sin\left[2kl_1\sin\left(\frac{\phi+\phi'}{2}\right)\sin\left(\frac{\phi-\phi'}{2}\right)\right]}{\sin\left(\frac{\phi-\phi'}{2}\right)} \right\}. \tag{2.7}$$

Close to backscatter, with kl_1 large, the second term is dominant. Thus the above expression may be written as

$$U_{dominant}^{D_1R+RD_1} = U_{s,h}^i e^{j\pi/4} \frac{2l_1}{\sqrt{\lambda}} \sin\left(\frac{\phi+\phi'}{2}\right)$$
$$\cdot \left\{ \frac{\sin\left[2kl_1 \sin\left(\frac{\phi+\phi'}{2}\right) \sin\left(\frac{\phi-\phi'}{2}\right)\right]}{2kl_1 \sin\left(\frac{\phi+\phi'}{2}\right) \sin\left(\frac{\phi-\phi'}{2}\right)} \right\}. \tag{2.8}$$

For the backscatter case with strips of equal length, from Equations (2.3) to (2.5) and (2.8)

$$U_{dominant}^{D_1R+RD_1} = U_{s,h}^i e^{j\pi/4} \frac{2l_1}{\sqrt{\lambda}} \sin(\phi), \quad 0 < \phi < \pi/4. \tag{2.9}$$

and

$$U_{dominant}^{RD_2+D_2R} = U_{s,h}^i e^{j\pi/4} \frac{2l_1}{\sqrt{\lambda}} \cos(\phi), \quad \pi/4 < \phi < \pi/2. \tag{2.10}$$

Notice that for $\phi = 45°$ this result agrees with the well known PO result. Also, observe that there is a slope discontinuity in the dominant UTD (RD and DR terms) at $\phi = 45°$. The DD field across the face of the dihedral balances this slope discontinuity.

The specular from the individual strip faces is produced by D from the ends of the strips and the DR, RD and DRD terms between the strips.

2.3 More Multiple Plate UTD Terms

Depending on the angle of the dihedral and on the bistatic angle, various terms can be important. The RRD and the DRR terms are present when the angle of the dihedral is less than 90°. Of course, these two terms are most significant when the diffraction is along a reflection shadow boundary RSB. Although the RDR term is present for all angles of the dihedral, its significance is greatest when the angle of the dihedral is less than 90° and the diffraction is along a reflection shadow boundary.

For the backscatter case with strips of equal lengths, based on simple reflection concepts, the order of interactions required to get the pattern between the strips

11

is the largest integer whose magnitude does not exceed $\left(\frac{180°}{\alpha}\right)$. Thus, for $\alpha = 60°$, third order terms are required to get the pattern between the strips. Figure 2.3 shows how only the third order terms for a dihedral of 60° combine to give the correct result between the strips. Figure 2.4 compares the Method of Moments results with that of the UTD computer code (with all terms present) for a dihedral of 60°. Notice that the discontinuity at $\phi = 60°$ in Figure 2.3 and Figure 2.4 is due to the triply diffracted field which has not been included in the computer code. Our formulation indicates that for $\alpha = 45°$, fourth order interactions are required. Since the UTD computer code does not take into account the fourth order interactions, we expect no agreement of the results between the strips in this case. This is shown in Figure 2.5. However, even for this case, notice the excellent agreement for ϕ greater then 50°. Thus, for the terms present in the computer code, the pattern would degrade gracefully between the strips for α less then 60°. As the angle of the dihedral becomes smaller, more terms are required to give the correct result between the strips and a "cavity" effect results.

2.4 Results of Rectangular Dihedral

In this section, the theory and computer code are validated by comparing the UTD results to 2-D method of moments results. In order to calculate the backscatter results, a slight bistatic angle is used to avoid numerical limit concerns on the computer. Method of Moments is chosen to validate the results as an independent check since both are two-dimensional. Fairly large sized dihedrals can be calculated using method of moments in the 2-D case. In 3-D, limits on computer memory restrict the size of dihedral that can be analyzed using method of moments. A 9″ (22.86 cm) 2-D dihedral is analyzed at 2 GHz and 10 GHz meaning the dihedral is 1.52 and 7.62 wavelengths on a side, respectively. All the patterns are normalized to dB relative to a square meter, that is, a two-dimensional cross section.
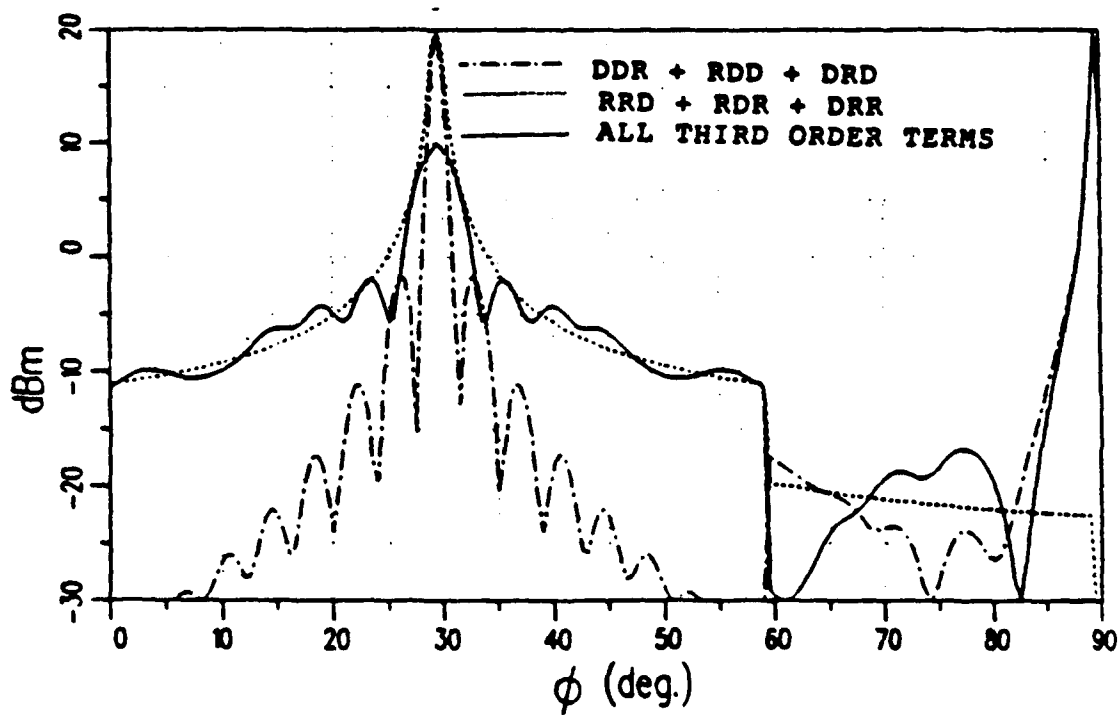
Figure 2.3: Only third order terms give a continuous result for 9″ 60° rectangular dihedral at 10 GHz for a horizontally polarized field (backscatter).

13
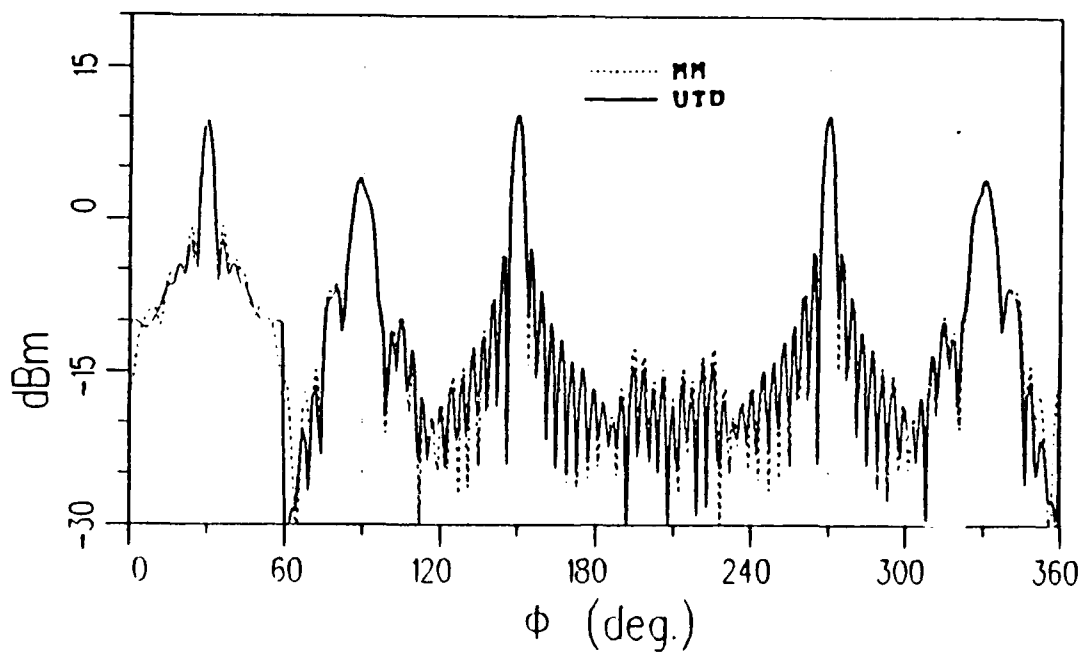
Figure 2.4: Backscatter field from a 9″ 60° rectangular dihedral at 10 GHz for a horizontally polarized field.
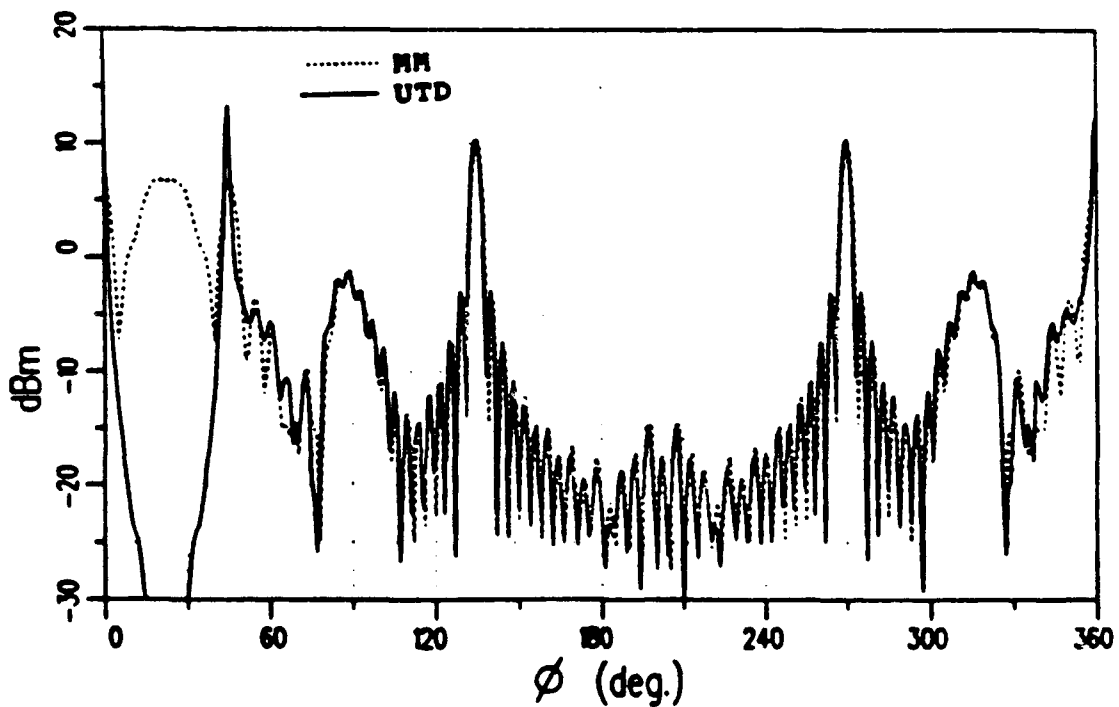
Figure 2.5: Backscatter field from a 9″ 45° rectangular dihedral at 10 GHz for a horizontally polarized field.

For the vertically polarized incident field, the backscatter from a 90° dihedral, Figure 2.6 shows the singly diffracted (D) term, DR, and RD terms. Figure 2.7 shows the D, RD and DR terms combined, the DRD term, and the DD term. This is all that is required to get the complete result for the 90° dihedral. Figure 2.13 shows the result obtained by the D, DR, RD, DRD, and DD terms combined.

From here on, the UTD results contain all of the terms discussed above. For the backscatter case, from Geometrical Optics, a main beam is expected when the angle of the dihedral is such that $\left(\frac{180°}{\alpha}\right)$ is an integer. This is clearly evident in Figures 2.4, 2.5, and 2.7. Also, as the angle of the dihedral diverts from α which makes $\left(\frac{180°}{\alpha}\right)$ an integer, the main beam breaks up. Figures 2.8 and 2.9 show backscatter results for $\alpha = 85$ and 95 degrees, respectively, with the incident field horizontally polarized. As expected, the main beam of the pattern for $\alpha = 90°$ breaks up as α is decreased or increased.

The backscattered field for the 2-GHz case is shown in Figure 2.10 for horizontal polarization and in Figure 2.11 for vertical polarization. The 10-GHz backscatter case is shown in Figures 2.12 and 2.13 for the horizontal and vertical polarizations, respectively. Patterns for a fixed bistatic angle of 90° are shown next. The 2-GHz case is shown in Figure 2.14 for horizontal polarization and in Figure 2.15 for vertical polarization. The 10-GHz patterns are shown in Figures 2.16 and 2.17 for horizontal and vertical polarization, respectively. In all cases, the agreement is excellent. The small dihedrals have slightly more disagreement because the higher order interactions are more important. It is assumed even better agreement and/or smaller sized dihedrals could be achieved and/or analyzed by including more interactions. For engineering accuracy, however, this would not seem necessary.

2.5 Conclusion

The UTD formulation gives excellent results for the rectangular dihedral in the principal plane. For backscatter, the number of interactions required to get the
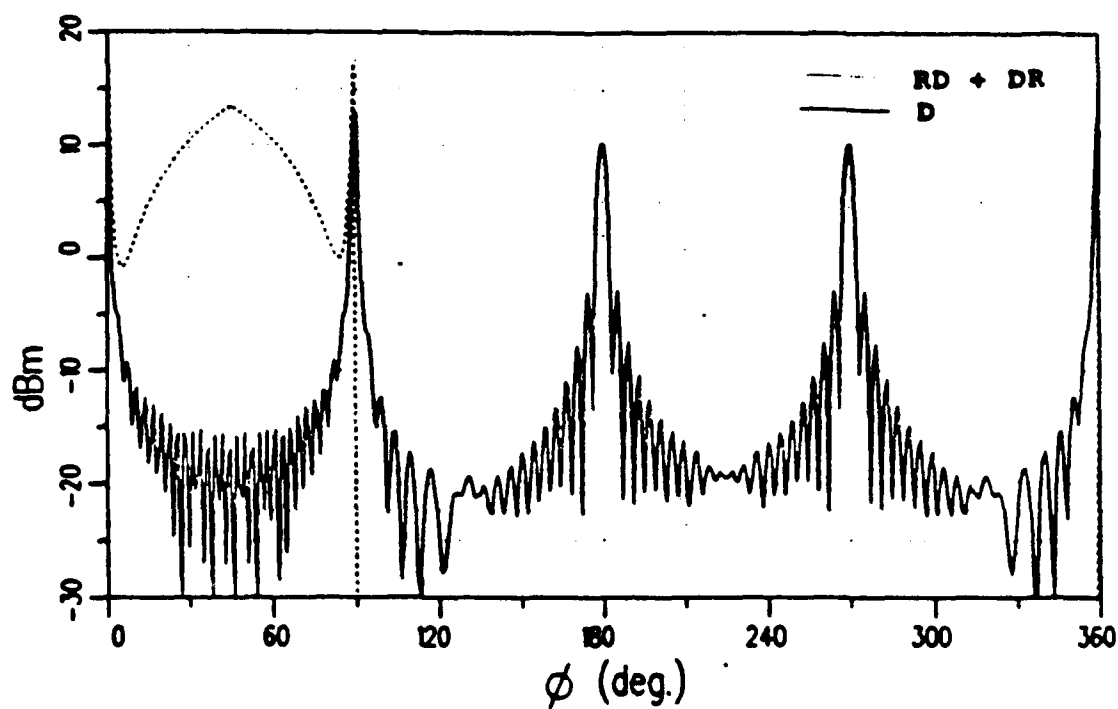
Figure 2.6: D, DR, and RD terms for the backscatter for 90° rectangular dihedral at 10 GHz (vertically polarized).
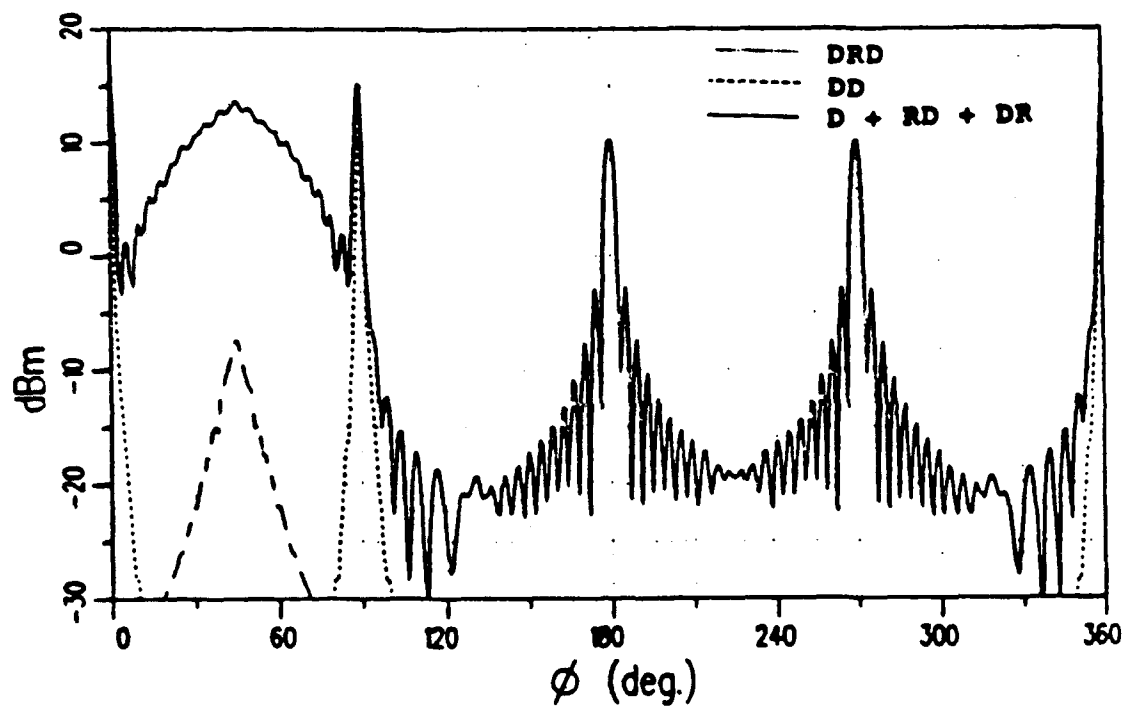
Figure 2.7: Same case as Figure 2.6 with DRD, and DD terms added.

16
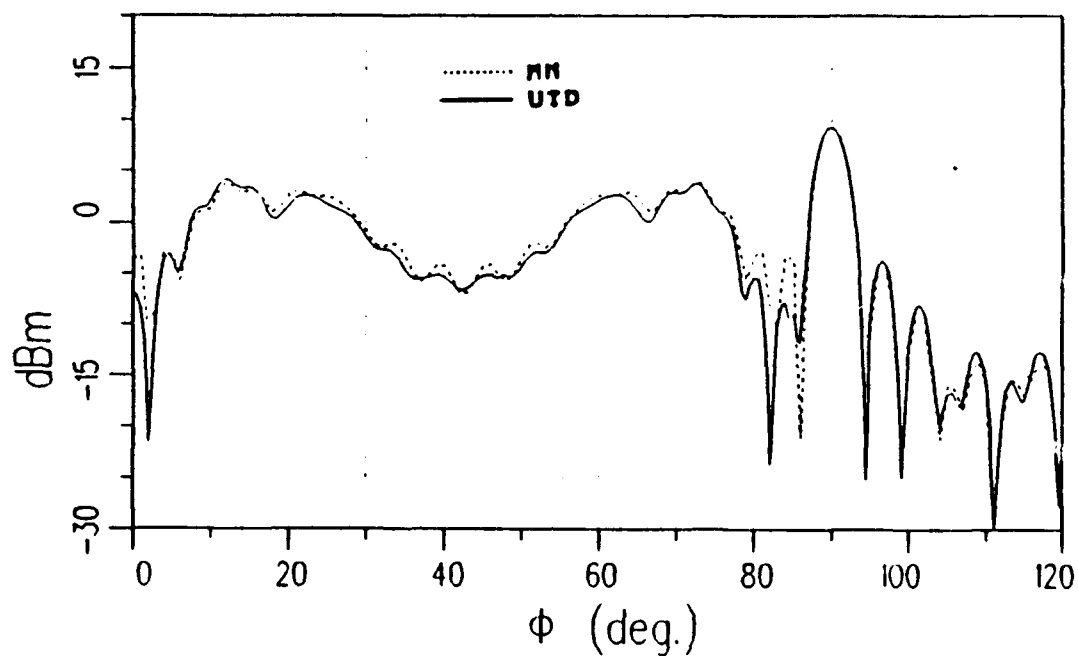
Figure 2.8: Backscatter from 85° rectangular dihedral at 10 GHz for horizontally polarized field.
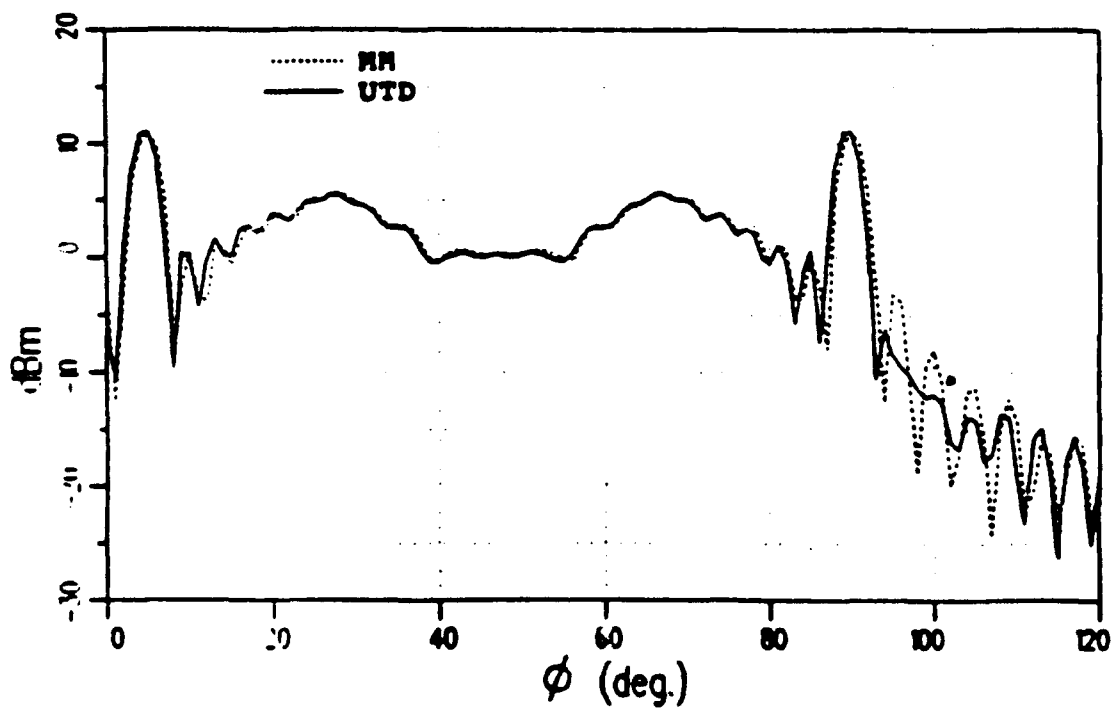
Figure 2.9: Backscatter from 95° rectangular dihedral at 10 GHz for horizontally polarized field.

17
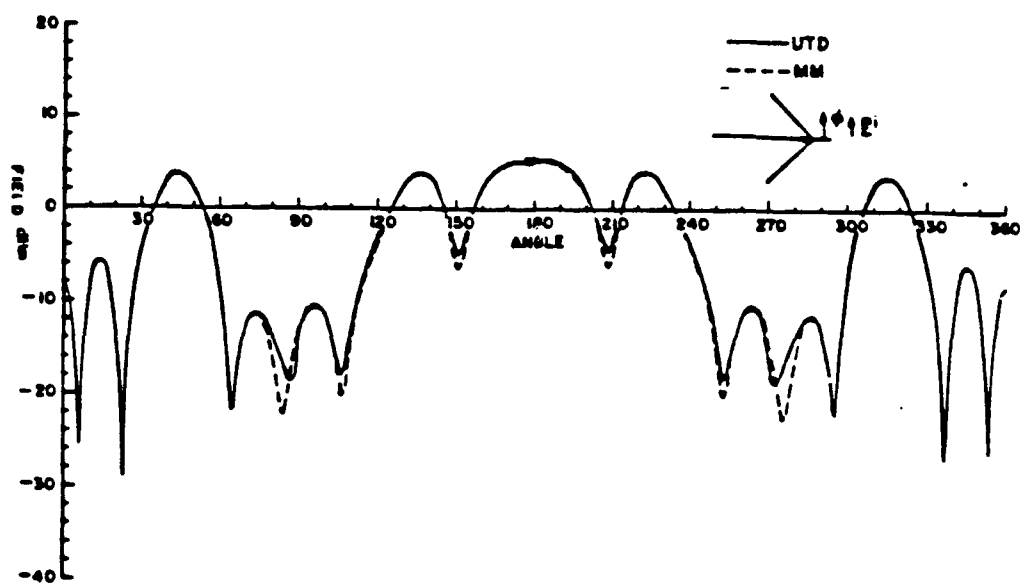
Figure 2.10: Backscatter at 2 GHz for horizontally polarized field.
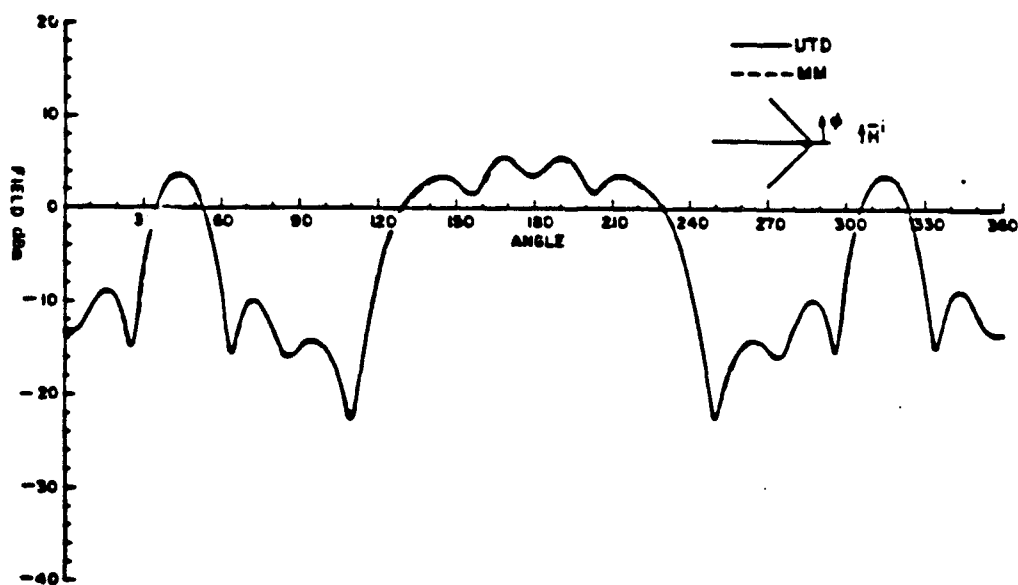
Figure 2.11: Backscatter at 2 GHz for vertically polarized field.
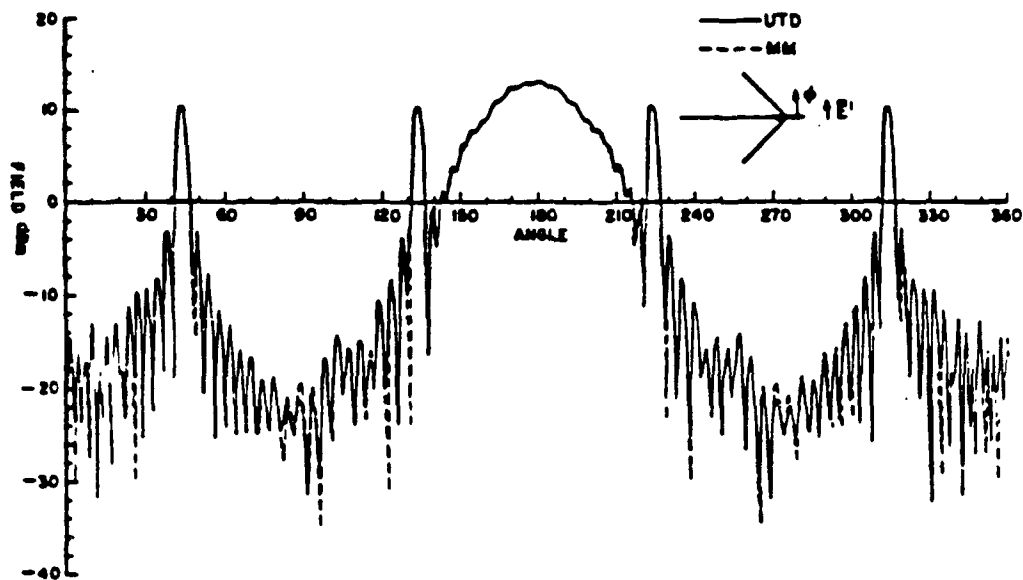
Figure 2.12: Backscatter at 10 GHz for horizontally polarized field.
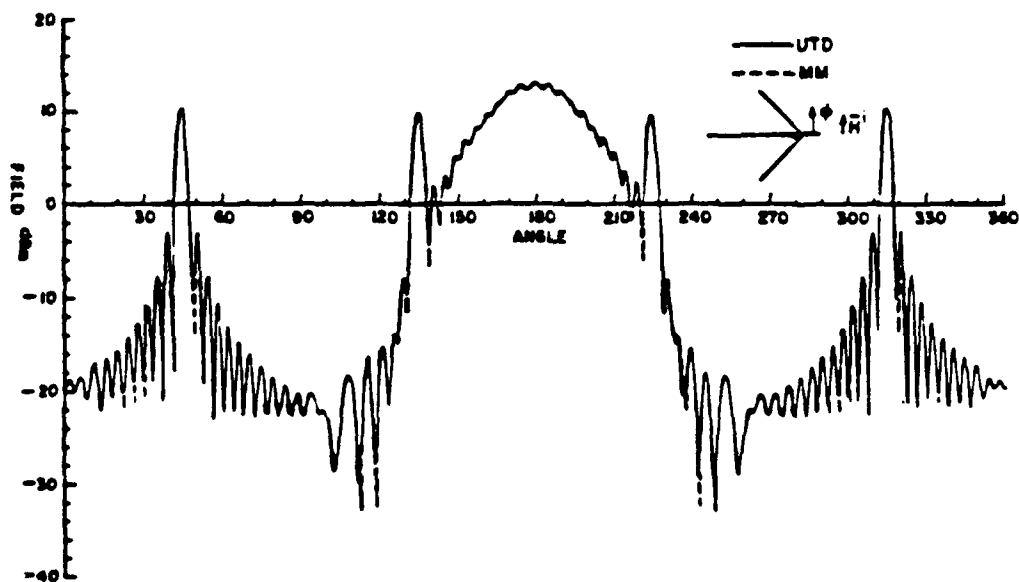
Figure 2.13: Backscatter at 10 GHz for vertically polarized field.

19
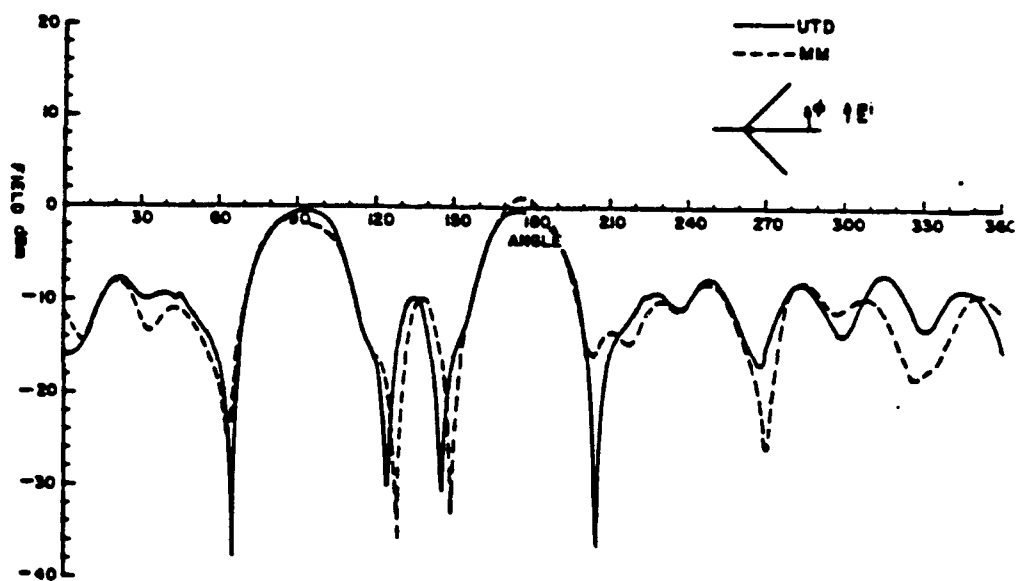
Figure 2.14: 90° bistatic field at 2 GHz for horizontally polarized field.
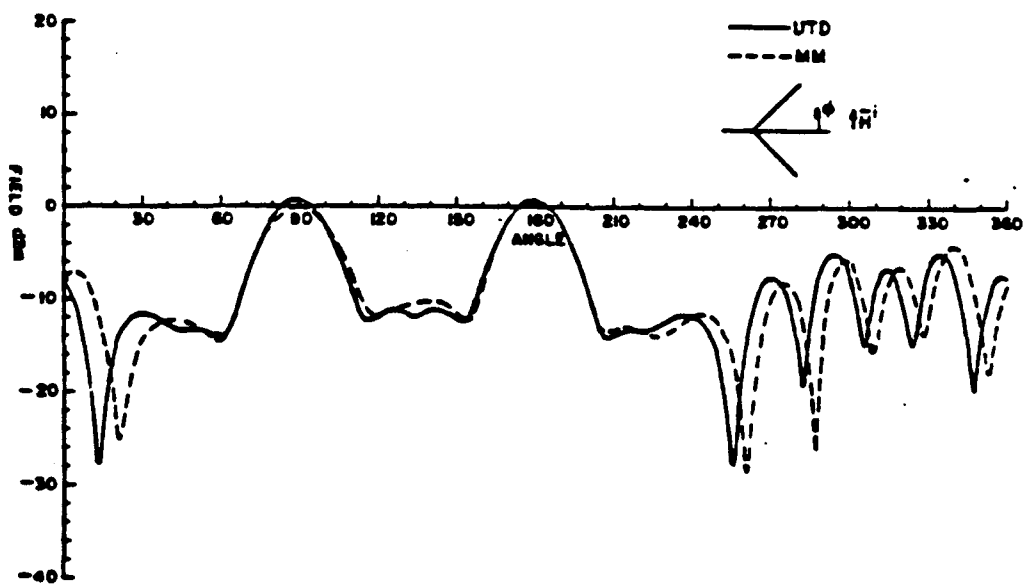
Figure 2.15: 90° bistatic field at 2 GHz for vertically polarized field.

20
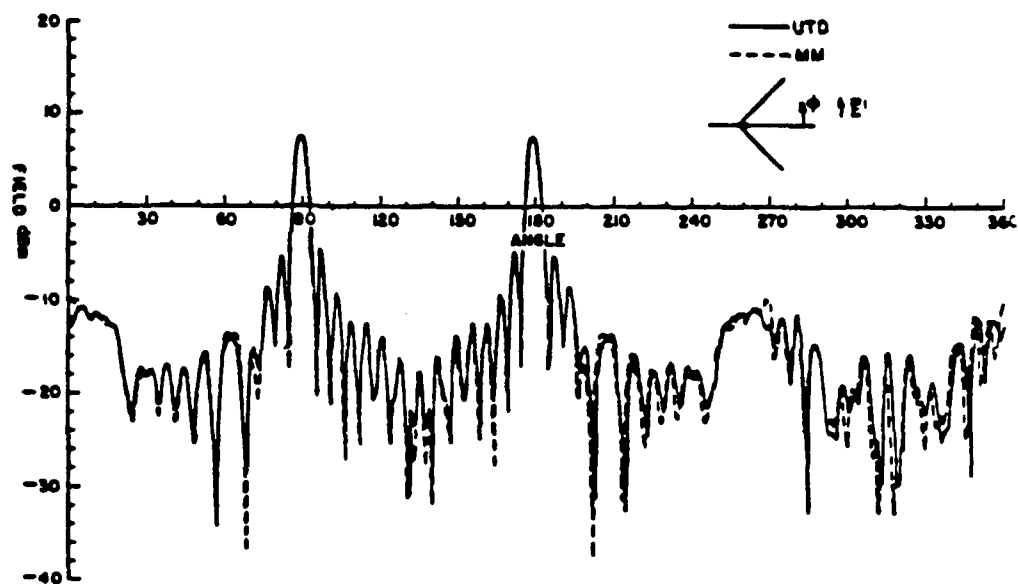
Figure 2.16: 90° bistatic field at 10 GHz for horizontally polarized field.
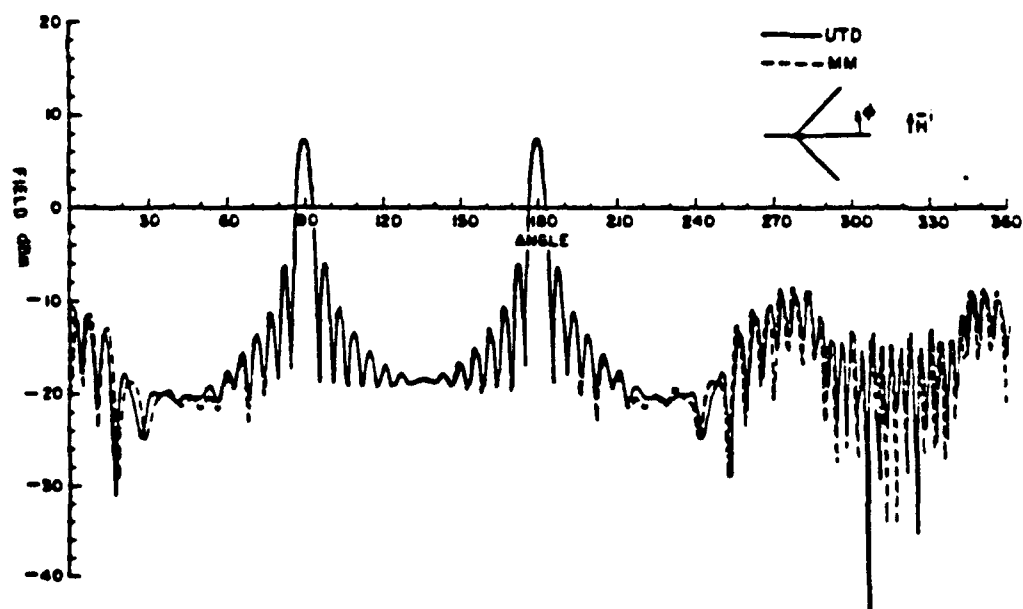
Figure 2.17: 90° bistatic field at 10 GHz for vertically polarized field.

21

complete pattern for a dihedral of angle α is found to be the integral value of $\left(\frac{180°}{\alpha}\right)$. For bistatic scattering, the number of interactions required will be less than or equal to that for the backscatter case. Since the computer code developed for this analysis contains interactions of up to third order, our results are found to be valid for backscatter for dihedrals of 60° or greater. This solution is expected to degrade gracefully between the strips for dihedrals of less than 60°. In general, as the angle of the dihedral diverts from α which makes the $\left(\frac{180°}{\alpha}\right)$ an integer, the main beam amplitude breaks up rapidly.

Chapter 3

Top-Hats and Bi-Cones

3.1 Introduction

Due to the localized nature of high frequency scattering, the solution to complex structures may be modeled as a superposition of scattered fields from simpler shapes. The object of this research has been to find far zone backscatter and bistatic scattered fields from some of the most common shapes. This requires second and higher order interactions to get accurate results over a wide range of angles. For these shapes, the most important higher order interactions have been determined. Where possible, the expressions will be simplified to show the connection between the UTD results and the more classical PO approximations.

The two-dimensional dihedral, studied in detail in [1], is one of the simplest of such shapes. The result of the two-dimensional dihedral may be modified by curvature and caustic corrections to get results for the top-hat, bi-cone, bruderhedral, cake pan, et cetera. Other shapes that have been studied are the donut and trihedral.

Ray techniques, like the Geometrical Theory of Diffraction, predict infinite fields at the caustics. The occurrence of these caustics requires the erroneous field infinities be "corrected" with caustic correction functions which blend the wide-angled predictions smoothly into the correct value at the caustic. Caustic corrections of the second and higher order are required to get accurate results for the shapes mentioned.

Caustic corrections for the second and higher order terms have been investigated in the context of UTD.

The solutions to the top-hat and the bi-cone are discussed in Sections 3.2 and 3.3, respectively. The curvature modifications and the caustic corrections to the two-dimensional solution are shown to give appropriate results when compared with the body of revolution results, even for very electrically small targets.

3.2 Top-Hat

3.2.1 Introduction

The 2-D dihedral result of Reference [1] may be used to get 3-D results for a wide variety of problems. The solution of the triangular dihedral in the principal plane is also shown in [1]. The solution to the top-hat problem is discussed in this report. A few modifications are required to the UTD 2-D analysis of the dihedral. Analytic results are validated against body of revolution results. Also, for backscatter, a dominant UTD result is shown to be valid in all regions and is reasonably simple to program. The parameters for the top-hat are shown in Figure 3.1.

3.2.2 Modifications Required

Basically rim caustic correction and spread factors are required to modify the 2-D dihedral solution to give the solution for the top-hat. In Reference [1], the most dominant terms for the 90° dihedral are found to be diffraction, diffracted-reflected (DR), reflected-diffracted (RD), and diffracted-reflected-diffracted (DRD). The dominant contribution from these terms will be used to get the result for the top-hat.

3.2.3 Theoretical Background

In addition to the background information present in Reference [1], we need information on the rim caustic correction. For the backscatter case, when the two diffractions are occurring from the same point (as in the DRD case), the double

24
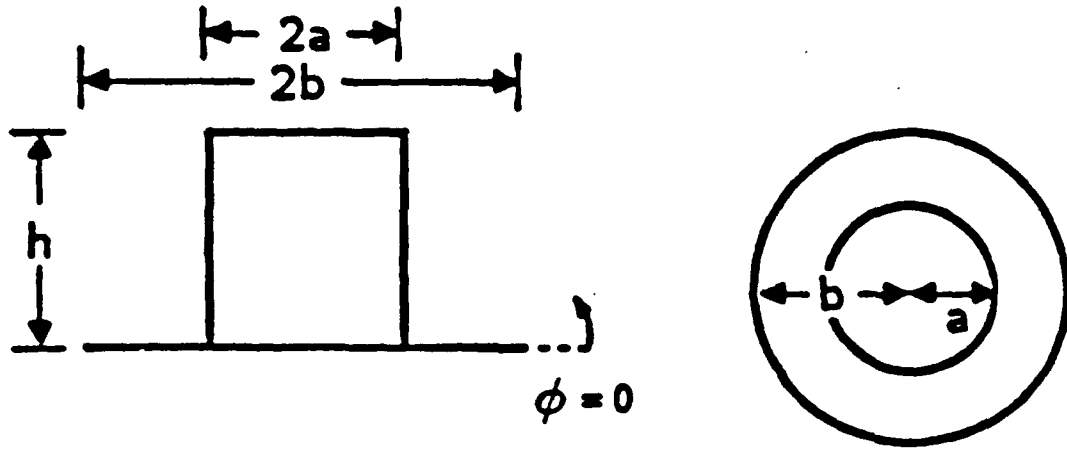
Figure 3.1: Top-hat geometry.

diffraction formulation can be simplified. The simplified equations are shown below, in Section 3.2.4.

3.2.4   Rim Caustic Correction

Details of the single diffraction rim caustic correction are shown in References [2] and [3]. Basically, a half rim is associated with each stationary point. The stationary points being the two diffraction points outside the caustic region. To correct for the rim caustic the regular diffraction coefficient is modified by a transition function. This result goes to the diffraction point solution outside the caustic region, making it a uniform solution. The ''ified diffraction coefficient is given as

$$D_{s,h} = \frac{-e^{-j\pi/}}{2n\sqrt{2\pi k}} \left[\cot\left(\frac{\pi + \beta^-}{2n}\right) + \cot\left(\frac{\pi - \beta^-}{2n}\right) \right.$$
$$\left. \mp \left\{ \cot\left(\frac{\pi + \beta^+}{2n}\right) + \cot\left(\frac{\pi - \beta^+}{2n}\right) \right\} \right] T_c(U), \qquad (3.1)$$

where

$$\beta = \beta^{\pm} = \phi \pm \phi', \qquad (3.2)$$

25

$$T_e(U) = \frac{1}{\pi} f_o(U) \sqrt{\frac{\pi U}{2}} e^{-j(U-\frac{\pi}{4})} \tag{3.3}$$

and

$$f_o(U) = \pi \left[\frac{2}{\pi} - H_1(U) + j J_1(U) \right]. \tag{3.4}$$

J_1 and H_1 are the first order Bessel and Struve functions, respectively. Also,

$$U = ka\hat{n}_e \bullet (\hat{r} + \hat{r}'). \tag{3.5}$$

The transition function is $T_e(U)$. k is the wave number, a and $\hat{n}_e$ are the radius of curvature and the normal to the edge at the point of diffraction, and $\hat{r}$ and $\hat{r}'$ are the directions to the source and the receiver, respectively. The transition function has small and large argument forms given as:

for $|U| << 1$

$$T_e(U) \approx \sqrt{\frac{\pi U}{2}} e^{-j(U-\frac{\pi}{4})} \left\{ \frac{\pi}{2} - \frac{2U^2}{3\pi} \left(1 - \frac{U^2}{15} \right) + j\frac{U}{2} \left(1 - \frac{U^2}{8} \right) \right\} \tag{3.6}$$

for $|U| >> 1$

$$T_e(U) \sim 1 + \frac{j3}{8U} - \frac{1}{U}\sqrt{\frac{2}{\pi U}} e^{-j(U-\frac{\pi}{4})} + \frac{15}{128U^2} - \frac{j105}{1024U^3} \tag{3.7}$$

It is important to note when U is negative, the negative branch of the square root is selected.

3.2.5 Double Diffraction

Details of double diffraction formulation used here are presented in [4]. For the backscatter case when the two diffractions occur from the same point and $a_p = a_q$, the double diffraction equations for P_s and P_h can be simplified. We have

$$P_s(\Phi, n, d) = \frac{1}{8\pi j n^1} \frac{a^2}{\sin^4(\frac{\Phi}{2n})}$$
$$\cdot\ d \left[\left(j + \frac{1}{2kda} \right) F[kda] - j \right] \left(\frac{e^{-jkd}}{\sqrt{d}} \right), \tag{3.8}$$

26

for a TM plane wave (with the electric field parallel to the wedge). For a TE plane wave (with the electric field perpendicular to the wedge),

$$P_h\left(\Phi, n, d\right) = -\frac{1}{4\pi j n^2} \cot^2\left(\frac{\Phi}{2n}\right)$$
$$\cdot \, da\left[\left(j - \frac{1}{2kda}\right) F[kda] - j\right]\left(\frac{e^{-jkd}}{\sqrt{d}}\right). \tag{3.9}$$

These equations are used to get the dominant contribution from the DRD terms of the side and top of the top-hat. All the remaining equations remain unchanged and are given in Reference [1].

3.2.6 Dominant Result

As mentioned above the dominant result is obtained from the diffracted, DR, RD, and DRD terms. We will use the exact expressions for all the terms, except for the case of DRD where only the discontinuous term is considered.

3.2.7 D, RD, DR, and DRD Terms

The expressions shown below are for backscatter from a top-hat of parameters given by Figure 3.1. These expressions are valid for $-90° < \phi < 90°$ unless otherwise stated. Of course by symmetry, the result for the other side may be obtained.

The diffracted terms from the disk for the right side is given by

$$U_{right}^{D_1} = U_{s,h}^i \frac{-e^{-j\pi/4}}{2\sqrt{2\pi k}}\left[1 - R_{s,h}\frac{1}{\cos\left(\phi\right)}\right]$$
$$\cdot \, T_e\left(2kb\cos\left(\phi\right)\right)\sqrt{\frac{b}{2\cos\left(\phi\right)}}\, e^{j2kl\cos(\phi)} \tag{3.10}$$

and for the left side

$$U_{left}^{D_1} = U_{s,h}^i \frac{-e^{-j\pi/4}}{2\sqrt{2\pi k}}\left[1 + R_{s,h}\frac{1}{\cos\left(\phi\right)}\right]$$
$$\cdot \, T_e\left(-2kb\cos\left(\phi\right)\right)\sqrt{\frac{b}{2\cos\left(\phi\right)}}\, e^{j\frac{\pi}{2}}e^{j2kl\cos(\phi)}$$
$$\cdot \, e^{-j4kb\cos(\phi)} \, ; \, \left\{\begin{array}{l} -90° < \phi < 0° \\ \arctan\left[\frac{h}{l}\right] < \phi \end{array}\right. \tag{3.11}$$

27

where $R_{s,h} = \mp 1$ and

$$U_{s,h} = \begin{cases} E & \text{, E field perpendicular to the pattern plane} \\ H & \text{, H field perpendicular to the pattern plane.} \end{cases} \qquad (3.12)$$

The diffracted terms from the top of the cylinder from the right side is

$$\begin{aligned}
U_{right}^{D_2} &= U_{s,h}^i \frac{2e^{-j\pi/4}\sin\left(\frac{2\pi}{3}\right)}{3\sqrt{2\pi k}} \\
&\quad \cdot \left[\frac{1}{\cos\left(\frac{2\pi}{3}\right)-1} + R_{s,h}\frac{1}{\cos\left(\frac{2\pi}{3}\right)-\cos\left(\frac{2\pi+4\phi}{3}\right)}\right] \\
&\quad \cdot T_e\left(2ka\cos\left(\phi\right)\right)\sqrt{\frac{a}{2\cos\left(\phi\right)}}\,e^{j2kh\sin(\phi)} \quad ; \\
&\qquad -\arctan\left[\frac{h}{l}\right] < \phi \qquad (3.13)
\end{aligned}$$

and for the left side

$$\begin{aligned}
U_{left}^{D_2} &= U_{s,h}^i \frac{2e^{-j\pi/4}\sin\left(\frac{2\pi}{3}\right)}{3\sqrt{2\pi k}} \\
&\quad \cdot \left[\frac{1}{\cos\left(\frac{2\pi}{3}\right)-1} + R_{s,h}\frac{1}{\cos\left(\frac{2\pi}{3}\right)-\cos\left(\frac{4\phi}{3}\right)}\right] \\
&\quad \cdot T_e\left(-2ka\cos\left(\phi\right)\right)\sqrt{\frac{a}{2\cos\left(\phi\right)}}\,e^{j\frac{\pi}{2}} \\
&\quad \cdot e^{j2kh\sin(\phi)}e^{-j4ka\cos(\phi)} \quad ; \quad 0 < \phi \qquad . \qquad (3.14)
\end{aligned}$$

The diffraction reflection (D_1 refers to diffraction from the edge of the disk and R refers to the reflection from the cylindrical surface) terms are given by

$$\begin{aligned}
U^{D_1R} + U^{RD_1} &= U_{s,h}^i \frac{-e^{-j\pi/4}}{2\sqrt{2\pi k}} \\
&\quad \cdot \left\{2R_{s,h}\frac{1}{\sin\left(\phi\right)} - j4kl\sin\left(\phi\right)\right\} \\
&\quad \cdot \sqrt{\frac{a}{2\cos\left(\phi\right)}} \quad ; \quad 0 < \phi < \arctan\left[\frac{h}{l}\right] \qquad (3.15)
\end{aligned}$$

and (D_2 refers to diffraction from the top and R refers to the reflection from the disk)

$$U^{RD_2} + U^{D_2R} = U_{s,h}^i \frac{e^{-j\pi/4}}{\sqrt{2\pi k}}T_e\left(2ka\cos\left(\phi\right)\right)$$

28

$$\cdot \left\{ R_{s,h} \frac{4 \sin\left(\frac{2\pi}{3}\right)}{3\left[\cos\left(\frac{2\phi}{3}\right) - \cos\left(\frac{4\phi}{3}\right)\right]} + j2kh\cos(\phi) \right\}$$

$$\cdot \sqrt{\frac{a}{2\cos(\phi)}} \quad ; \quad \arctan\left[\frac{h}{l}\right] < \phi < \frac{\pi}{2} \qquad . \qquad (3.16)$$

For the DRD term, only the dominant term is retained for the joined wedge solution. The dominant DRD term from the side of the top-hat is

$$U_{side}^{DRD} = R_{s,h} U_{s,h}^{i} P_{s,h} \left(\Phi = \phi, n = 2, d = 2l\right)$$

$$\cdot \sqrt{\left(\frac{\rho_1}{\rho_1 + l}\right)\left(\frac{\rho^r}{\rho^r + l}\right)\rho_2} \; e^{j2kl\cos(\phi)} \qquad (3.17)$$

where

$$\rho_1 = \frac{b}{\cos(\phi) - 1} \qquad (3.18)$$

$$\rho^r = \frac{(l + \rho_1)a}{a + 2(l + \rho_1)} \qquad (3.19)$$

$$\rho_2 = \frac{b(l + \rho^r)}{b + (\cos(\phi) - 1)(l + \rho^r)} \qquad (3.20)$$

and $P_{s,h}(\Phi, n, d)$ is given by Equation (3.8) and (3.9). The dominant DRD term from the right side of the top of the top-hat is

$$U_{top,right}^{DRD} = R_{s,h} U_{s,h}^{i} P_{s,h} \left(\Phi = \frac{\pi}{2} - \phi, n = 2, d = 2h\right)$$

$$\cdot T_e\left(2ka\cos(\phi)\right) \sqrt{\frac{a^2}{2\left(a + h\cos(\phi)\right)\cos(\phi)}}$$

$$\cdot e^{j2kh\sin(\phi)} \quad ; \quad -\arctan\left[\frac{h}{l}\right] < \phi \qquad . \qquad (3.21)$$

The dominant DRD term from the left side of the top of the top-hat is

$$U_{top,left}^{DRD} = R_{s,h} U_{s,h}^{i} P_{s,h} \left(\Phi = \phi - \frac{\pi}{2}, n = 2, d = 2h\right)$$

$$\cdot T_e\left(-2ka\cos(\phi)\right) \sqrt{\frac{a^2}{2\left(a + h\cos(\phi)\right)\cos(\phi)}} \; e^{j\frac{\pi}{2}}$$

$$\cdot e^{j2kh\sin(\phi)} e^{j4ka\cos(\phi)} \quad ; \quad 0 < \phi \qquad . \qquad (3.22)$$

29

3.2.8 Peak of the Top-Hat

Along the axis of the top-hat, the cotangent terms of the diffraction coefficients that tend to "blow up" combine to give the dominant result. Not surprisingly, the dominant result obtained is exactly as one would predict from physical optics.

As expected, the reflection boundary cotangent terms of the diffraction from the upper face of the disk (obtained from Equations (3.10) and (3.11)) give the area of the disk. The reflection boundary cotangent terms from the diffraction from the end cap of the upper face of the cylinder (obtained from Equations (3.13) and (3.14)) give the area of the end cap. The incident boundary cotangent terms of the curved face from DR, RD and from DRD (obtained from Equations (3.16), (3.21) and (3.22)) give the negative area of the end cap. Thus the apparent "infinities" combine to give a result equal to the area of the disk minus the area of the end cap of the cylinder plus the area of the end cap of the cylinder with the phase accounting for twice the electrical distance of the cylinder. The RCS along the axis of the top-hat is appropriately given as

$$\sigma^{po}_{top,hat} = 4\pi \left| \frac{\pi(b^2 - a^2)}{\lambda} + \frac{\pi a^2}{\lambda} e^{-jk2h} \right|^2 \qquad (3.23)$$

3.2.9 Results

Figures 3.2 and 3.3 show the results obtained for the horizontal and vertical polarization, respectively, by the UTD computer code and the Body of Revolution code at 10 GHz for a = 2 in., b = 4 in., and h = 4 in. top-hat. The results compare very well.

3.3 The Bi-Cone

3.3.1 Introduction

A solution for the bi-cone is sought by using the UTD 2-D solution of the dihedral discussed in Reference [1]. The parameters for the bi-cone are shown in Figure 3.4.
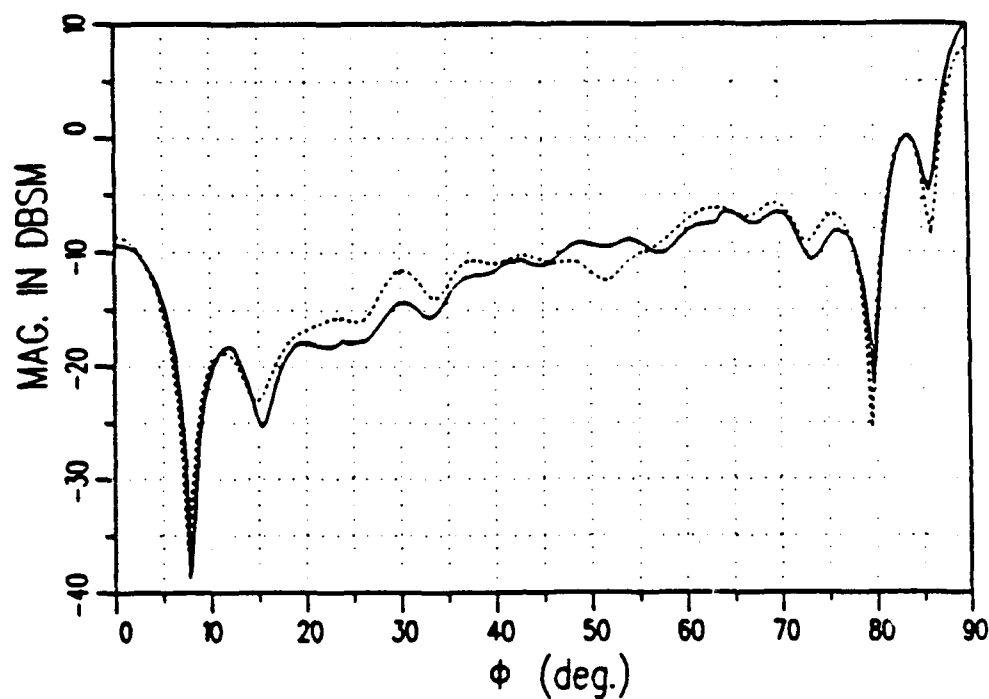
Figure 3.2: Backscatter field from a top-hat for horizontally polarized field. The solid line is UTD solution and the dashed line is the BOR solution.
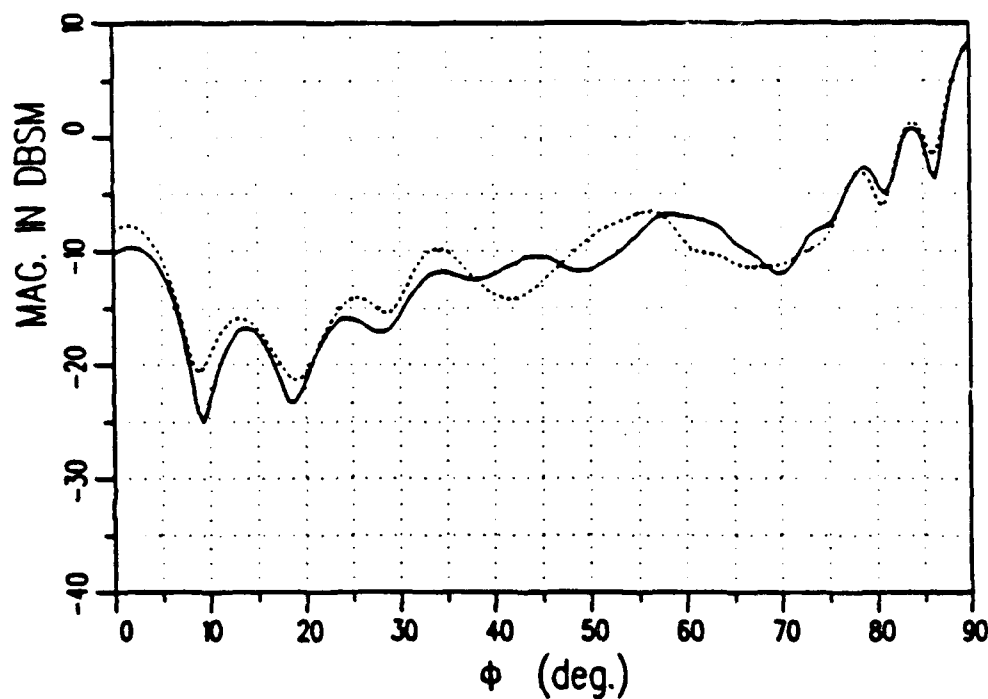
Figure 3.3: Backscatter field from a top-hat for vertically polarized field. The solid line is UTD solution and the dashed line is the BOR solution.

31
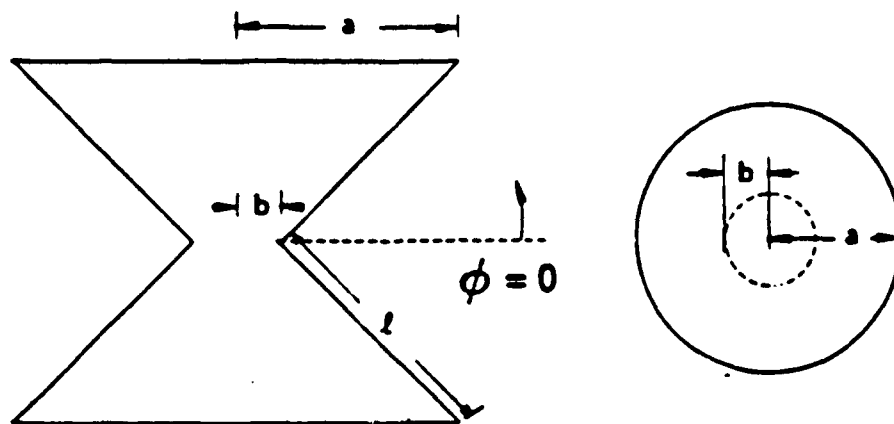
Figure 3.4: Bi-Cone geometry.

3.3.2 Modifications Required

Basically, caustic correction and spread factor modifications are required to the 2-D dihedral solution to get a result for the bi-cone. Two types of caustics need to be corrected. One is the rim caustic which has been used in the solution to the top hat in Section 3.2.4 with details given in [2] and [3]. The other is the curved surface caustic. Since diffraction is a local phenomena, it cannot be expected to account for a caustic of a global phenomena. However, the curved surface caustic is applicable if the two ends of the curved surface have the same radii of curvature (same spread factors for the two diffraction points). The diffraction coefficient from each of the edges "blows up" in the specular direction but combines to give the correct result. With the two radii of curvatures different, the diffraction coefficients from the two edges have different spread factors and the diffraction coefficient cannot combine to give the correct result.

3.3.3 Theoretical Background

In addition to the background information presented in Reference [1] and in Section 3.2, we need information on the curved surface caustic correction.

3.3.4 Curved Surface Caustic Correction

First Order

Details of the single diffraction curved surface caustic correction are presented in [2]. Basically, the term of the diffraction coefficient which "blows up" in the specular direction is corrected by the inclusion of a transition function. This result goes to the diffraction point solution outside the caustic region, making it a uniform solution. The specular terms from the two diffraction points with the correction are given as

$$D_{s,h}^{rn-} = R_{s,h} \frac{-e^{-j\pi/4}}{2n\sqrt{2\pi k}\sin\beta_o} \cot\left(\frac{\pi-(\phi+\phi')}{2n}\right) T_c\left(+jXa_e\right) \tag{3.24}$$

and

$$D_{s,h}^{rn+} = R_{s,h} \frac{-e^{-j\pi/4}}{2n\sqrt{2\pi k}\sin\beta_o} \cot\left(\frac{\pi-(\phi+\phi')}{2n}\right) T_c\left(-jXa_e\right). \tag{3.25}$$

The angles ϕ and ϕ' are measured from the curved surface, a_e is the radius of curvature of the diffracting edge, and

$$\begin{aligned} X &= K\cot\alpha_c \left[\tan^2\alpha_c\left(\cos^2 v + \epsilon_c^2\sin^2 v\right)+1\right]^{1/2} \\ &\quad\cdot\ \sin\beta_o 2\cos\left(\frac{\phi+\phi'}{2}\right)\cos\left(\frac{\phi-\phi'}{2}\right). \end{aligned} \tag{3.26}$$

The transition function is given as

$$T(z) = T_1(z) = \frac{2}{3}zM(1,2.5,-z) \tag{3.27}$$

or

$$T(z) = T_2(z) = -zU(1,2.5,-z) \tag{3.28}$$

where

$$U(1,2.5,-z) = -\frac{2}{3}M(1,2.5,-z) + \frac{\sqrt{\pi}}{2}(-z)^{-\frac{3}{2}}e^{-z}. \tag{3.29}$$

Physically, T_1 may be viewed as a result due to a finite cone frustum, and T_2 due to a semi-infinite cone frustum. Mathematically, both give the same result when both edges of the reflecting surface are considered. The small and the large argument of the transition function are the following:

for $|z| \ll 1$,

$$T_1(z) \approx e^{-z} \left(\frac{2z}{3} + \frac{2z^2}{5} + \frac{z^3}{7} \right) \tag{3.30}$$

$$T_2(z) \approx e^{-z} \left(\frac{\sqrt{\pi}}{2\sqrt{-z}} + \frac{2z}{3} + \frac{2z^2}{5} + \frac{z^3}{7} \right) \tag{3.31}$$

for $|z| \gg 1$,

$$T_1(z) \sim 1 + \frac{\sqrt{\pi}}{2} e^{\pm j\frac{3}{2}\pi} \frac{e^{-z}}{\sqrt{z}} - \frac{1}{2z} - \frac{1}{4z^2} \tag{3.32}$$

$$T_2(z) \sim 1 - \frac{1}{2z} - \frac{1}{4z^2} \tag{3.33}$$

3.3.5 Higher Order Terms

To maintain the physical optics result for the cone frustum in the specular region, the argument of the transition function for the curved surface must be the same for DR, RD, and DRD terms. However, $a_e = r_e$ where r_e is the radius of curvature at the reflection point. The formulation remains the same as for the first order curved caustic correction discussed above, in 3.3.4.

3.3.6 Dominant Result

As expected, the bi-cone has the same type of dominant mechanisms as the 2-D dihedral and the top-hat. Thus, the dominant result is obtained from diffracted, DR, RD, and DRD terms for the bi-cone.

3.3.7 D, RD, DR, and DRD terms

The expressions shown below are for backscatter from a bi-cone with parameters given in Figure 3.4. These expressions are valid for $-90° < \phi < 90°$ unless otherwise stated. Of course, by symmetry, the result for the other side may be obtained.

34

The diffraction coefficient from the top on the right side is given by

$$U_{right}^{D_1} = U_{s,h}^i \frac{-2e^{-j\pi/4}}{7\sqrt{2\pi k}} \left[2\cot\left(\frac{2\pi}{7}\right) + R_{s,h}\left\{ \cot\left(\frac{\frac{5\pi}{2}+2\phi}{\frac{7}{2}}\right) \right.\right.$$

$$\left.\left. + \cot\left(\frac{\frac{-\pi}{2}-2\phi}{\frac{7}{2}}\right) T_c\left(-jka\left(\frac{l}{a-b}\right)2\cos\left(\frac{3\pi}{4}+\phi\right)\right)\right\}\right]$$

$$\cdot\; T_e\left(2ka\cos\left(\phi\right)\right)\sqrt{\frac{a}{2\cos\left(\phi\right)}}\; e^{j2kl\cos\left(\frac{\pi}{4}-\phi\right)} \tag{3.34}$$

and for the left side

$$U_{left}^{D_1} = U_{s,h}^i \frac{4e^{-j\pi/4}\sin\left(\frac{4\pi}{7}\right)}{7\sqrt{2\pi k}}$$

$$\cdot\; \left[\frac{1}{\cos\left(\frac{4\pi}{7}\right)-1} + R_{s,h}\frac{1}{\cos\left(\frac{4\pi}{7}\right)-\cos\left(\frac{8\phi}{7}\right)}\right]$$

$$\cdot\; T_e\left(-2ka\cos\left(\phi\right)\right)\sqrt{\frac{a}{2\cos\left(\phi\right)}}\; e^{j\frac{\pi}{2}}$$

$$\cdot\; e^{j2kl\cos\left(\frac{\pi}{4}-\phi\right)}e^{-j\cdot lka\cos(\phi)}\;;\;\; 0<\phi \qquad . \tag{3.35}$$

The diffraction coefficient from the bottom on the right side is given by

$$U_{right}^{D_2} = U_{s,h}^i \frac{-2e^{-j\pi/4}}{7\sqrt{2\pi k}} \left[2\cot\left(\frac{2\pi}{7}\right) + R_{s,h}\left\{ \cot\left(\frac{\frac{5\pi}{2}-2\phi}{\frac{7}{2}}\right) \right.\right.$$

$$\left.\left. + \cot\left(\frac{\frac{-\pi}{2}+2\phi}{\frac{7}{2}}\right) T_c\left(-jka\left(\frac{l}{a-b}\right)2\cos\left(\frac{3\pi}{4}-\phi\right)\right)\right\}\right]$$

$$\cdot\; T_e\left(2ka\cos\left(\phi\right)\right)\sqrt{\frac{a}{2\cos\left(\phi\right)}}\; e^{j2kl\cos\left(\phi+\frac{\pi}{4}\right)} \tag{3.36}$$

and for the left side

$$U_{left}^{D_2} = U_{s,h}^i \frac{4e^{-j\pi/4}\sin\left(\frac{4\pi}{7}\right)}{7\sqrt{2\pi k}}$$

$$\cdot\; \left[\frac{1}{\cos\left(\frac{4\pi}{7}\right)-1} + R_{s,h}\frac{1}{\cos\left(\frac{4\pi}{7}\right)-\cos\left(\frac{8\phi}{7}\right)}\right]$$

$$\cdot\; T_e^l\left(-2ka\cos\left(\phi\right)\right)\sqrt{\frac{a}{2\cos\left(\phi\right)}}\; e^{j\frac{\pi}{2}}$$

$$\cdot\; e^{j2kl\cos\left(\phi+\frac{\pi}{4}\right)}e^{-j\cdot lka\cos(\phi)}\;;\;\; 0>\phi. \tag{3.37}$$

35

The diffraction reflection terms (D_1 refers to the diffraction from the top right edge and R refers to the reflection from the curved side of the bottom cone) are given as

$$U^{D_1 R} + U^{RD_1} = U^i_{s,h} \frac{-2e^{-j\pi/4}}{7\sqrt{2\pi k}} \left[2\cot\left(\frac{\frac{\pi}{2} - 2\phi}{\frac{7}{2}}\right) T_1 + 2\cot\left(\frac{\frac{3\pi}{2} + 2\phi}{\frac{7}{2}}\right) \right.$$
$$\left. + R_{s,h}\left\{ 2\cot\left(\frac{4\pi}{7}\right) - j7kl\cos\left(\phi + \frac{\pi}{4}\right)\right\}\right] \sqrt{\rho_1} \; ;$$
$$0 < \phi < \frac{\pi}{4} \tag{3.38}$$

where

$$T_1 = T_c\left(jkr_e\left(\frac{l}{a-b}\right)\cos\left(\frac{3\pi}{4} - \phi\right)\right) \tag{3.39}$$

and (D_2 refers to the diffraction from the bottom right edge and R refers to the reflection from the curved side of the top cone)

$$U^{D_2 R} + U^{RD_2} = U^i_{s,h} \frac{-2e^{-j\pi/4}}{7\sqrt{2\pi k}} \left[2\cot\left(\frac{\frac{\pi}{2} + 2\phi}{\frac{7}{2}}\right) T_2 + 2\cot\left(\frac{\frac{3\pi}{2} - 2\phi}{\frac{7}{2}}\right) \right.$$
$$\left. + R_{s,h}\left\{ 2\cot\left(\frac{4\pi}{7}\right) - j7kl\cos\left(\phi - \frac{\pi}{4}\right)\right\}\right] \sqrt{\rho_2} \; ;$$
$$-\frac{\pi}{4} < \phi < 0 \tag{3.40}$$

where

$$T_2 = T_c\left(jkr_e\left(\frac{l}{a-b}\right)\cos\left(\frac{3\pi}{4} + \phi\right)\right). \tag{3.41}$$

Also,

$$\rho_1 = \frac{aX}{2a\cos\left(\frac{\pi}{4} - \phi\right)\cos\left(\frac{\pi}{4}\right) + (\cos(\phi) - \sin(\phi))\left(2S\cos\left(\frac{\pi}{4}\right)\cos\left(\frac{\pi}{4} - \phi\right) + X\right)}, \tag{3.42}$$

$$S = \frac{l}{\cos\left(\frac{\pi}{4} - \phi\right)} \tag{3.43}$$

$$X = b + \frac{l}{\cos\left(\frac{\pi}{4} - \phi\right)}\cos\left(\frac{\pi}{4} + \phi\right)\cos\left(\frac{\pi}{4}\right) \tag{3.44}$$

and

$$\rho_2 = \frac{aX}{2a\cos\left(\frac{\pi}{4} + \phi\right)\cos\left(\frac{\pi}{4}\right) + (\cos(\phi) + \sin(\phi))\left(2S\cos\left(\frac{\pi}{4}\right)\cos\left(\frac{\pi}{4} + \phi\right) + X\right)}, \tag{3.45}$$

36

$$S = \frac{l}{\cos\left(\frac{\pi}{4} + \phi\right)} \tag{3.46}$$

$$X = b + \frac{l}{\cos\left(\frac{\pi}{4} + \phi\right)} \cos\left(\frac{\pi}{4} - \phi\right) \cos\left(\frac{\pi}{4}\right). \tag{3.47}$$

The curved surface caustic correction for the double diffraction ensures continuity of the fields. For the diffracted - reflected and reflected - diffracted fields, the caustic correction is required on the term associated with the incident shadow boundary. Using the separate wedges formulation, assuming angles for the double diffraction are measured from the curved surface, the terms $P_{s,h}\left(\Phi_{p=2}, \Phi_{q=2}\right)$ and $P_{s,h}\left(\Phi_{p=3}, \Phi_{q=3}\right)$ insure continuity of the incident shadow boundary of the DR and RD terms. Thus, the transition function required for the curved surface caustic correction is included only with these two terms. However, using the joined wedges formulation and assuming that angles are measured from the end cap, the term $P_{s,h}\left(\Phi_{p=1}, \Phi_{q=1}\right)$ insures continuity of the DR and RD terms.

For the DRD term, only the dominant term is retained for the joined wedges solution. The dominant DRD term at the top of the bi-cone (especially around $\phi = 45°$) is

$$
\begin{aligned}
U_{top}^{DRD} &= R_{s,h} U_{s,h}^{i} P_{s,h}\left(\Phi = \frac{\pi}{4} - \phi, n = \frac{7}{4}, d = 2l\right) \\
&\quad \cdot T_c\left(jkb\left(\frac{l}{a-b}\right)\cos\left(\frac{3\pi}{4} - \phi\right)\right) \\
&\quad \cdot \sqrt{\left(\frac{\rho_1}{\rho_1 + l}\right)\left(\frac{\rho^r}{\rho^r + l}\right)}\, \rho_2\, e^{j2kl\cos\left(\frac{\pi}{4} - \phi\right)}
\end{aligned} \tag{3.48}
$$

and from the bottom (especially around $\phi = -45°$)

$$
\begin{aligned}
U_{bottom}^{DRD} &= R_{s,h} U_{s,h}^{i} P_{s,h}\left(\Phi = \frac{\pi}{4} + \phi, n = \frac{7}{4}, d = 2l\right) \\
&\quad \cdot T_c\left(jkb\left(\frac{l}{a-b}\right)\cos\left(\frac{3\pi}{4} + \phi\right)\right) \\
&\quad \cdot \sqrt{\left(\frac{\rho_1}{\rho_1 + l}\right)\left(\frac{\rho^r}{\rho^r + l}\right)}\, \rho_2\, e^{j2kl\cos\left(\frac{\pi}{4} + \phi\right)}
\end{aligned} \tag{3.49}
$$

where

$$\rho_1 = \frac{a}{\cos(\phi) - \frac{\sqrt{2}}{2}} \tag{3.50}$$

$$\rho^r = \frac{(l + \rho_1)b}{b + 2\cos\left(\frac{\pi}{l}\right)(l + \rho_1)} \tag{3.51}$$

$$\rho_2 = \frac{a(l + \rho^r)}{a + (\cos(\phi) - \frac{\sqrt{2}}{2})(l + \rho^r)}. \tag{3.52}$$

3.3.8 Results

Figures 3.5 and 3.6 show the results obtained for the horizontal and vertical polarization by the UTD computer code and the Body of Revolution code at 10 GHz for $a = 2$ in., $b = 0.5$ in., and $l = 2\sqrt{1.5}$ in. bi-cone, where l is the slant length of one of the cones. It is expected that by including the diffracted-diffracted field the UTD results should become even better.

3.4 Conclusions

It has been shown that excellent results for electrically small sizes of a top-hat and bi-cone are obtained by making the necessary curvature modifications and caustic corrections to the 2-D dihedral solution. It is expected that with similar modifications, solutions to the bruderhedral and the cake-pan may be obtained. The solution to the donut also requires caustic corrections of first and second order.
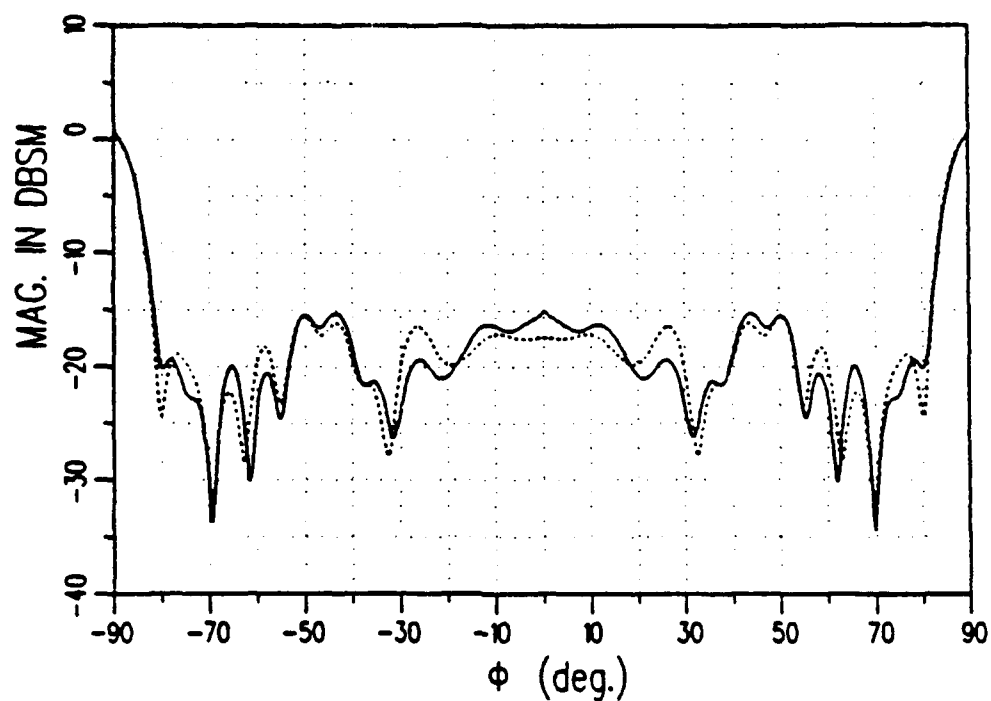
Figure 3.5: Backscatter field from a bi-cone for horizontally polarized field. The solid line is UTD solution and the dashed line is the BOR solution.
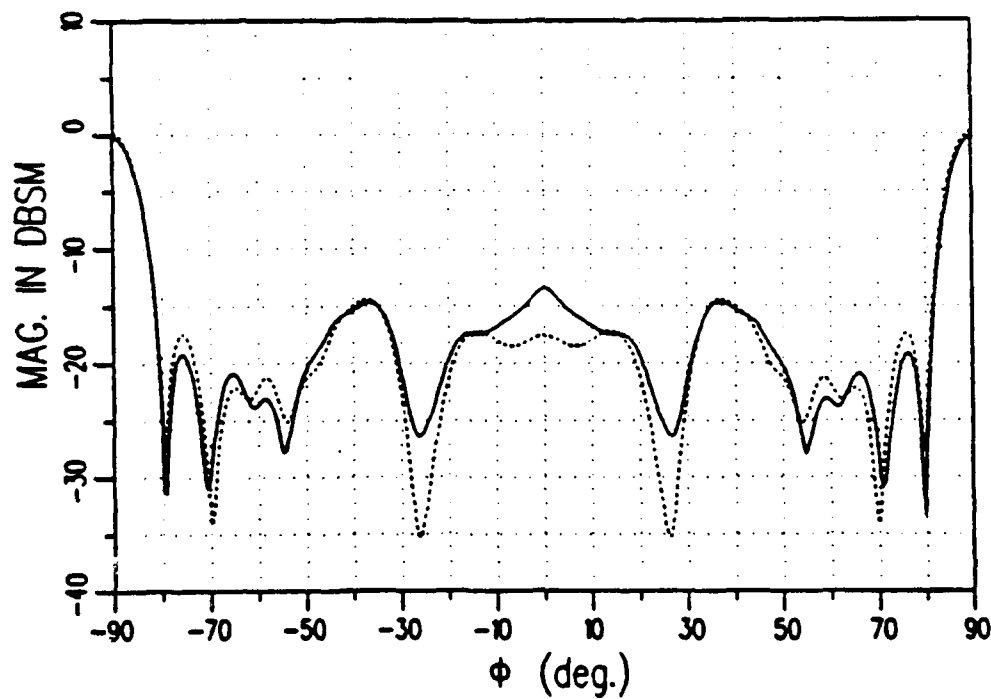

Figure 3.6: Backscatter field from a bi-cone for vertically polarized field. The solid line is UTD solution and the dashed line is the BOR solution.

Chapter 4

Far Zone Corner Diffraction

4.1 Introduction

Many local characteristic scattering centers of ground targets can be modeled by flat plate structures. In the far zone, the first order effects show up in images as emanating from the corners of the plates. The UTD treats this as the incident field multiplied by a diffraction coefficient. Comparisons of previous corner diffraction solutions with measurement based on ultrawideband images have shown discrepancies in some regions of space.

The report "Current Near the Vertex of a Perfectly Conducting Angular Sector," by T. J. Brinkley and R. J. Marhefka explores a new component missing in previous results. An approximate expression for the current on an angular sector is derived from the exact solution [5]. It is used to find a new far zone expression for the field diffraction by a vertex. This new vertex component is added to parts based on PO and fringe currents [6] and higher order local edge interaction parts [7]. The resulting diffraction coefficient is summarized in the next section.

The new expression for the corner diffracted field is verified by comparison with measurements where the contribution from a single vertex has been singled out using time domain gating techniques. The results are also applied to large flat plates and compared with excellent agreement to measured patterns. The advantage for

target identification is that the local frequency and angular behavior of vertex type structures can now be more accurately predicted.

4.2 Corner Diffracted Field Expression

The field diffracted by the corner of an angular sector is written as the sum of the contribution to the scattered field from the different currents on the angular sector. The far zone field scattered by an angular sector is

$$
\begin{aligned}
\vec{E}^c &= \vec{E}^{c,jpo} + \vec{E}^{c,jd1} + \vec{E}^{c,jd2} + \vec{E}^{c,jv} \\
&\quad + \vec{E}^{c,jd1t2} + \vec{E}^{c,jd2t1} + \vec{E}^{c,jd1d2} + \vec{E}^{c,jd2d1}.
\end{aligned}
\tag{4.1}
$$

The contribution from the physical optics current is

$$
\vec{E}^{c,jpo} = \sum_{m=1}^{2} \vec{E}_m^{c,jpo}
\tag{4.2}
$$

where

$$
\vec{E}_m^{c,jpo} = \hat{\beta}_m^i E_{\beta_m}^{c,jpom} + \hat{\psi}_m^i E_{\psi_m}^{c,jpom}
\tag{4.3}
$$

$$
\begin{bmatrix} E_{\beta_m}^{c,jpom} \\ E_{\psi_m}^{c,jpom} \end{bmatrix}
= \begin{bmatrix} D_s^{c,jpom} & D_2^{c,jpom} \\ 0 & D_h^{c,jpom} \end{bmatrix}
\begin{bmatrix} E_{\beta_m^i}^i (Q_c) \\ E_{\psi_m^i}^i (Q_c) \end{bmatrix} \frac{e^{-jkr}}{r}
\tag{4.4}
$$

$$
\begin{aligned}
D_{s,h,2}^{c,jpom} &= (-1)^{m-1} \frac{j}{8\pi k} \left(\frac{1}{\cos\beta_m - \cos\beta_m^i} \right) \left\{ \begin{array}{c} \frac{\sin\beta_m}{\sin\beta_m^i} \\ -\sin\psi_m \\ \sin\beta_m \end{array} \right\} \\
&\quad \cdot \sum_{n=1}^{2} \left[S^i C_{n1}^{s,h,2} \left(\gamma_m, \psi_m^i \right) \right]
\end{aligned}
\tag{4.5}
$$

$$
\begin{aligned}
C_{np}^s \left(\eta, \eta^i \right) &= (-1)^{n-1} \left[\cot \left(\frac{\pi - (\eta - (-1)^n \eta^i)}{4} \right) \right. \\
&\quad \left. + (-1)^p \cot \left(\frac{\pi + (\eta - (-1)^n \eta^i)}{4} \right) \right]
\end{aligned}
\tag{4.6}
$$

$$
\begin{aligned}
C_{np}^h \left(\eta, \eta^i \right) &= \frac{1}{\sin\eta} \left[\cot \left(\frac{\pi - (\eta - (-1)^n \eta^i)}{4} \right) \right. \\
&\quad \left. + (-1)^p \cot \left(\frac{\pi + (\eta - (-1)^n \eta^i)}{4} \right) \right]
\end{aligned}
\tag{4.7}
$$

$$
C_{n1}^2 \left(\eta, \eta^i \right) = \left(\cot\beta_m \cos\psi_m + \cot\beta_m^i \cos\eta^i \right) C_{n1}^h \left(\eta, \eta^i \right)
\tag{4.8}
$$

41

$$\cos \gamma_m = \frac{\sin \beta_m \cos \psi_m}{\sin \beta_m^i}$$

$$+ \frac{(\cos \beta_m - \cos \beta_m^i)^2}{\sin \beta_{in}^i (\sin \beta_m \cos \psi_m + \sin \beta_m^i \cos \psi_m^i)} \tag{4.9}$$

$$\cos^{-1} \mu = -j \ln \left(\mu + \sqrt{\mu^2 - 1} \right) \tag{4.10}$$

$$\sqrt{\mu^2 - 1} = \begin{cases} -\left| \sqrt{\mu^2 - 1} \right| & \mu < 1 \\ j \left| \sqrt{\mu^2 - 1} \right| & -1 \le \mu \le 1 \\ \left| \sqrt{\mu^2 - 1} \right| & \mu > 1 \end{cases} \tag{4.11}$$

$$S^i = \begin{cases} -1, \pi - \psi^i < 0 \\ 1, \pi - \psi^i > 0 \end{cases}. \tag{4.12}$$

The various angles are shown in Figure 4.1. The details of the derivation may be found in [8], [9], or [10].

The contribution from the edge diffracted current of edge m ($m = 1, 2$) terminated by edge m ($m = 1, 2$) is

$$\vec{E}^{c,jd_i} = \hat{\beta}_m^i E_{\beta_m}^{c,jdm} + \hat{\psi}_m^i E_{\psi_m}^{c,jdm} \tag{4.13}$$

$$\begin{bmatrix} E_{\beta_m}^{c,jdm} \\ E_{\psi_m}^{c,jdm} \end{bmatrix} = \begin{bmatrix} D_s^{c,jdm} & D_2^{c,jdm} \\ 0 & D_h^{c,jdm} \end{bmatrix} \begin{bmatrix} E_{\beta_m^i}^i (Q_c) \\ E_{\psi_m^i}^i (Q_c) \end{bmatrix} \frac{e^{-jkr}}{r} \tag{4.14}$$

$$D_{s,h,2}^{c,jdm} = (-1)^{m-1} \frac{j}{8\pi k} \left(\frac{1}{\cos \beta_m - \cos \beta_m^i} \right) \left\{ \begin{array}{c} \frac{\sin \beta_m}{\sin \beta_m^i} \\ -\sin \psi_m \\ \sin \beta_m \end{array} \right\}$$

$$\cdot \sum_{n=1}^{2} \left[C_{n2}^{s,h,2} \left(\alpha_m, \psi_m^i \right) - S^i C_{n1}^{s,h,2} \left(\alpha_m, \psi_m^i \right) \right] \tag{4.15}$$

$$C_{n2}^2 \left(\eta, \eta^i \right) = \left(\cot \beta_m \cos \psi_m - \cot \beta_m^i \cos \alpha_m \right) C_{n2}^h \left(\eta, \eta^i \right) \tag{4.16}$$

$$\cos \alpha_m = \frac{\sin \beta_m \cos \psi_m}{\sin \beta_m^i} + \frac{(\cos \beta_m - \cos \beta_m^i) \cos \beta_m^i}{\sin^2 \beta_m^i}. \tag{4.17}$$

The functions C_{np}^s, C_{np}^h, C_{n1}^2, S^i, and $\cos^{-1}$ have been defined previously in Equations (4.6), (4.7), (4.8), (4.12), and (4.10), and the angles are defined in Figure 4.1. The details of the derivation may be found in [9] or [10].

The contribution from the vertex diffracted current is

$$\vec{E}^{c,jv} = \frac{jkZ_0}{4\pi} \frac{e^{-jkr}}{r} \left[\int_0^{\alpha_v} \int_0^{r_1'} \hat{r} \times \hat{r} \times \vec{J}^{df} \left(\vec{r} \right) e^{jk\vec{r} \cdot \vec{r}'} r' dr' d\phi_c' \right.$$
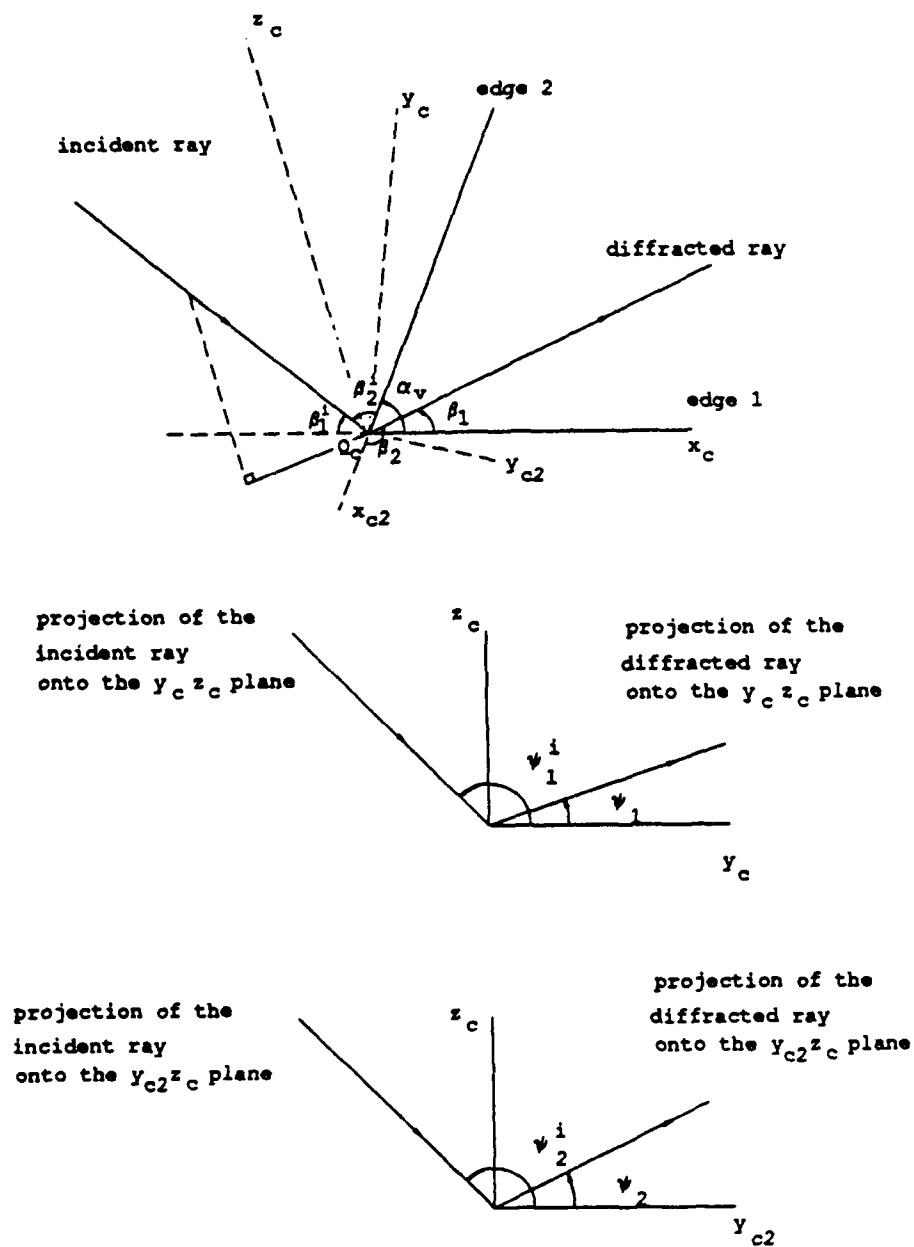
Figure 4.1: Edge fixed coordinates on an angular sector.

$$+ \int_0^{\alpha_v} \hat{r} \times \hat{r} \times \hat{r}' \frac{A_{r'}\left(\phi'_r\right)}{k^{\nu_{r'}(\phi'_c)}} \frac{\left(r'_1\right)^{1-\nu_{r'}(\phi'_r)} e^{-jk(1-\sin\theta_s\cos(\phi_c-\phi'_r))}}{jk\left(1-\sin\theta_s\cos\left(\phi s-\phi'_c\right)\right)} d\phi'_c$$

$$+ \int_0^{\alpha_v} \hat{r} \times \hat{r} \times \hat{\phi}'_c \frac{A_{\phi'_c}\left(\phi'_c\right)}{k^{\nu_{\phi'_c}(\phi'_c)}} \frac{\left(r'_1\right)^{1-\nu_{\phi'_c}(\phi'_c)} e^{-jk(1-\sin\theta_s\cos(\phi_s-\phi'_c))}}{jk\left(1-B\left(\phi'_c\right)\right)} d\phi'_c \qquad (4.18)$$

where

$$\vec{J}^{df}\left(\vec{r}\right) = \vec{J}^{AS}\left(\vec{r}\right) - \vec{J}^{PO}\left(\vec{r}\right) - \vec{J}^{d1}\left(\vec{r}\right) - \vec{J}^{d2}\left(\vec{r}\right) \qquad (4.19)$$

$$\nu_{r',\phi'_c} = \frac{\ln\left|\frac{J^{df}_{r',\phi'_c}\left(r'_1,\phi'_c\right)}{J^{df}_{r',\phi'_c}\left(r'_2,\phi'_c\right)}\right|}{\ln\left(\frac{r'_2}{r'_1}\right)} \qquad (4.20)$$

$$B'_{r',\phi'_c} = \frac{\arg\left(\frac{J^{df}_{r',\phi'_c}\left(r'_1,\phi'_c\right)}{J^{df}_{r',\phi'_c}\left(r'_2,\phi'_c\right)}\right)}{k\left(r'_2 - r'_1\right)} \qquad (4.21)$$

$$A_{r',\phi'_c}\left(\phi'_c\right) = \begin{cases} J^{df}_{r',\phi'_c}\left(\vec{r}'_1\right)\left(kr'_1\right)^{\nu_{r',\phi'_c}} e^{jkr'_1} \ ; \ B'_{\min} < B'_{r',\phi'_c} < B'_{\max} \\ 0; \ B'_{r',\phi'_c} < B'_{\min} \ or \ B'_{r',\phi'_c} > B'_{\max} \end{cases} \qquad (4.22)$$

$$B\left(\phi'_c\right) = \begin{cases} \sin\theta_s\cos\left(\phi_s - \phi'_c\right); \ \sin\theta_s\cos\left(\phi_s - \phi'_c\right) < 0.9 \\ 0.9; \ \sin\theta_s\cos\left(\phi_s - \phi'_c\right) > 0.9 \end{cases} \qquad (4.23)$$

The angles are defined in Figure 4.2. Expressions for the currents used in Equation (4.19) are given in [11]. The number of eigenvalues and the number of terms used in calculating the eigenfunctions are $N_{ev} = 7$ and $N_{ef} = 9$ to calculate $\vec{J}^{AS}(\vec{r})$ for the surface integral in Equation (4.18), $N_{ev} = 15$ and $N_{ef} = 15$ to calculate $\vec{J}^{AS}(\vec{r}'_1)$ for the line integral in Equation (4.18), and $N_{ev} = 25$ and $N_{ef} = 15$ to calculate $\vec{J}^{AS}(\vec{r}'_2)$ for the line integral in Equation (4.18). The values of the parameters used in all of the calculations are $r'_1 = 0.2\lambda$, $r'_2 = 0.3\lambda$, $B'_{\min} = 0.5$, and $B'_{\max} = 1.5$ which have been found to give fairly accurate results, while limiting the computational time required. The integrations in Equation (4.18) must be done numerically. A simple Riemann sum is used to do the integrations using 4 steps for the radial part of the surface integral, 20 steps for the angular part of the surface integral, and 20 steps for the line integration.
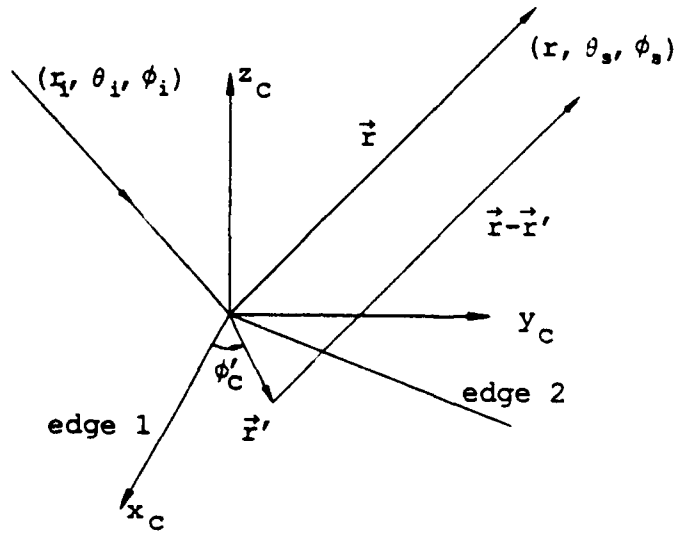
44

Figure 4.2: Radiation integral geometry for a far zone field point.

The contribution from the edge diffracted current of edge m ($m = 1, 2$) terminated by the other edge ($m = 2, 1$) is

$$\vec{E}^{c,jd1t2} = \vec{E}_1^{c,jdt} = \hat{\beta}_1^i E_{\beta_1}^{c,jd1t} + \hat{\psi}_1^i E_{\psi_1}^{c,jd1t} \tag{4.24}$$

$$\vec{E}^{c,jd2t1} = \vec{E}_2^{c,jdt} = \hat{\beta}_2^i E_{\beta_2}^{c,jd2t} + \hat{\psi}_2^i E_{\psi_2}^{c,jd2t} \tag{4.25}$$

where

$$
\begin{aligned}
E_{\beta_m}^{c,jdmt} = & -V(m) \frac{j \sin(\beta_m^i - \alpha_v)}{2\pi k \sin^3 \beta_m^i} \left\{ E_m^i(Q_c) \frac{\sin \beta_{in}}{\sin \beta_m^i} \varpi^{(2)} \left(\beta_m, \psi_m; \beta_m^i, \psi_m^i \right) \right. \\
& + Z_0 H_m^i(Q_c) \left[\cos \beta_m \cos \psi_m \varpi^{(0)} \left(\beta_m, \psi_m; \beta_m^i, \psi_m^i \right) \right. \\
& + \left. \left. \sin \beta_m \cot \beta_m^i \varpi^{(1)} \left(\beta_m, \psi_m; \beta_m^i, \psi_m^i \right) \right] \right\} \frac{e^{-jkr}}{r}.
\end{aligned}
\tag{4.26}
$$

$$E_{\psi_m}^{c,jdmt} = V(m) \frac{j Z_0 H_m^i(Q_c) \sin(\beta_m^i - \alpha_v) \sin \psi_m}{2\pi k \sin^3 \beta_m^i} \varpi^{(0)} \left(\beta_m, \psi_m; \beta_m^i, \psi_m^i \right) \frac{e^{-jkr}}{r} \tag{4.27}$$

where

$$V(m) = \begin{cases} U(\beta_1^i - \alpha_v) ; m = 1 \\ -U(\beta_2^i + \alpha_v - \pi) ; m = 2 \end{cases} \tag{4.28}$$

45

$$E'_m(Q_c) = \hat{x}_{cm} \cdot \vec{E}^i(Q_c) \tag{4.29}$$

$$H'_m(Q_c) = \hat{x}_{cm} \cdot \vec{H}^i(Q_c) \tag{4.30}$$

$$\varpi^{(0)}\left(\beta, \psi; \beta', \psi'\right) = \frac{U\left(\pi - \psi'\right)}{\sin \alpha_v \left(\cos \alpha + \cos \psi'\right)\left(\cos \delta + \cos \psi'\right)}$$
$$- \frac{\sin^2 \beta^i}{2 \sin\left(\beta^i - \alpha_v\right)\left(\cos \beta - \cos \beta'\right)}$$
$$\cdot \left[\frac{\csc \alpha \sin\left(\frac{\pi - \alpha}{2}\right)}{\cos \frac{\psi^i}{2} - \cos\left(\frac{\pi - \alpha}{2}\right)} - \frac{\csc \delta \sin\left(\frac{\pi - \delta}{2}\right)}{\cos \frac{\psi^i}{2} - \cos\left(\frac{\pi - \delta}{2}\right)}\right] \tag{4.31}$$

$$\varpi^{(1)}\left(\beta, \psi; \beta', \psi'\right) = \frac{U\left(\pi - \psi'\right)\cos \psi^i}{\sin \alpha_v \left(\cos \alpha + \cos \psi'\right)\left(\cos \delta + \cos \psi'\right)}$$
$$+ \frac{\sin^2 \beta^i}{2 \sin\left(\beta^i - \alpha_v\right)\left(\cos \beta - \cos \beta'\right)}$$
$$\cdot \left[\frac{\cot \alpha \sin\left(\frac{\pi - \alpha}{2}\right)}{\cos \frac{\psi^i}{2} - \cos\left(\frac{\pi - \alpha}{2}\right)} - \frac{\cot \delta \sin\left(\frac{\pi - \delta}{2}\right)}{\cos \frac{\psi^i}{2} - \cos\left(\frac{\pi - \delta}{2}\right)}\right] \tag{4.32}$$

$$\varpi^{(2)}\left(\beta, \psi; \beta', \psi'\right) = \frac{-U\left(\pi - \psi'\right)\sin \psi^i}{\sin \alpha_v \left(\cos \alpha + \cos \psi'\right)\left(\cos \delta + \cos \psi'\right)}$$
$$+ \frac{\sin^2 \beta^i \sin \frac{\psi^i}{2}}{2 \sin\left(\beta^i - \alpha_v\right)\left(\cos \beta - \cos \beta'\right)}$$
$$\cdot \left[\frac{\sin\left(\frac{\pi - \alpha}{2}\right)}{\cos \frac{\psi^i}{2} - \cos\left(\frac{\pi - \alpha}{2}\right)} - \frac{\sin\left(\frac{\pi - \delta}{2}\right)}{\cos \frac{\psi^i}{2} - \cos\left(\frac{\pi - \delta}{2}\right)}\right] \tag{4.33}$$

$$\cos \alpha = \frac{\sin \beta^i \sin \beta \cos \psi + \cos \beta^i \left(\cos \beta - \cos \beta'\right)}{\sin^2 \beta^i} \tag{4.34}$$

$$\cos \delta = \frac{\sin \alpha_v \sin \beta \cos \psi + \cos \alpha_v \left(\cos \beta - \cos \beta'\right)}{\sin \alpha_v \sin \beta^i}. \tag{4.35}$$

The details of the derivation may be found in [12, 7].

The contribution from the double diffracted current terminated by the last diffracting edge is

$$\vec{E}^{c,jd2d1} = \vec{E}_1^{c,jdd} \tag{4.36}$$

$$\vec{E}^{c,jd1d2} = \vec{E}_2^{c,jdd} \tag{4.37}$$

where

$$\vec{E}_m^{c,jdd} = E'_{\psi_m^i}(Q_c) V(m) \frac{e^{\frac{i\pi}{4}} \sin\left(\beta'_m - \alpha_v\right) \sin \beta_{m'}}{4 \left(2\pi k\right)^{3/2} \sin \alpha_v \sin^2 \beta'_m \left(1 - \nu\right)}$$

46

$$\cdot \ \left[\hat{\beta}_{m'} I_h\left(\beta_{m'},\psi_{m'};\beta'\right) - \hat{\psi}_{m'} M_h\left(\beta_{m'},\psi_{m'};\beta'\right)\right]$$

$$\cdot \ \sum_{p=1}^{2} \cot\left(\frac{\pi + (-1)^p \psi_m^i}{4}\right) F^c\left(a_p\left(\psi_m^i\right), 1-v\right)\frac{e^{-jkr}}{r} \qquad (4.38)$$

where

$$I_h\left(\beta,\psi;\beta'\right) \ = \ \frac{1}{\sin\beta'}\left\{\frac{\cot\beta\cos\psi + \cot\beta'}{\cos\alpha + 1}\right.$$

$$+ \ \left.\frac{\cos\alpha\cot\beta' - \cot\beta\cos\psi}{\sin\alpha}\cot\left(\frac{\pi-\alpha}{4}\right)\right\} \qquad (4.39)$$

$$M_h\left(\beta,\psi;\beta'\right) \ = \ \frac{\sin\psi}{\sin\beta\sin\beta'}\left\{\frac{1}{\cos\alpha + 1} - \frac{1}{\sin\alpha}\cot\left(\frac{\pi-\alpha}{4}\right)\right\} \qquad (4.40)$$

$$\cos\alpha \ = \ \frac{\sin\beta\cos\psi}{\sin\beta'} + \frac{\cos\beta'\left(\cos\beta - \cos\beta'\right)}{\sin^2\beta'} \qquad (4.41)$$

$$F^c\left(a, 1-v\right) \ = \ \frac{\sqrt{a}\sqrt{1-v}}{\sqrt{a} + \sqrt{1-v}} \qquad (4.42)$$

$$\sqrt{1-v} \ = \ \begin{cases} \left|\sqrt{1-v}\right| \ ; & 1-v > 0 \\ -j\left|\sqrt{1-v}\right|; & 1-v < 0 \end{cases} \qquad (4.43)$$

$$v \ = \ \frac{\sin\alpha_v\sin\beta_m\cos\psi_m + \cos\alpha_v\left(\cos\beta_m - \cos\beta'\right)}{\sin\alpha_v\sin\beta'} \qquad (4.44)$$

$$\beta' \ = \ (-1)^m\left(\pi - \beta_m^i\right) - \alpha_v \qquad (4.45)$$

$$a_p\left(\psi^i\right) \ = \ 1 + \cos\left[4N_p\pi - (-1)^p\psi_m^i\right] \qquad (4.46)$$

and N_p is the integer most nearly satisfying

$$4N_p\pi - (-1)^p\psi_m^i = \pi. \qquad (4.47)$$

The angles are defined in Figure 4.1, and the details of the derivation may be found in [7, 12].

4.3 Results

To illustrate the accuracy of the new corner diffracted field, it is compared with other methods. The results labeled the "New Corner" in Figure 4.6 are calculated using the contributions from the physical optics current, edge diffracted currents,
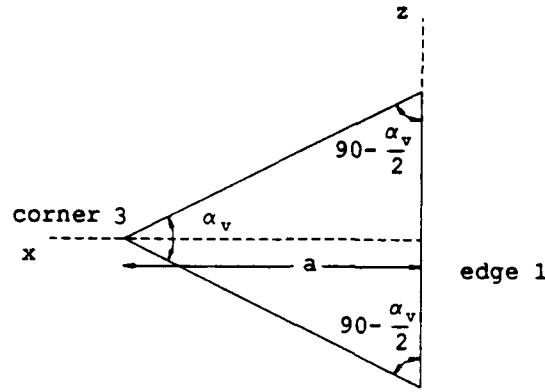
47

Figure 4.3: Vertical triangle.

the double diffracted current, and the vertex diffracted currents as given in the section above. The parameters used in calculating the contribution from the vertex diffracted current are $N_{ev} = 15$ and $N_{ef} = 15$ to find $\vec{J}^{AS}(\vec{r}_1')$, $N_{ev} = 25$ and $N_{ef} = 15$ to find $\vec{J}^{AS}(\vec{r}_2')$, $r_1' = 0.2\lambda$, $r_2' = 0.3\lambda$, 20 equally spaced rectangular approximations for the numerical evaluation of the linear integral, $N_{ev} = 7$ and $N_{ef} = 9$ to calculate $\vec{J}^{AS}$ for the surface integral, and 4 equally spaced rectangular approximations in the r' part of the surface integral, and 20 equally spaced rectangular approximations in the ϕ_c' part of the surface integral. The results are compared with measured results and the previous corner diffraction coefficient based on the contributions from the physical optics current [8, 9, 10], edge diffracted currents [9, 10], and double diffracted currents [7, 12].

Measurement data are processed using the following procedure to provide a reference solution for the field diffracted by the corner of an angular sector. Frequency swept measurements over a frequency range of 2 to 18 GHz are made on the triangle shown in Figure 4.3 for both the case $a = 32''$, $\alpha_v = 30°$ and the case $a = 32''$, $\alpha_v = 45°$ at 5° degree intervals in the $\theta = 90°$ pattern. The frequency swept data at each pattern point are transformed to the time domain to obtain the band limited impulse response. The approximate impulse response is convolved with a 35-dB
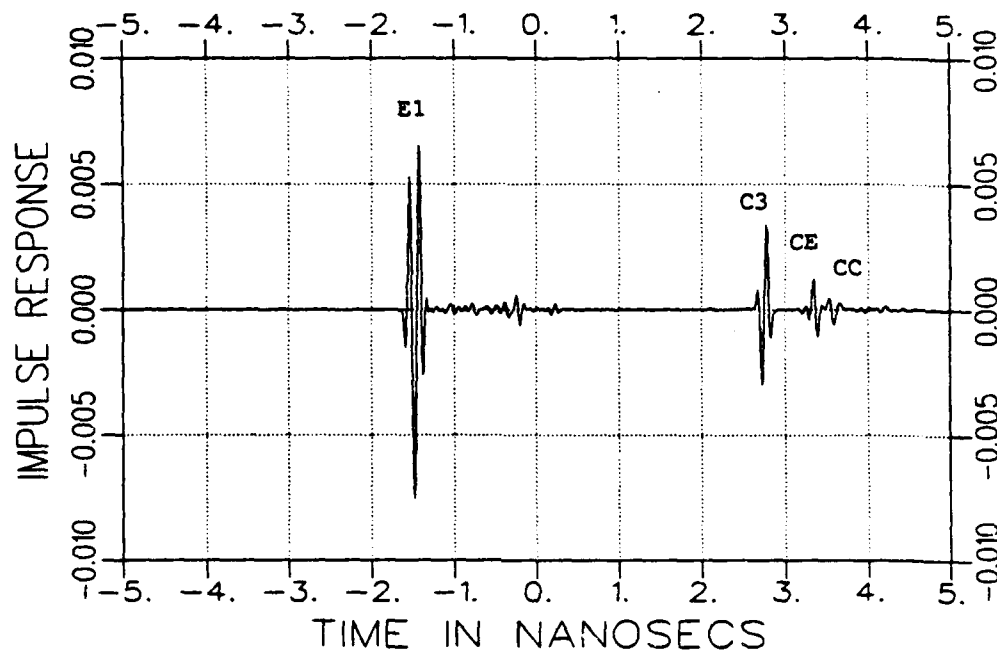
Figure 4.4: Impulse response ($\hat{\phi}$ polarized co-pol response) of the triangle in Figure 4.3 with a=32″ and $\alpha_v = 30°$ at $\theta = 90°$ and $\phi = 145°$.

Kaiser-Bessel smoothing waveform in order to eliminate Gibb's phenomenon ringing at the system cut-off frequency of 18 GHz. The time response, typical of those obtained for pattern points in the region $95° < \phi < 175°$, for the pattern angle $\phi \approx 145°$ is shown in Figure 4.4. The two first order mechanisms are labeled E1, which corresponds to the return from the front edge, and C3 which corresponds to the return from corner 3. The higher order mechanisms labeled CE and CC correspond to corner-edge interactions and corner-corner interactions. The path length to corner 3 is sufficiently different from the path lengths of the other mechanisms that the field diffracted by corner 3 may be gated out in the time domain over most of the pattern. The response from corner 3 is isolated in the time domain and then transformed back to the frequency domain to obtain the contribution from this corner over the entire frequency band. Further details of the time gating process may

49
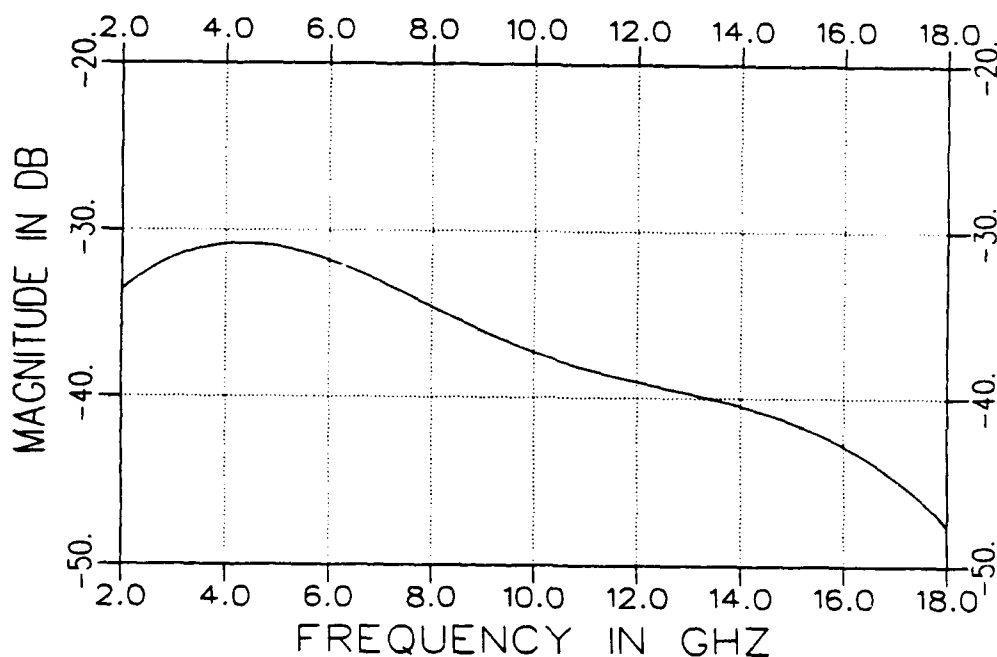
Figure 4.5: Frequency response ($\dot{\phi}$ polarized co-pol response) of corner 3 of the vertical triangle with a=32″ and $\alpha_v = 30°$ at $\theta = 90°$ and $\phi = 145°$.

be found in [13] and [14]. The contribution from corner 3 as a function of frequency is shown in Figure 4.5.

The measurements may then be used to determine the scattered field from an angular sector as a function of the pattern angle. From the frequency dependence of all of the components of the corner diffracted field in the section above and Figure 4.5 (which gives the cross section in dBsm), the corner diffracted field has a frequency response that varies as one over the frequency. The corner diffracted field is therefore constant for a given look angle when it is expressed in terms of dBSW. The roll-off at the upper and lower limits of the frequency response in Figure 4.5 is a result of the time gating process, so only the data in the center of the frequency range are used. The measurements are averaged (the contribution from the corner should be a constant when it is expressed in dBSW) over 50 evenly spaced samples in the region of 6 to 14 GHz to obtain the measured value of the corner diffracted field.

Repeating this process for all of the points in the pattern where the individual corner contribution may be gated out in the time domain results in the measured curves in Figure 4.6. The results show that the additional correction to the corner diffracted field improves the high frequency calculations considerably for this pattern.
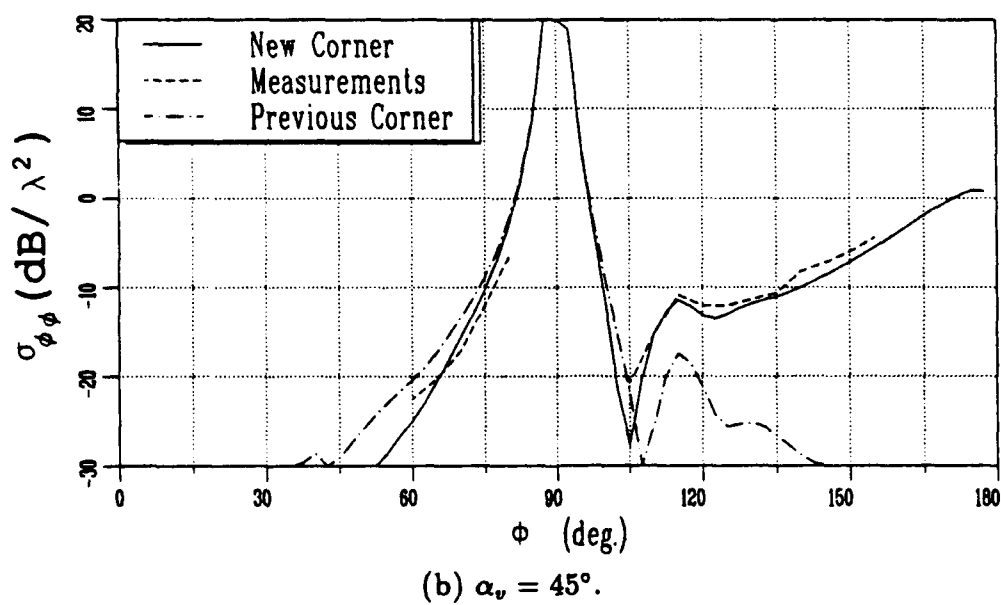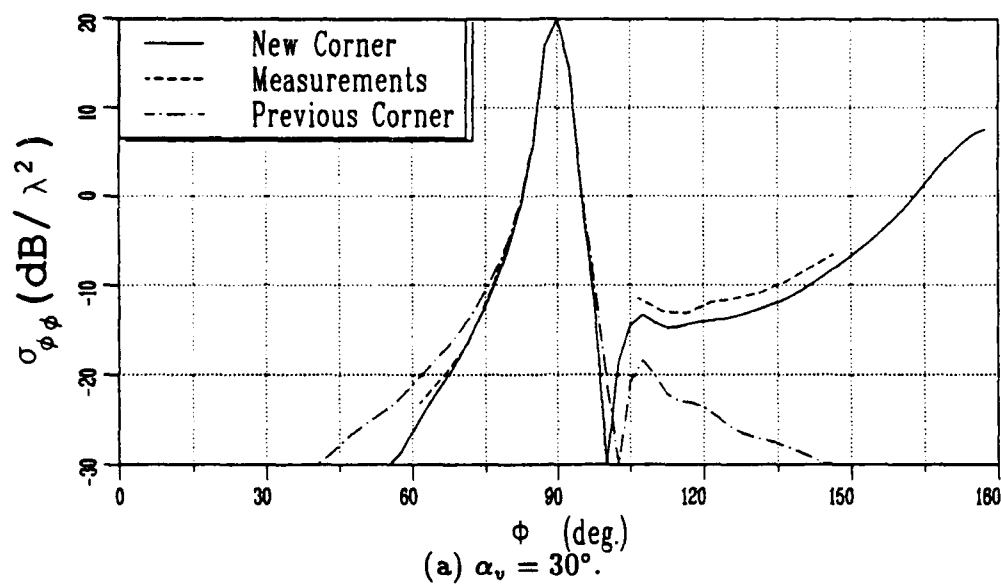
(a) $\alpha_v = 30°$.

(b) $\alpha_v = 45°$.

Figure 4.6: Calculated and measured contribution from corner 3 to the RCS ($\sigma_{\phi\phi}$) of the vertical triangle for a $\theta = 90°$ pattern.

52

Chapter 5

Higher Order Plate Terms

5.1 Goals

The scattering from polygonal plate structures is composed of its first order effects as discussed in the Chapter 4 as well as higher order terms that travel across the plates. These higher order terms show up as arcs in the SAR images. The goal of this effort is to understand the phenomenology of these higher order mechanisms in order to determine their frequency response and pattern behavior. This information is intended to provide insight into whether these mechanisms are robust enough to act as characteristics identifying tags of targets. In addition, preliminary determination of diffraction coefficients for double diffraction between noncoplanar skewed edges has been accomplished. These types of diffraction coefficients are needed for the evaluation of the complete patterns of trihedrals and dihedrals in three dimensions. The details are given in the report "High Frequency Electromagnetic Scattering by Conducting Polyhedral Structures," by L. P. Ivrissimtzis and R. J. Marhefka. Some relevant results to this contract's goals are outlined here.

5.2 Method

The phenomenon of higher order interactions between edges in flat plate structures for monostatic and bistatic cross section is investigated. Specifically, a ray approxi-

mation of the total field is developed starting with a postulate of the current on the scatterer. The surface current includes a primary nonuniform component generated by the edges of the structure in addition to the Physical Optics constituent. A secondary nonuniform current excited by doubly diffracted fields is also superimposed. The asymptotic reduction of the related surface or line integral results in individual mechanisms that are formulated in terms of corner-to-edge and edge-to-corner diffracted rays.

Edge wave interactions are examined as a field component in a high frequency formulation of the scattering by edged structures. The edge wave corner launching diffraction is derived via reciprocity from the approximation of the diffraction of dipole excited edge waves. Rediffraction of tip launched edge waves is formulated by replacing the tip that excites them with a fictitious dipole source radiating close to one of the edges of a trihedral. Pattern and time domain calculations reveal that the estimation of the edge wave interaction is adequate, as long as this type of return does not coincide in time with corner diffraction or doubly diffracted rays.

The canonical problem of near zone double diffraction by a pair of coplanar skewed edges is studied by employing an Extended Spectral Theory of Diffraction. A closed form double diffraction coefficient resulting from the asymptotic analysis is derived, and may be employed in pattern calculations of sources radiating in the presence of conducting flat plate objects. The solution is extended to the case of noncoplanar skewed edges via a heuristic modification of the pertinent transition function, so that continuity across the shadow boundaries of the edge diffracted rays is warranted.

5.3 Results

The various types of the higher order mechanisms that can exist on a plate are illustrated in Figure 5.1. It depicts a 24" square plate tilted at a 45° angle with respect to the horizontal plane. The measured images are presented in Chapter 6 in

Figures 6.5 and 6.6. The aspect angle is scanned from $-5°$ to $95°$ in step of $0.5°$ while for each angle the frequency is scanned from 2 to 18 GHz in steps of 20 MHz. The arcs appearing in the images of the plate correspond to higher order mechanisms.

The corner diffracted pulses are denoted by C1–C4 while possible edge wave mechanisms are indicated by E1–E4. The letter D is used to indicate doubly diffracted rays. In order to compare the calculated and measured results more clearly, down range cuts are compared in the complete report discussed in this chapter. Figures 5.2, 5.3, and 5.4 compare measurements to calculations for the $\theta = 30°$ vertical, horizontal, and cross-polarized components, respectively. Note that in the measured data, the two returns (S1, S2) are from the mount supports. Unknown mechanisms are marked with question marks.

In most cases good agreement is obtained. This is particularly true for the leading corners; trailing corners disagreed in some cases. This should be improved with the new vertex component discussed in Chapter 4. It was not available at the time of this report.

To observe the frequency behavior of isolated mechanisms, several of the separable ones have been time gated and transformed back into the frequency domain. Figures 5.5 and 5.6 show the $\theta = 30°$ cases for edge wave mechanisms marked E1 and E2, respectively. Excellent agreement between calculations and measurements are obtained for many of the cases. The largest discrepancy is associated with the double diffraction, D, terms across the plate. To illustrate the behavior of these terms, the time range between 2–3 nsec has been gated and transformed. These comparisons are shown in Figures 5.7 and 5.8. Apparently, the frequency characteristic of a double diffraction mechanism is comparable with that of an edge wave. As a matter of fact, in the high frequency domain, theory predicts both should decay with the inverse of $k^{3/2}$. The shape of these measured and computed curves in the frequency domain appear very similar.

The discrepancies in the curves are most likely attributable to the fact that these higher order mechanisms have been analyzed based on the simpler corner diffraction models. It will be interesting to see if the more advanced model described in Chapter 4 can be used to improve these predictions. Also note the terms that propagate diagonally across the plate have not been implemented at this time and, therefore, are not present in the calculated data.
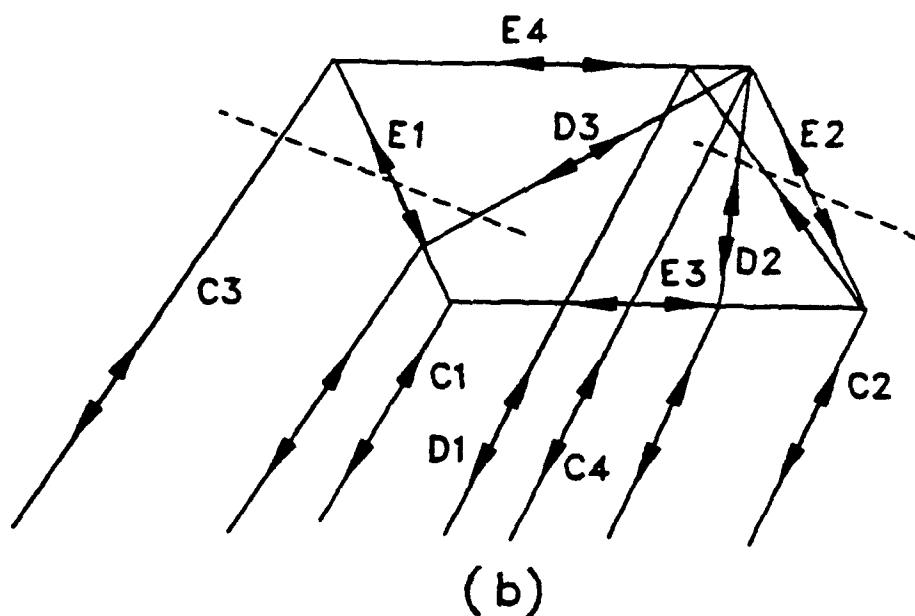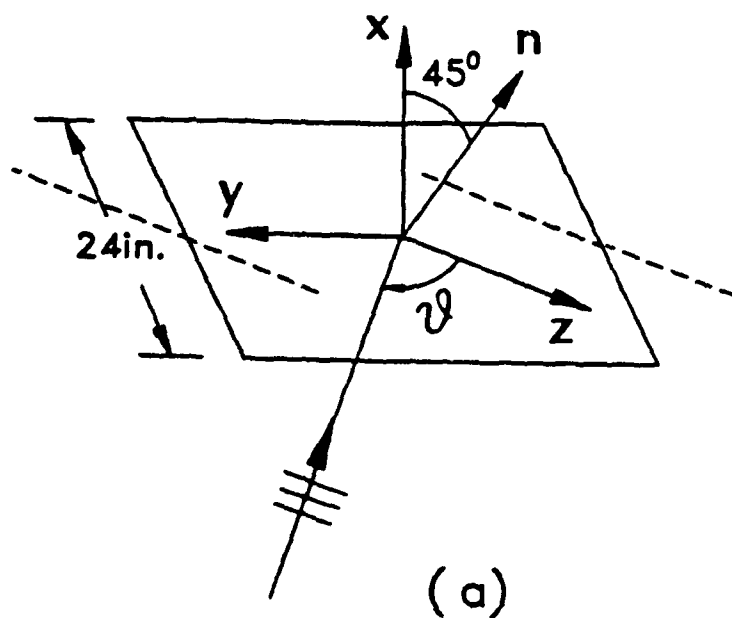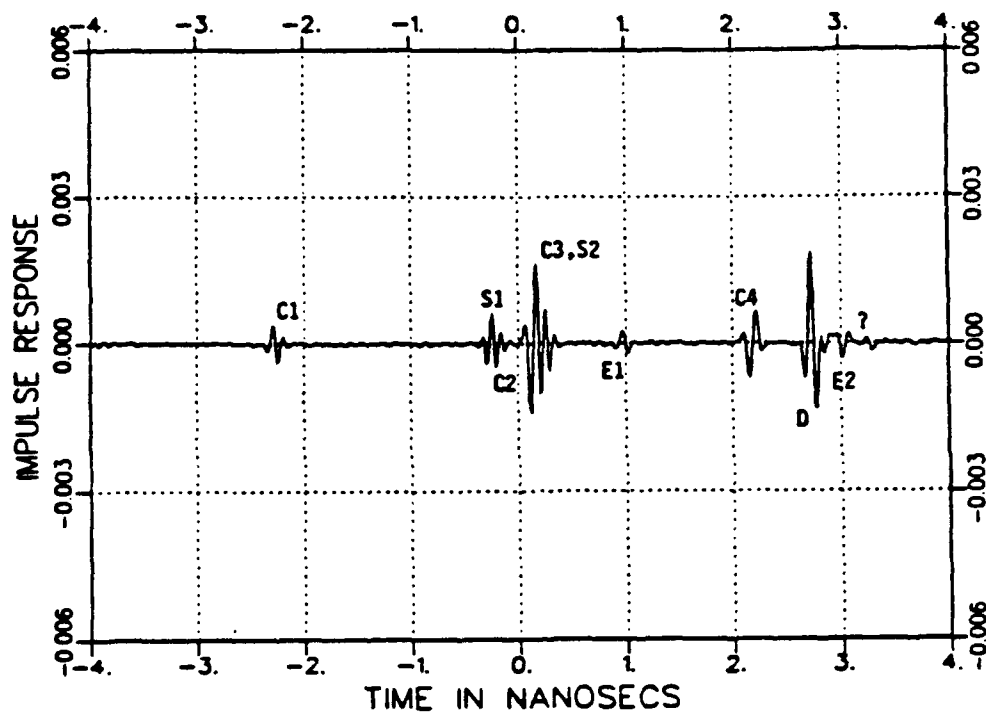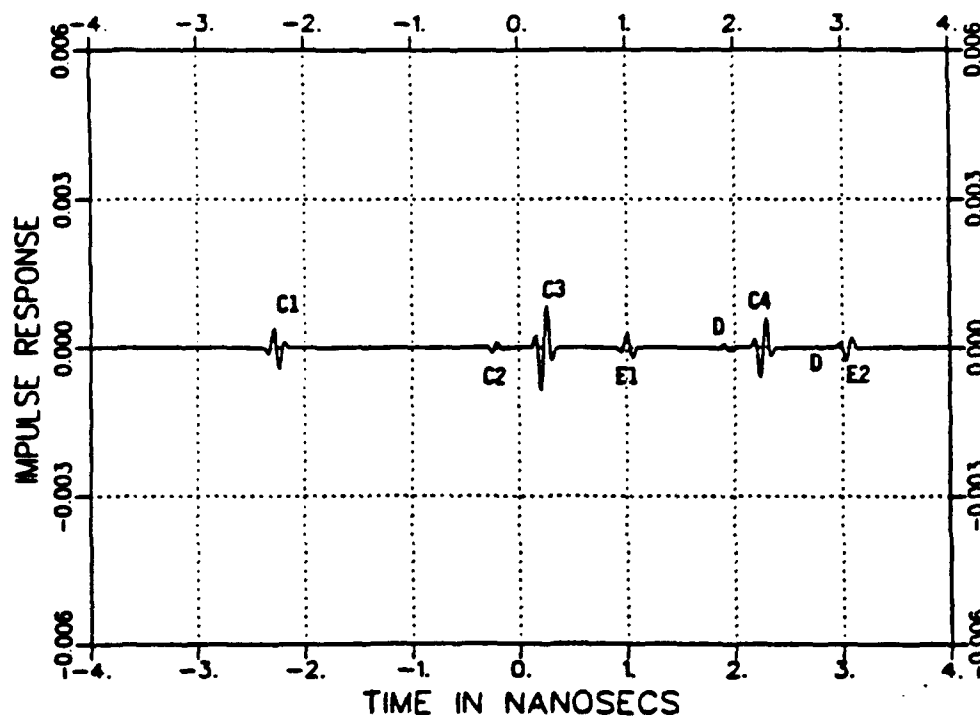
Figure 5.1: The 2 ft. square plate, tilted by 45° with respect to the horizontal plane, used in the time domain analysis: (a) Geometry, (b) Possible ray mechanisms.

Figure 5.2: Impulse response of a 24″ square plate at $\theta = 30°$ and $\phi = 90°$. Vertical polarization. (a) Measured, (b) Calculated.

58
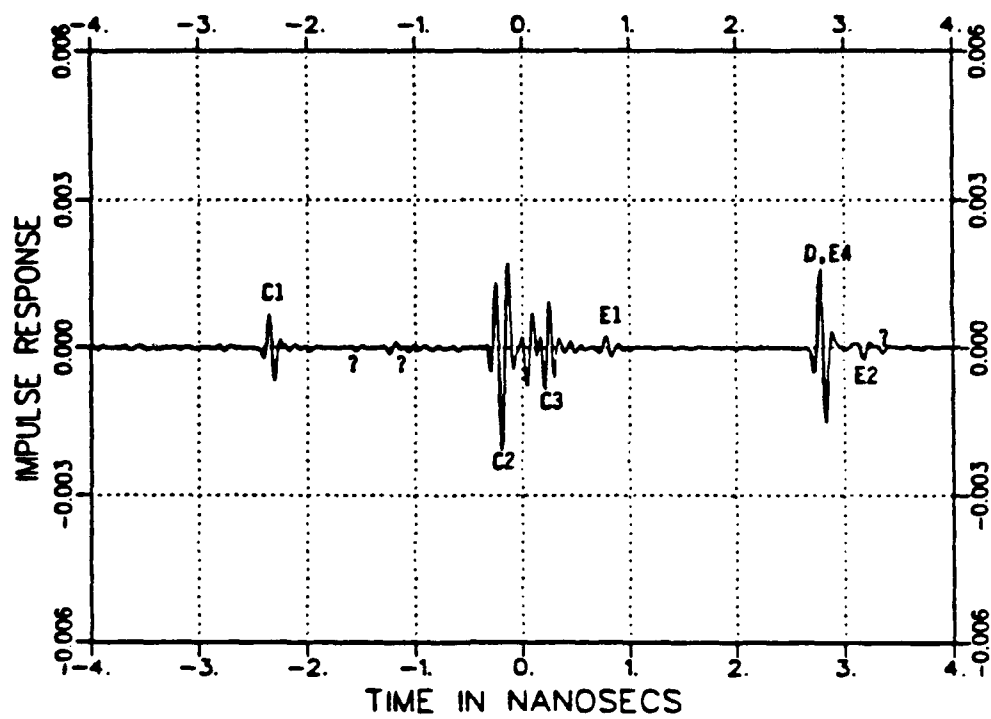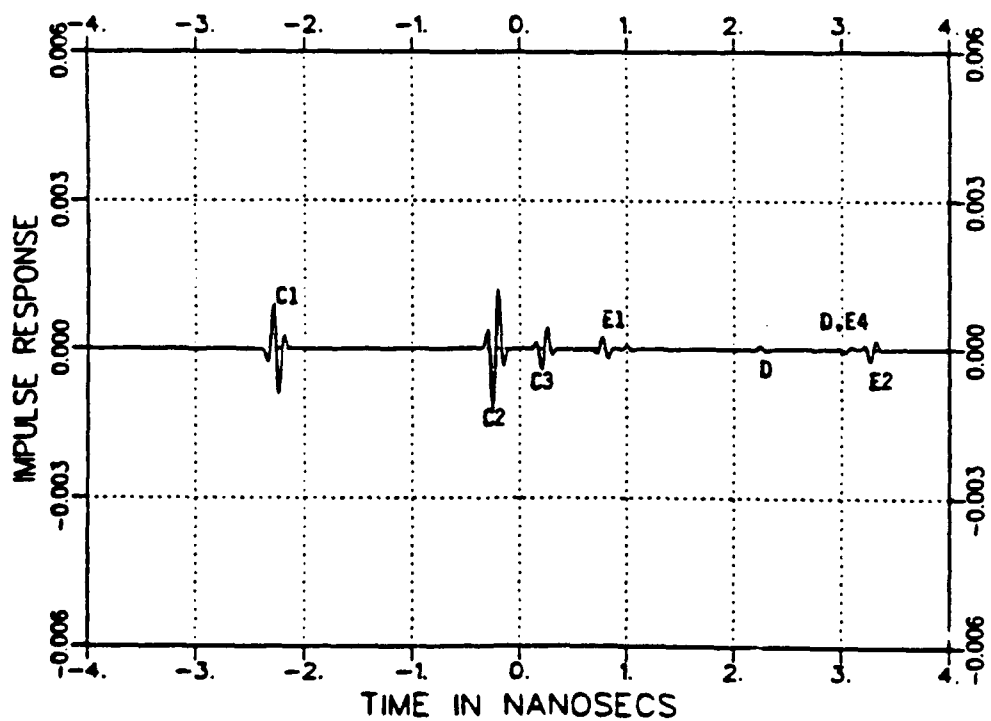
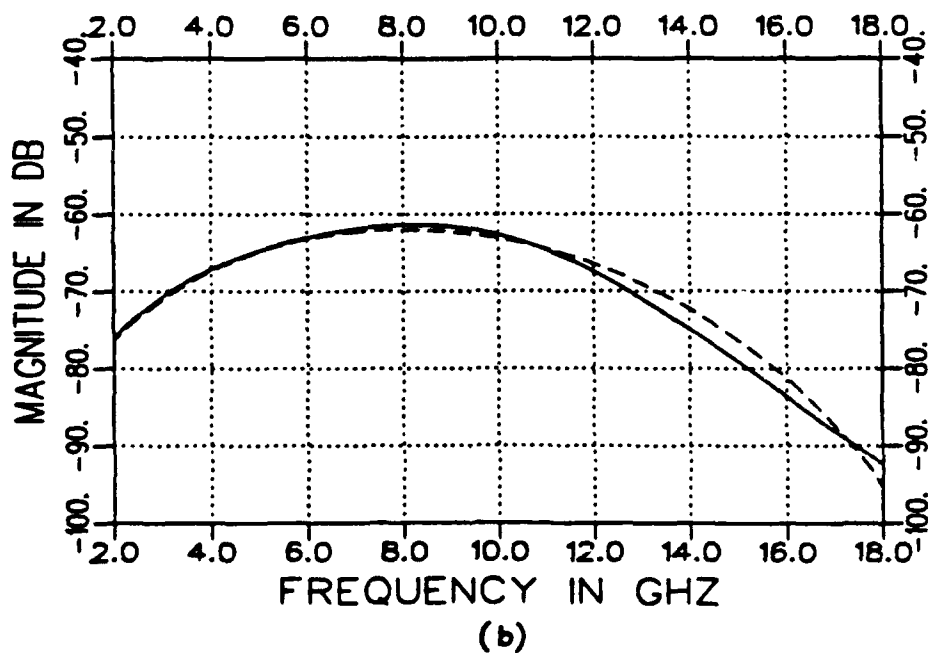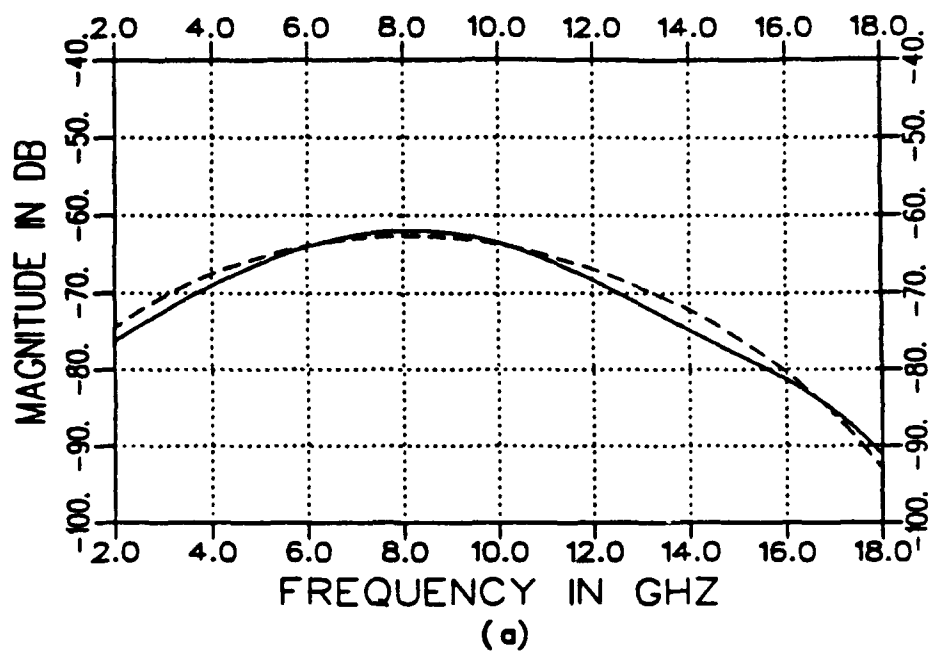Figure 5.3: Impulse response of a 24″ square plate at $\theta = 30°$ and $\phi = 90°$. Horizontal polarization. (a) Measured, (b) Calculated.
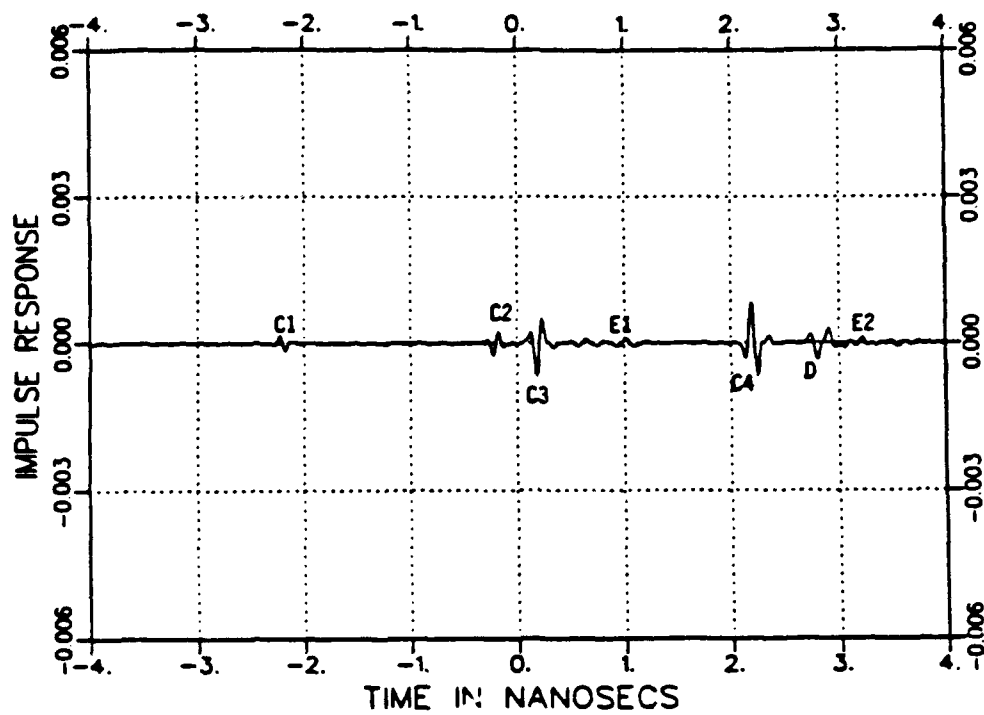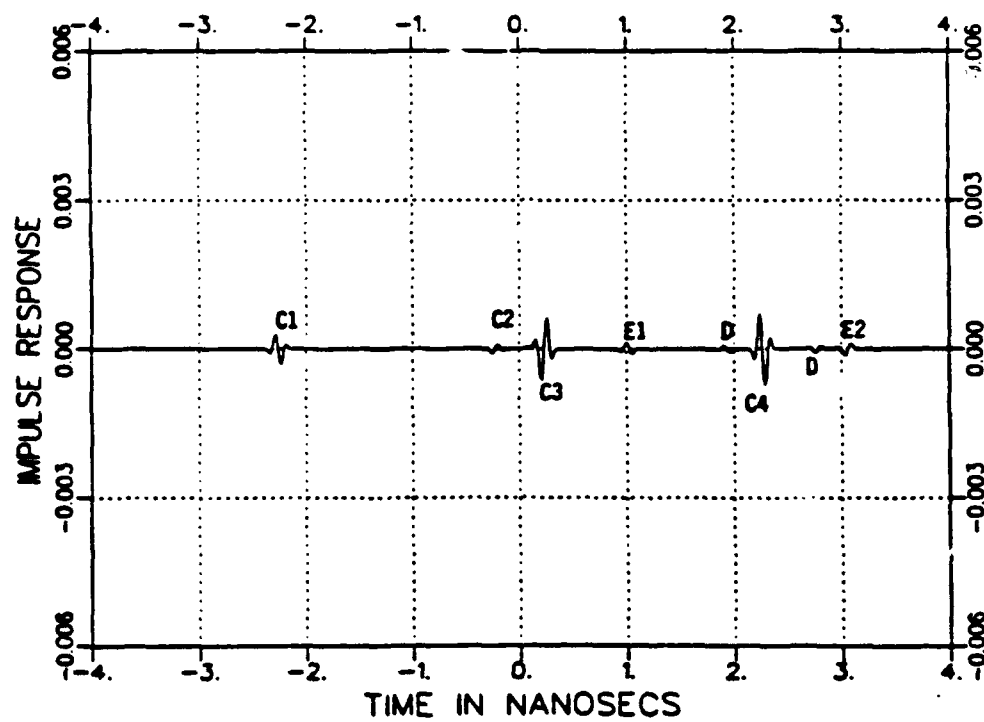
Figure 5.4: Impulse response of a 24″ square plate at $\theta = 30°$ and $\phi = 90°$. Cross polarization. (a) Measured, (b) Calculated.
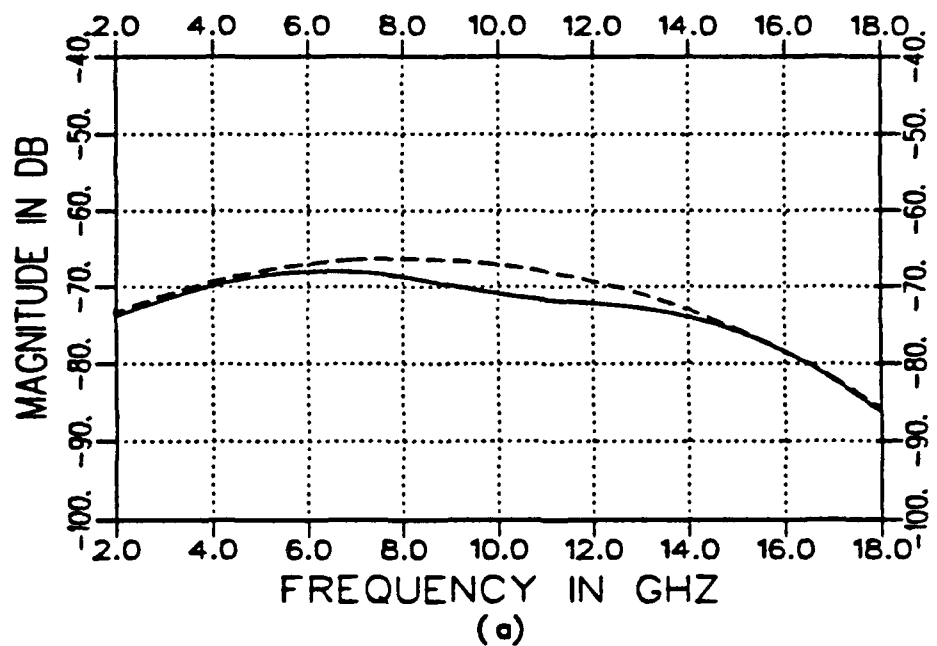
60

Figure 5.5: Frequency response of the edge wave diffraction mechanism E1 of a 24″ square plate at $\theta = 30°$ and $\phi = 90°$. (a) Vertical Polarization, (b) Horizontal Polarization. Solid line: measurements, dotted line: calculations.
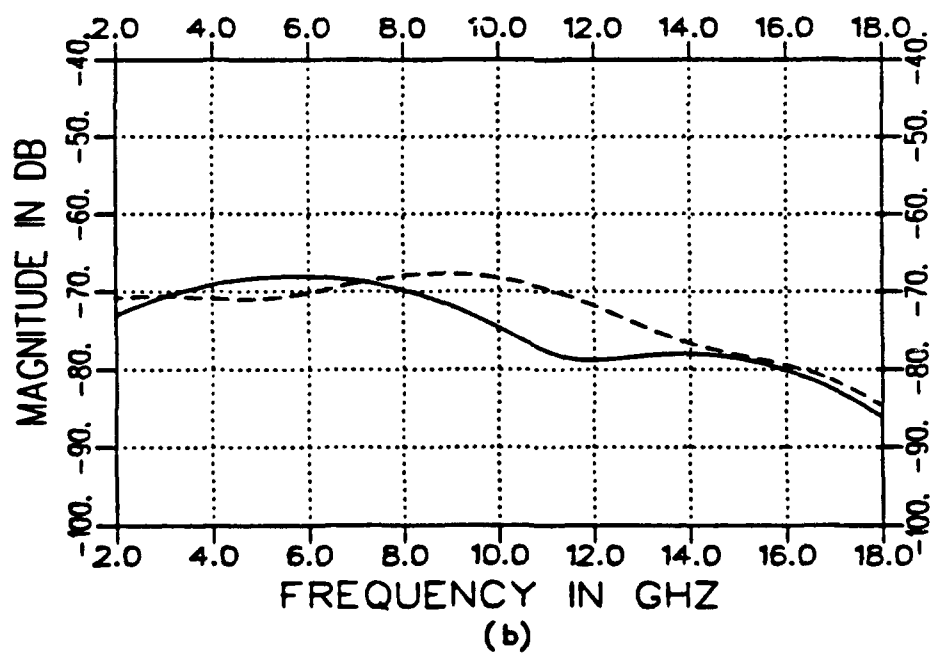
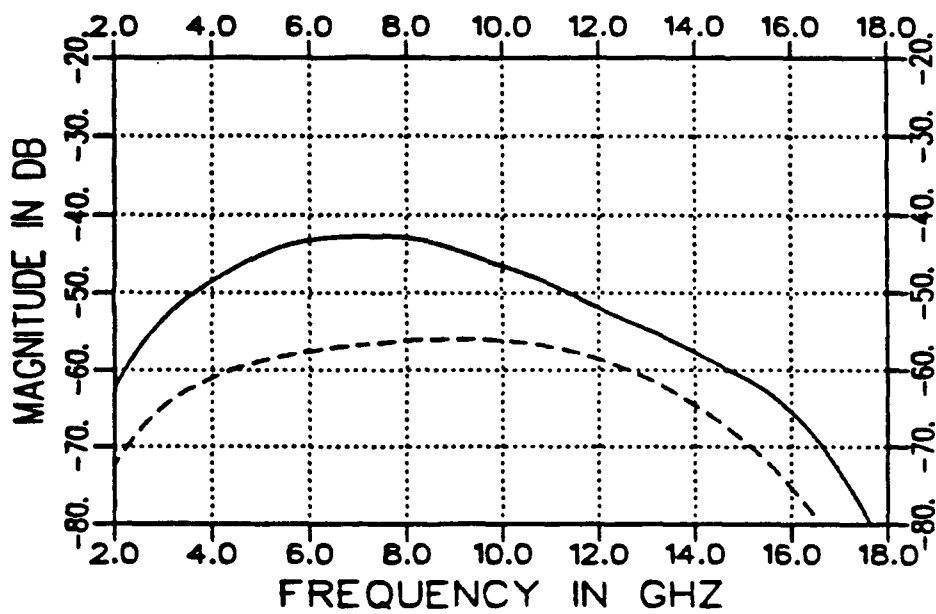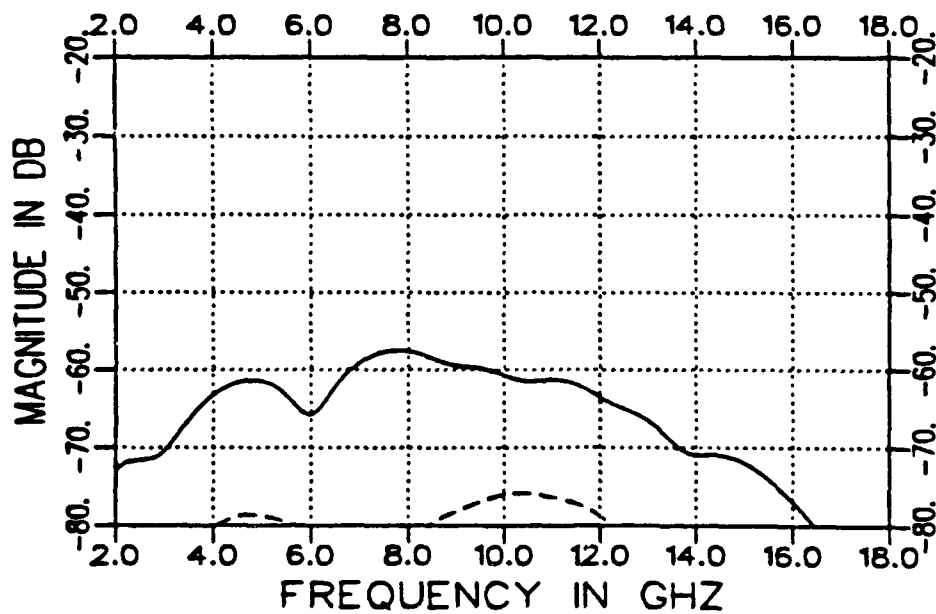Figure 5.6: Frequency response of the edge wave diffraction mechanism E2 of a 24″
square plate at $\theta = 30°$ and $\phi = 90°$. (a) Vertical Polarization, (b) Horizontal
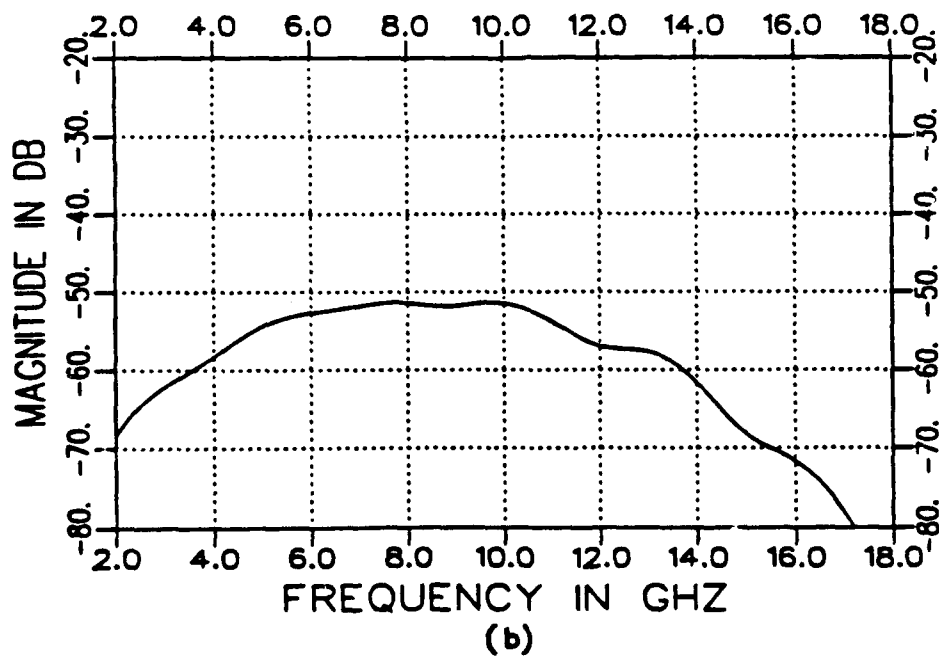Polarization. Solid line: measurements, dotted line: calculations.

Figure 5.7: Frequency response of the diffraction mechanisms within the time window (2ns,3ns) of a 24″ square plate at $\theta = 15°$ and $\phi = 90°$. (a) Vertical Polarization, (b) Horizontal Polarization. Solid line: measurements, dotted line: calculations.
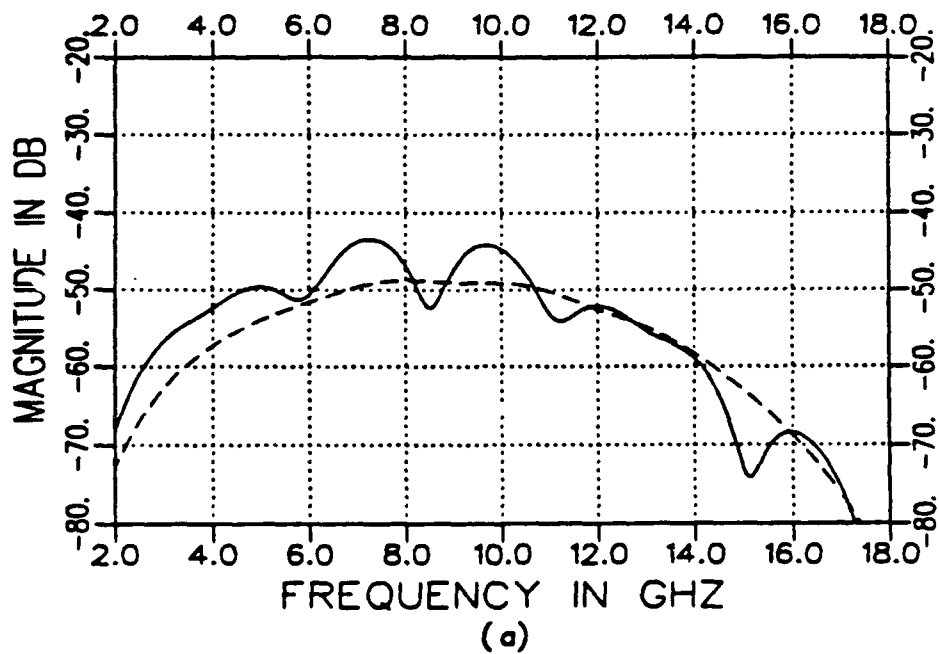
Figure 5.8: Frequency response of the diffraction mechanisms within the time window (2ns,3ns) of a 24″ square plate at $\theta = 75°$ and $\phi = 90°$. (a) Vertical Polarization, (b) Horizontal Polarization. Solid line: measurements, dotted line: calculations.

Chapter 6

Ultra-Wideband Imaging of Scattering Centers

6.1 Goals

One of the goals of the project was to perform fundamental diagnostic scattering mechanism research utilizing both analysis and measurements. This goal was fulfilled using the technique of ultra-wideband polarimetric imaging.

6.2 Method

The technique of ultra-wideband radar imaging is described in Report 721198-2, entitled "Ultra-Wideband Radar Imaging and the Diagnosis of Scattering Centers," by S. M. Scarborough. The process uses measured or calculated complex backscattering data for multiple polarizations over a 10:1 range of frequency and at least 90 degrees of look angle variation. A sketch of the "data space" is shown in Figure 6.1. It is known that imbedded in such data is information on not just the location, but also the frequency, angle, and polarimetric "signatures" of the scattering centers which comprise the total response of an object.

The imaging algorithm used in the report is the back-projection technique [15]. In this algorithm, the image construction is viewed as a weighted sum of one-dimensional projections, each of which is obtained from the complex spectral re-
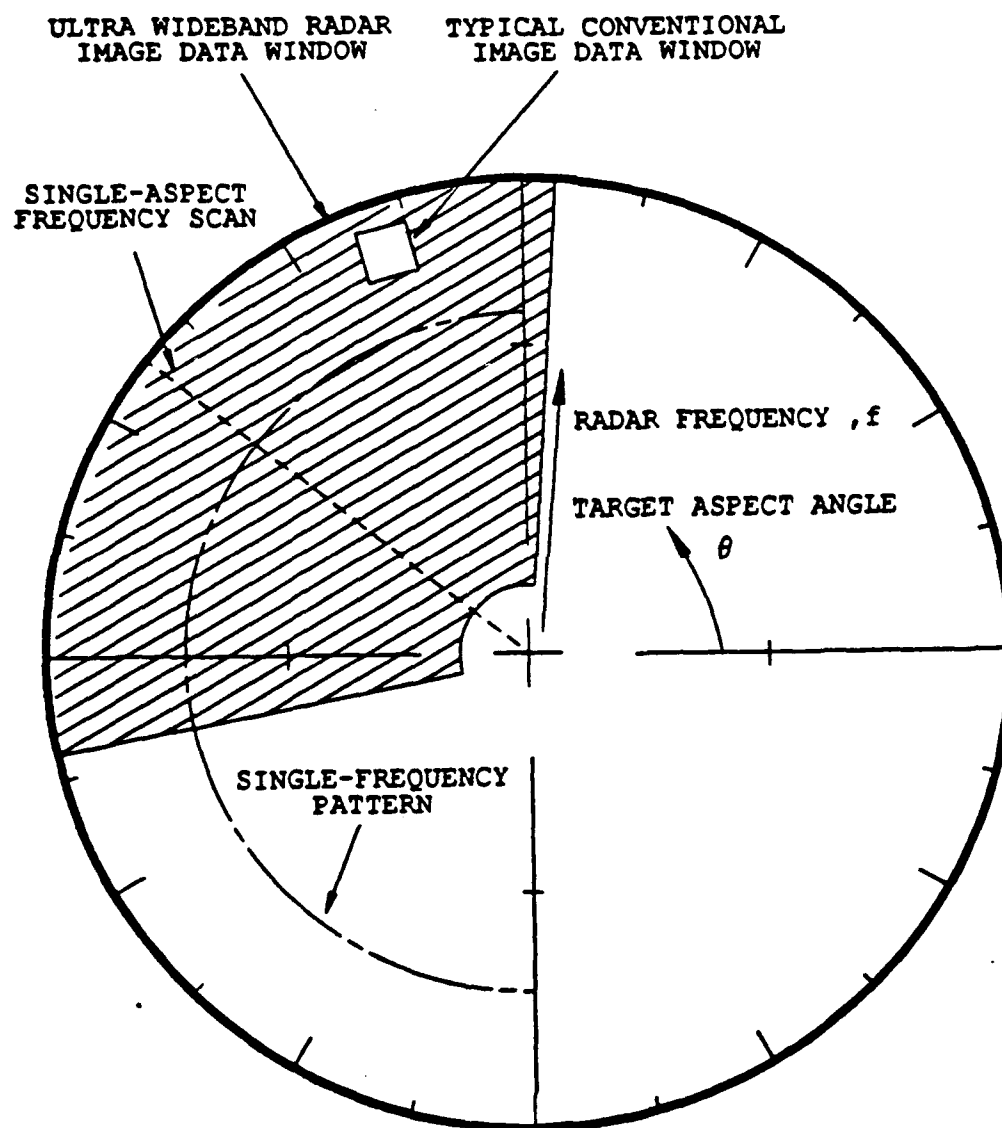
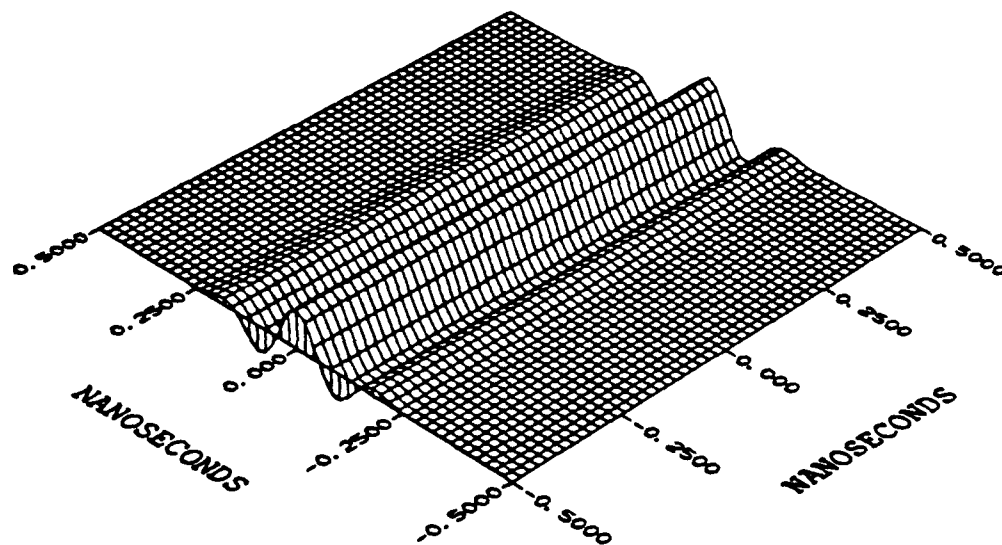Figure 6.1: Measurement data space for UWB images.

Figure 6.2: Image of bandlimited impulse — 1 back projection.

sponse at a particular target look angle lying in the radar measurement plane of angles. Figure 6.2 shows an image for a band-limited impulse at just one look angle. Figure 6.3 shows the image for just two look angles at 90 degrees to one another. Finally, Figure 6.4 shows an image using the band-limited impulse over a 180 degree range. This figure represents the typical point spread function of this imaging process. Using frequencies from 2–18 GHz and angle data ranges of at least 90 degrees or typically 180 degrees, 0.1 nsec or 1.5 cm resolution is obtained.

A sampling theorem exists which governs how often in angle and frequency the response must be recorded. If D is the maximum dimension of the target and c is the speed of light, then the sampling rate in frequency must be

$$\Delta f \leq \frac{c}{2(1+k)D}.$$

The factor k in this equation is a safety factor, whose value is usually 0.5 to 1. Angle sampling depends on both target maximum extent D and the highest frequency of
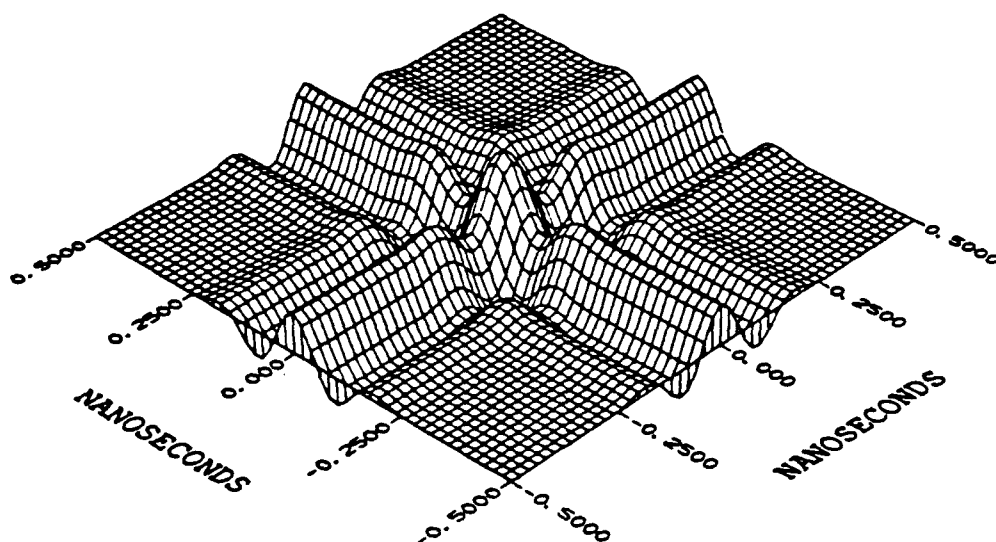
67

Figure 6.3: Image of bandlimited impulse — 2 back projections.

the interrogating radar signal, f_{II}. The frequency sampling rate must be

$$\Delta\theta \leq \frac{c}{2f_h D}.$$

Images have been produced using measured data of both simple and complex targets. For example, Figures 6.5 and 6.6 show the images for a tilted square conducting plate at horizontal and vertical polarization, respectively. The image simulates a top view of the object (perpendicular to the plane of the measurements). The outline of the plate is clear in both images. It looks rectangular instead of square because the plate is tilted 45 degrees with respect to horizontal. However, in addition to the rectangle outline are the returns from several other scattering mechanisms. The circle in the center is the return from the foam target support cylinder. The phantom edge in the vertical polarization image is a multiple scattering mechanism between the front and back edge of the plate. The arcs in the images are multiple scattering mechanisms created by "edge waves" and corner interactions on the target. The edge wave mechanisms, in particular, have been very difficult to identify before
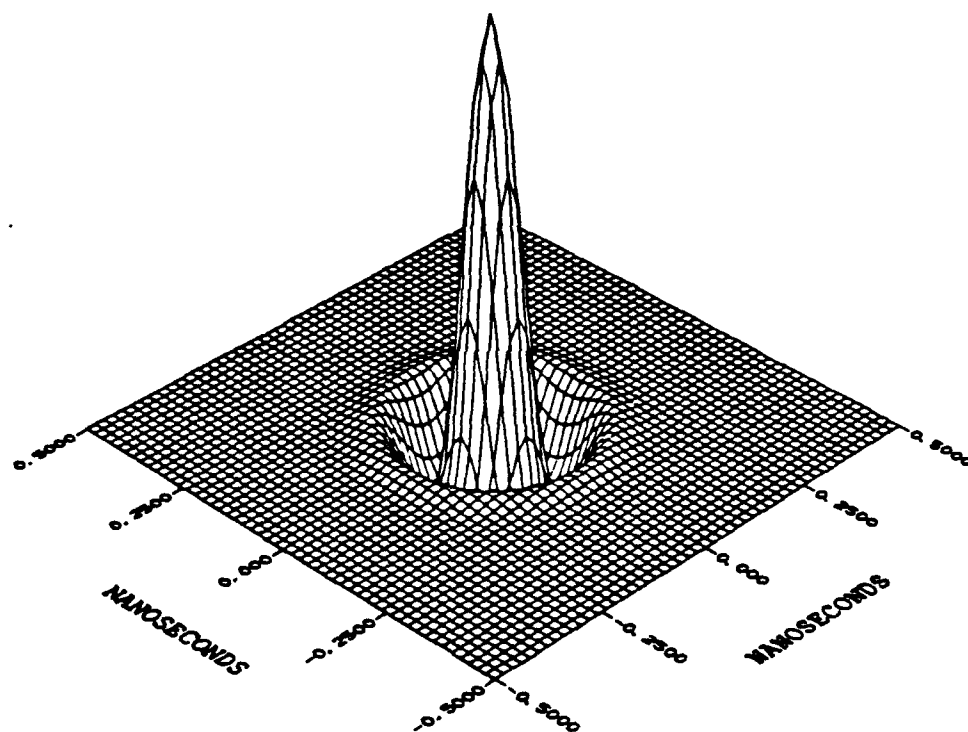
68

Figure 6.4: Image of bandlimited impulse over 180° angular bandwidth.

this process (and these data over such a wide coherent frequency and angle range) became available.

Figure 6.7 shows the image of a model MIG 21 using horizontal polarization. Figure 6.8 shows an image of an M35 army truck, with an outline of the truck superimposed. Both of these images show the outlines of the structure are preserved, but higher order scattering mechanisms are also visible. It could be that these higher order scattering terms are more distinctive for identification than the outlines.

The results also show there is information in these images in addition to the geometrical distribution of the scattering centers. If a gate is placed around a particular scattering center, then a transform process may be used to extract the frequency and angle response of just that particular mechanism. For example, Figure 6.9 shows the square plate image, with the outlines of three square gates which were used to separate individual mechanisms. A frequency-angle space image of the response of the diagonal corner interaction mechanism of window three is shown in Figure 6.10. A spectrum for the 30 degree look angle extracted from the image in Figure 6.10 is shown in Figure 6.11. The corner interaction demonstrates the $f^{-3/2}$ behavior as predicted by theory.

6.3 Conclusions

The conclusions from this report are:

- The high resolution of the images permits scattering mechanisms to be resolved distinctly.

- The high frequency bandwidth and angle range shows that the scattering mechanisms have distinctive behavior vs. frequency and angle, allowing them to be identified as well as located.
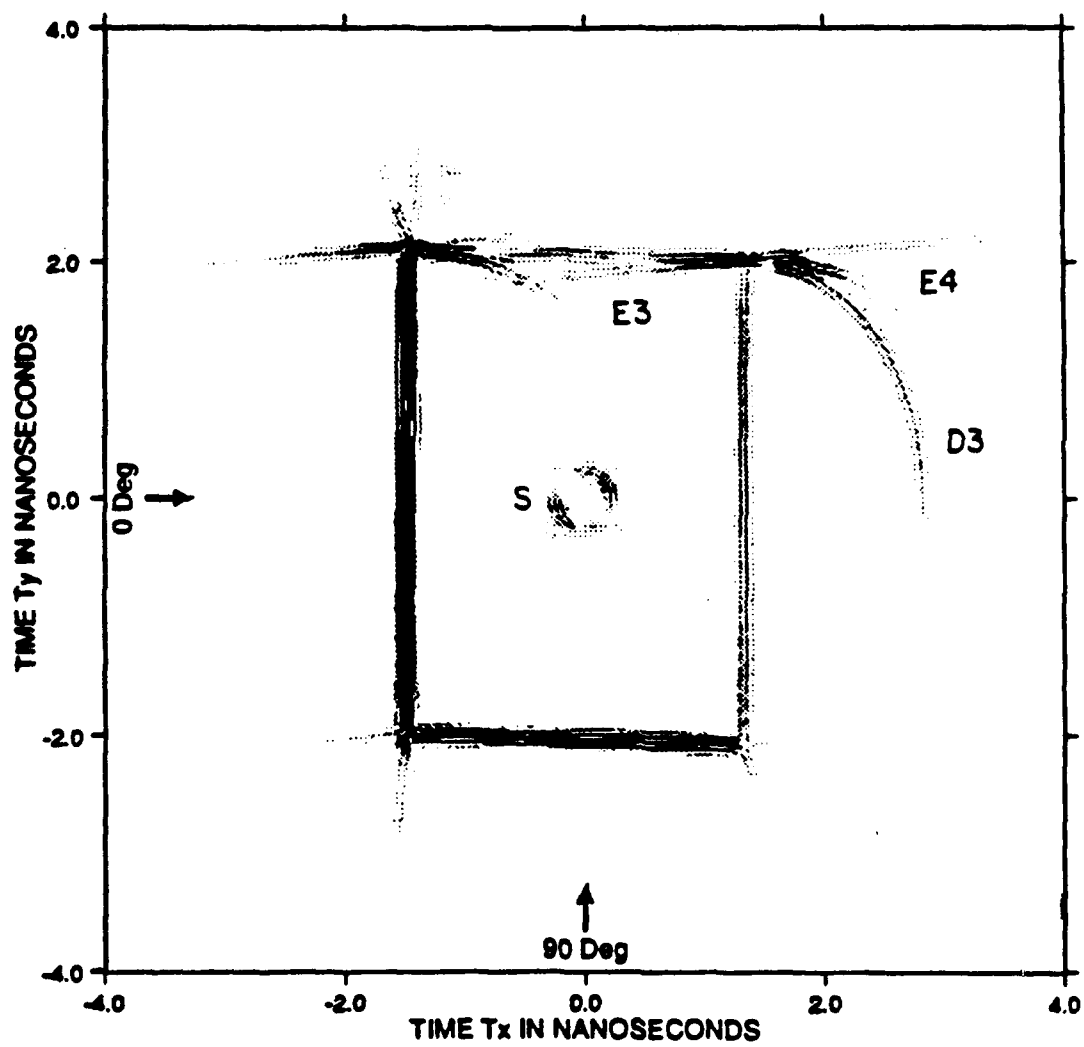
Figure 6.5: Image of tilted square plate, $-5°(0.5°)95°$ HP.

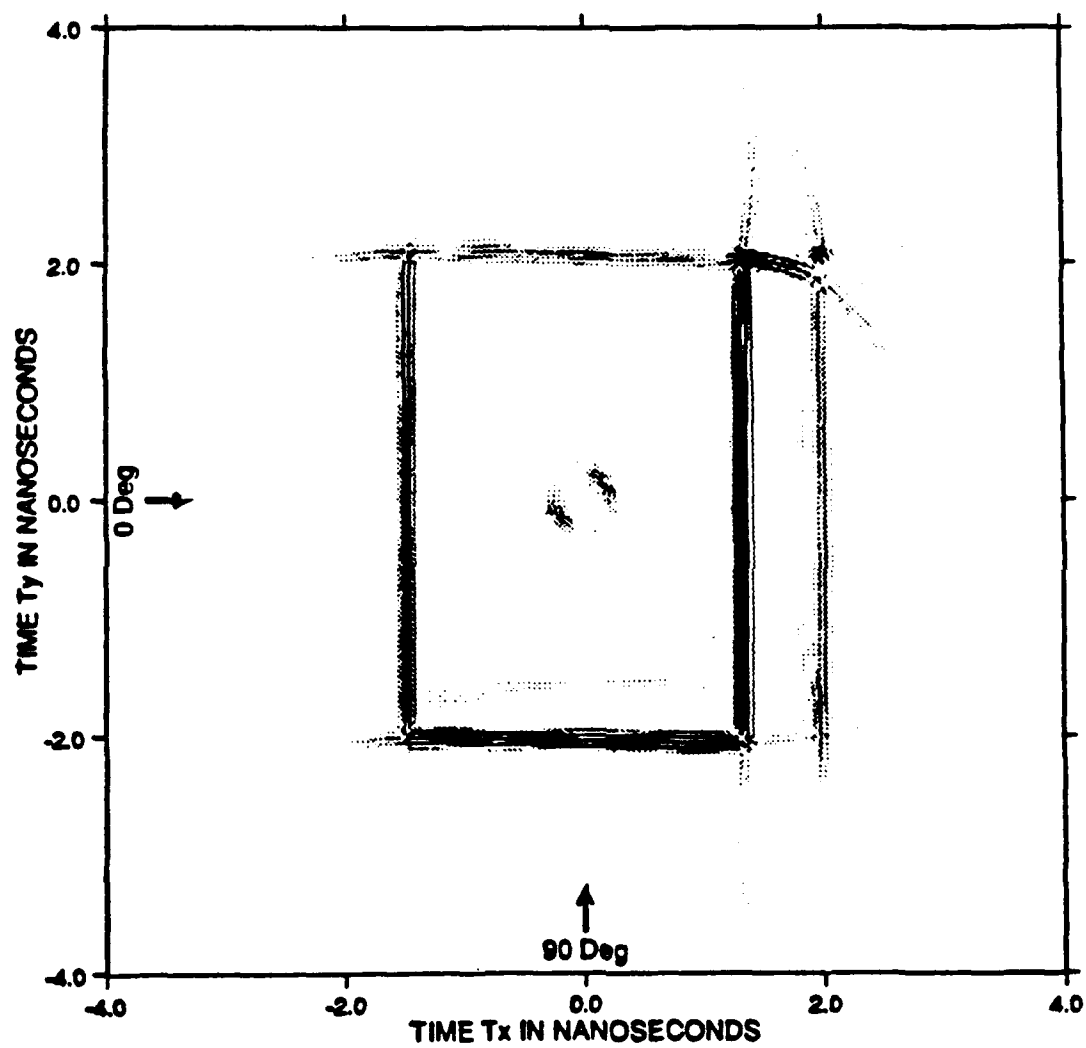Figure 6.6: Image of tilted square plate, −5°(0.5°)95° VP.
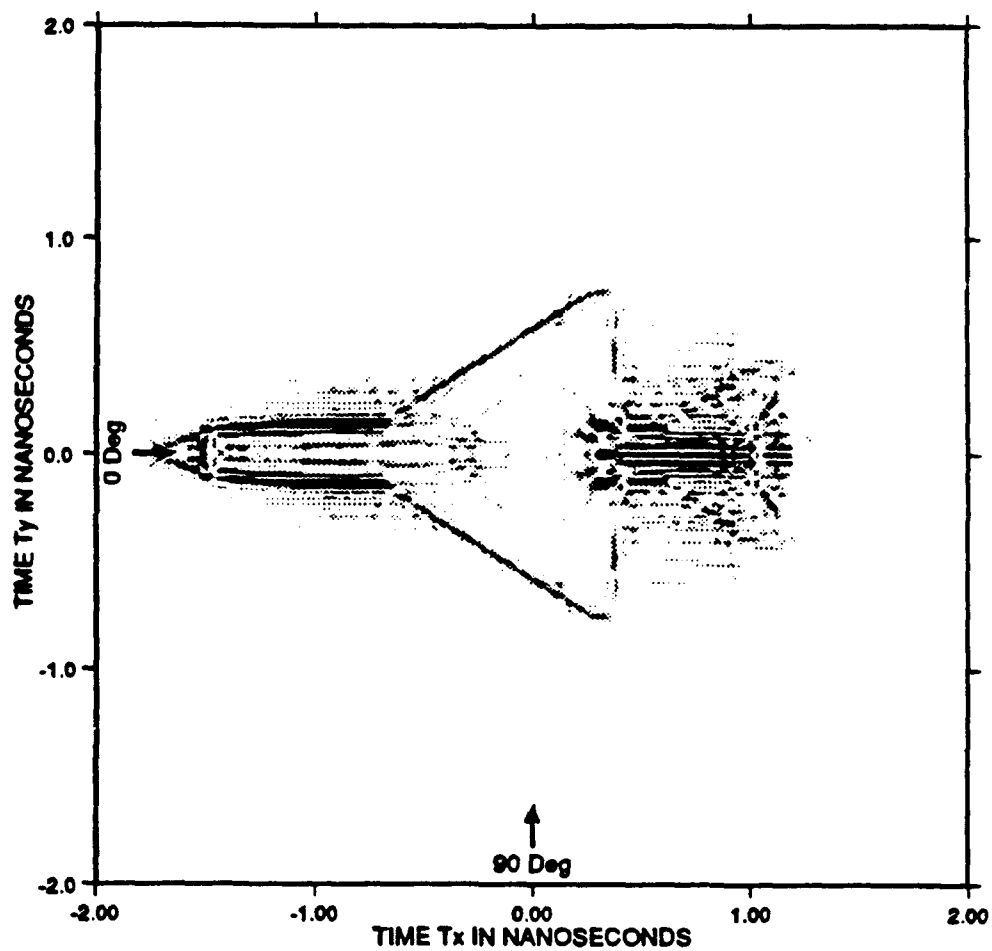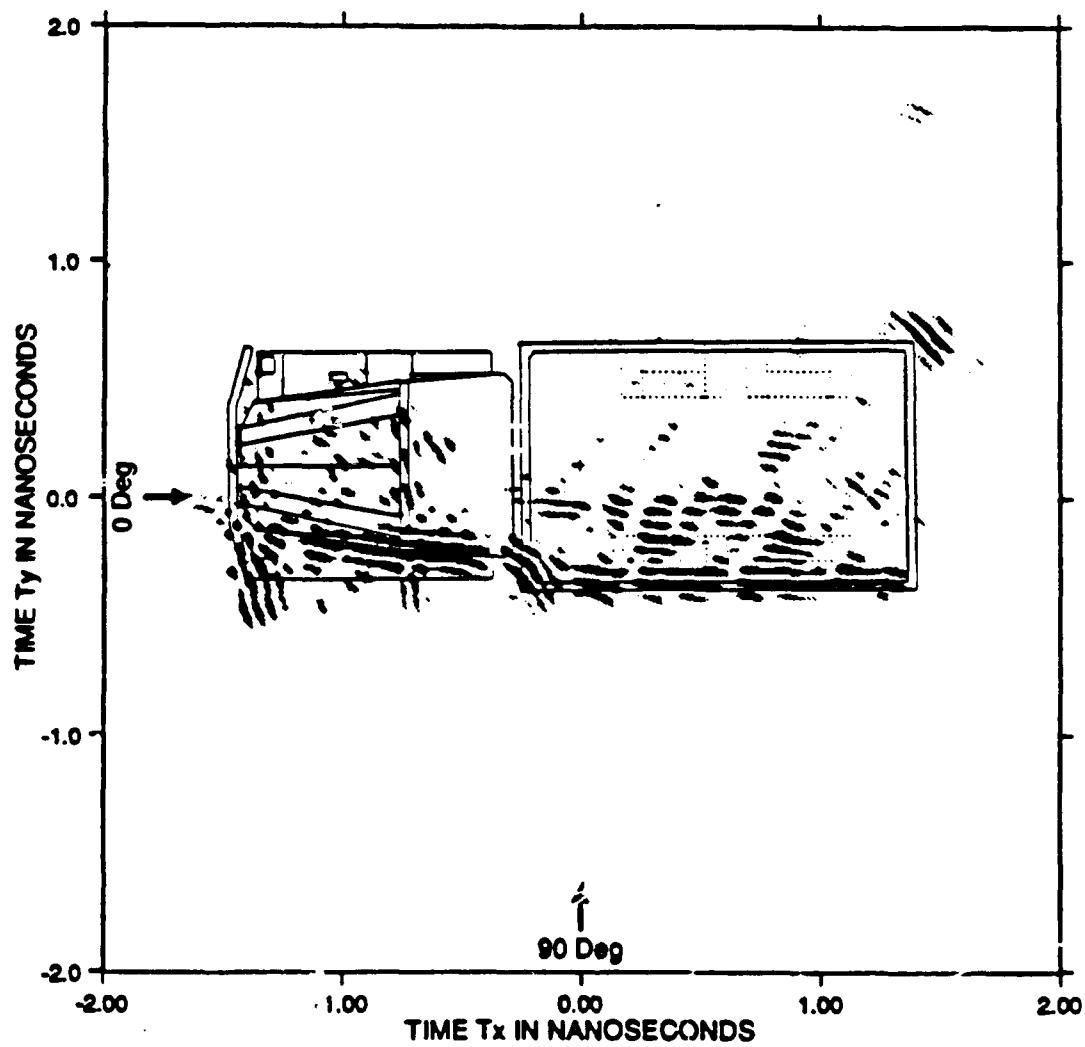
Figure 6.7: Image of model MIG-21 aircraft, 0°(1°)360° HP.

Figure 6.8: Model M35 truck, image and overlay −5°(1°)95° VP.
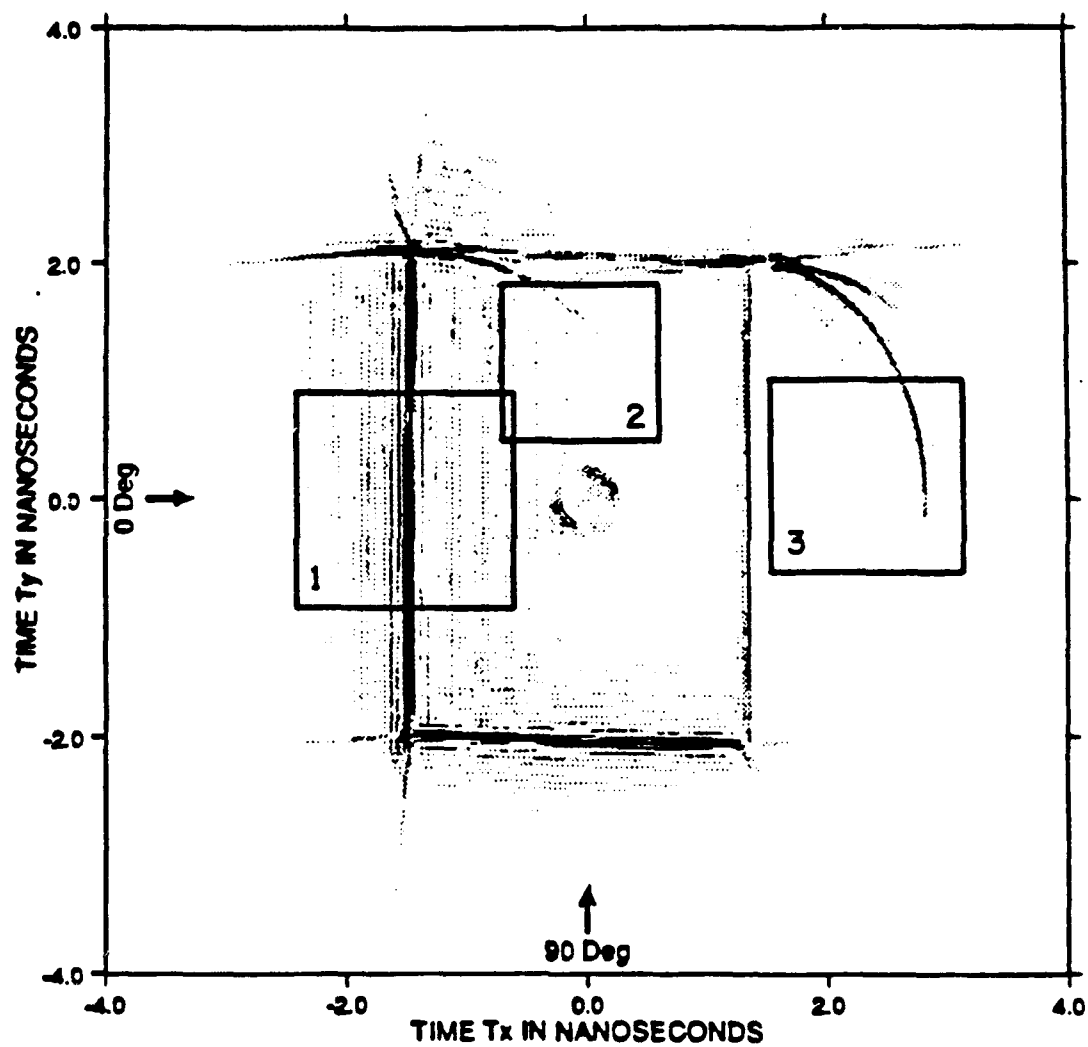
74

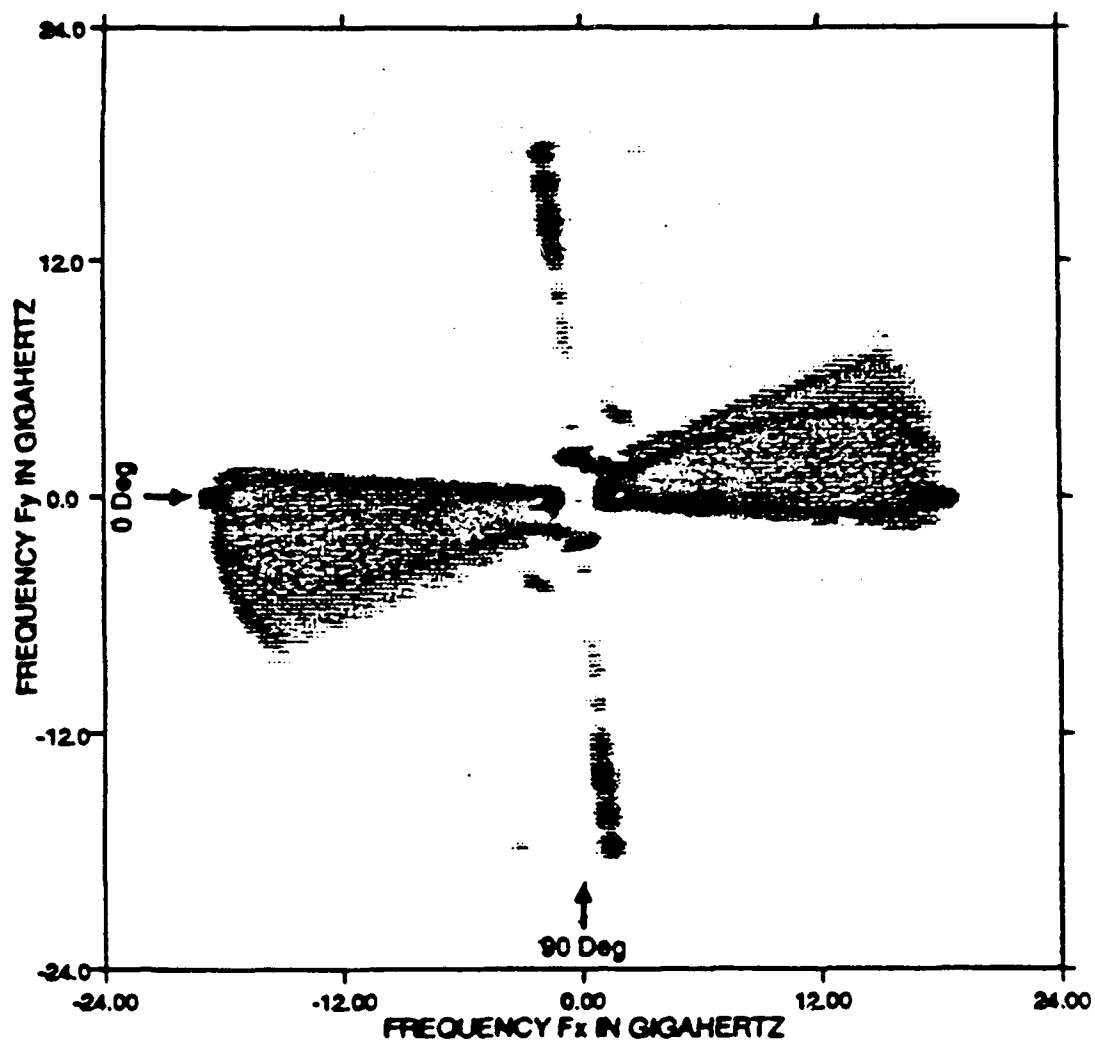Figure 6.9: Image of tilted square plate showing example gates.

Figure 6.10: Frequency/angle response of tip-to-tip diffraction, HP.
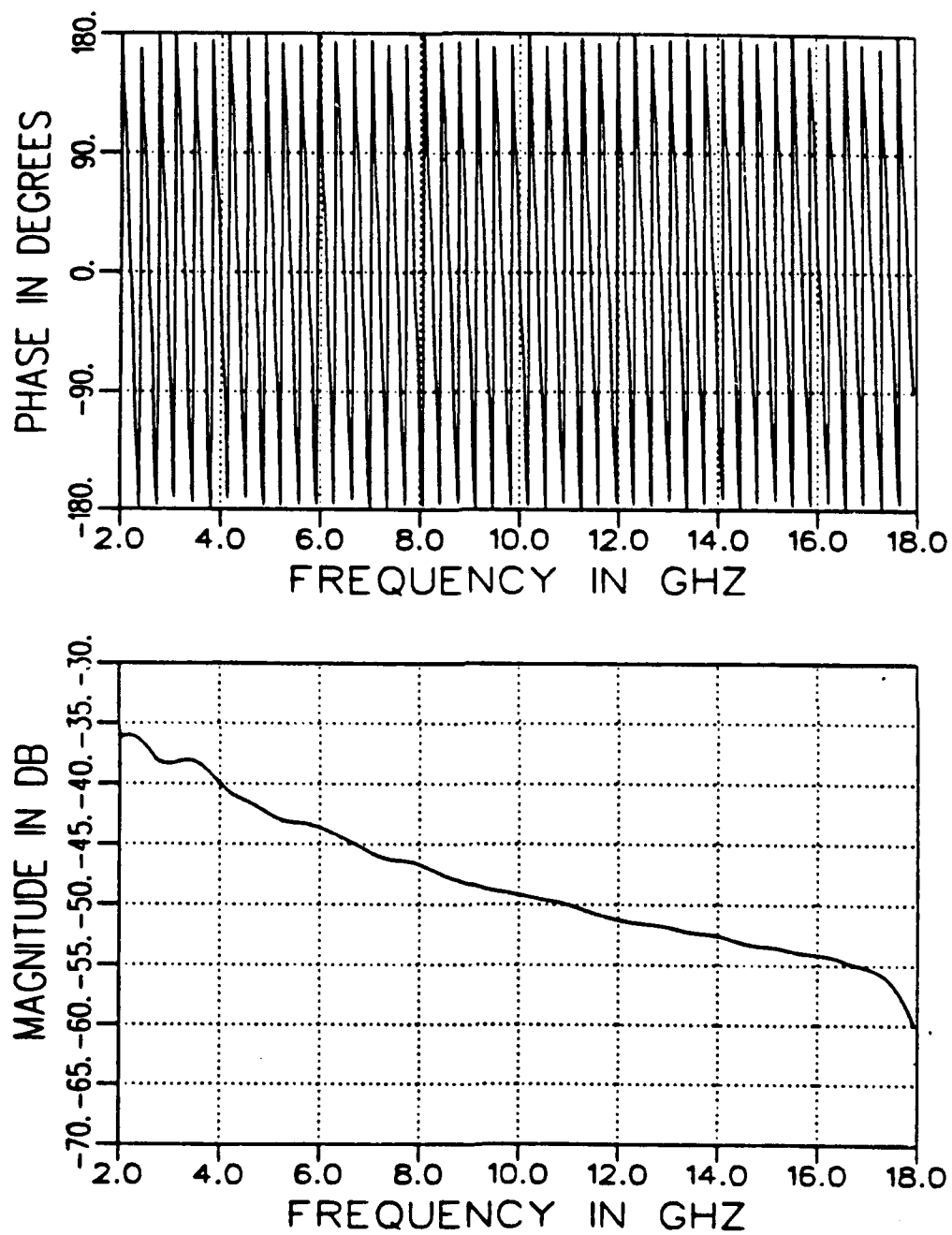
Figure 6.11: Frequency response of tip-to-tip diffraction at 20° azimuth, HP.

- Polarimetric data show it is the individual scattering mechanisms which have a polarization response which is simple enough to be predicted beyond the range of measurements, or to be interpolated between measurements.

- When many of these polarimetric scattering mechanisms are added, and possibly interact with each other, the composite behavior of the target can become quite complex.

Chapter 7

Calibration and Performance of Radar Signature Measurement Systems

7.1 Goals

Included in the work statement on this project were measurements of simple targets such as corner reflectors, dihedrals, and other simple reflectors. Such data not only give information on simple scattering mechanisms, but also are the basis for using such targets as secondary calibration standards for polarimetric scattering measurements. These measurements have been performed in conjunction with a study on Ultra-Wide Band scattering range calibration, and a separate technical report has been written on this subject.

7.2 Method

The report which contains this work is entitled "An Assessment of Three Experimental Scattering Measurement Systems Operating Below 2 GHz," by John S. Gwynne, Report 721198-3. The report discusses the types of measurement errors encountered in three separate RCS systems, and then describes calibration and range evaluation techniques appropriate for all cases. The report concludes with some illustrative measurements of several targets on the three systems.

The three ranges studied were:

- The Ohio State University "Big Ear" Radio Telescope, used as a compact radar scattering range (OSURT)

- The Parallel Plate Transmission Line scattering range at the Ohio State University ElectroScience Laboratory (PPTL)

- The indoor Compact Range at the Ohio State University ElectroScience Laboratory (OSUCR)

Range construction and typical range instrumentation for all three of these systems is discussed in the report. Also described are the most common error sources for each system.

The report focuses on two performance functions which characterize these ranges. The System Transfer Function (SRT) defines the relative amplitude and phase vs. frequency and position in the test zone for an ideal point scatterer. The Calibration Transfer Function (CTF) is the inverse of the SRT, and represents the complex function which when multiplied by the raw data will give calibrated scattering data.

The report contains measured SRT data for all three systems. The technique for measurement is described, and the noise and error sources are described and demonstrated. The calibration flow diagram shown in Figure 7.1 summarizes the process. The results of Figure 7.2 show the benefit of including all of the steps in the calibration process of Figure 7.1. The selection of windowing functions for use in this process is also discussed in detail.

Beyond optimizing the process for system calibration, the calibration target has an effect on calibration accuracy on a real system with noise and clutter. This report discusses the use of spheres, hemispheres, and dihedrals for calibration, and compares their performance features. For example, Figure 7.3 shows a comparison of the CTF measured using a 6-inch dihedral vs. one obtained from a 12-cm-diameter hemisphere

80

CALIBRATION
FLOW DIAGRAM

(1) COLLECTION OF DATA

$\downarrow$

(2) ROUGH TIME GATING OF $\Gamma_C - \Gamma_{CB}$

$\downarrow$

(3) CALCULATION OF THE CTF

$$C = \frac{\sqrt{\sigma_{cal}}}{\Gamma_C - \Gamma_{CB}}$$

$\downarrow$

(4) ROUGH TIME GATING OF $\Gamma_T - \Gamma_{TB}$

$\downarrow$

(5) CALIBRATION OF THE TARGET

$$\sqrt{\sigma} = (\Gamma_T - \Gamma_{TB}) C$$

$\downarrow$

(6) FINAL TIME/FREQUENCY GATING
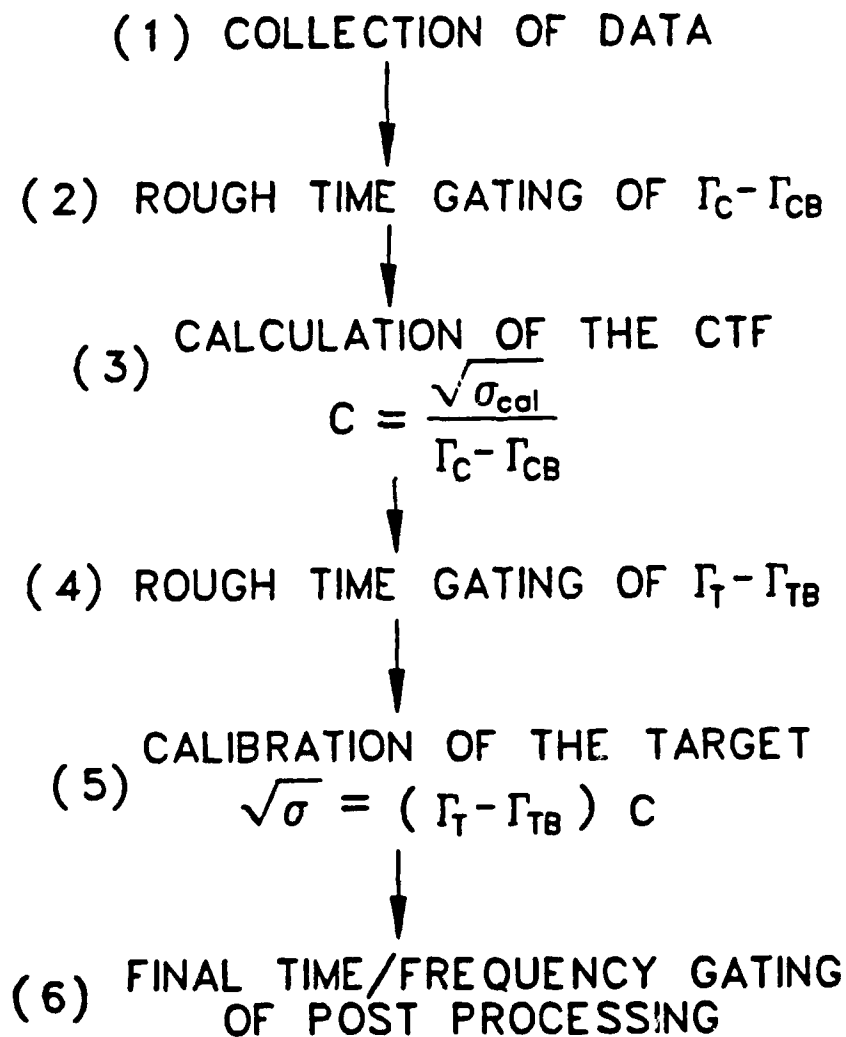OF POST PROCESSING

Figure 7.1: Flow diagram for the calibration of data that has a low signal to noise/clutter ratio.
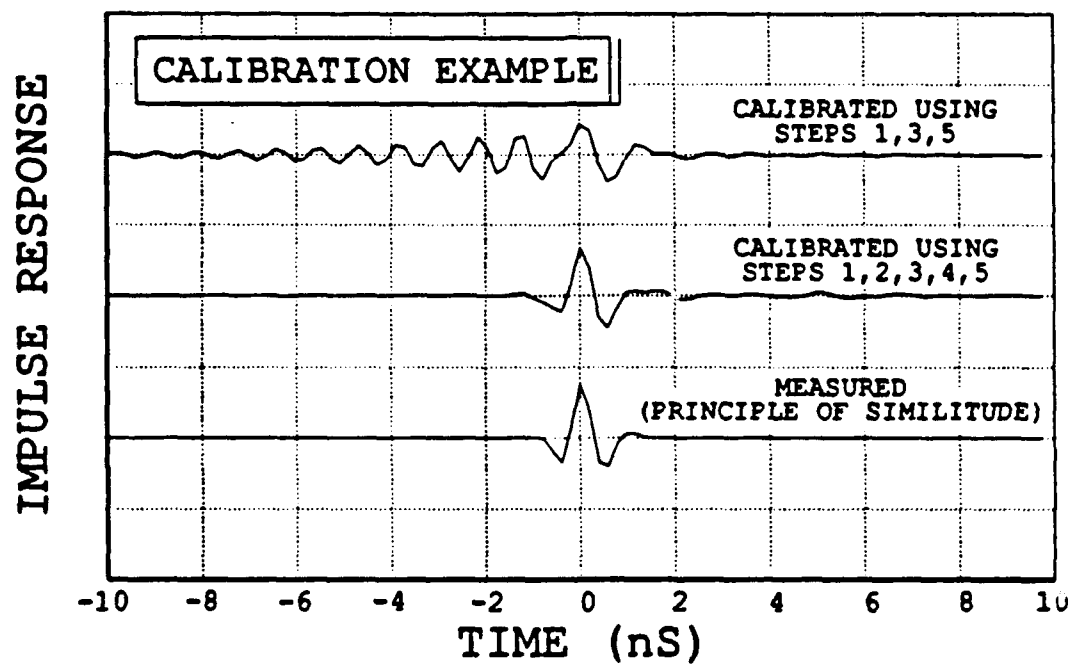
Figure 7.2: Example of the benefits of the additional calibration steps in the time domain.

measurement. As seen in the figure, nulls in the calibration target response create spike artifacts in the CTF frequency response.

Finally, the report presents performance characteristics and target measurement examples for the three ranges. For example, Figure 7.4 shows a waterfall image diagram of cylinder field probing echoes for the OSURT. Error mechanisms and their relative amplitude compared to the desired plane wave beam are easily visible in this image.

Figure 7.5 shows the outline diagram of an inert land mine model which was measured on all three ranges. Figure 7.6 shows its calibrated backscattered echo spectrum at broadside, measured on the three ranges. Figure 7.7 shows its approximate impulse response derived from the measured spectral data. The report describes the factors which cause the slight differences in these data.

7.3 Conclusions

The conclusions section of the report describes the relative strengths and weaknesses of the three measurement systems. It stresses the importance of choosing a calibration target which has no pattern or frequency response nulls, and also has an accepted accurate theoretical solution for its response signature. The section also discusses improvements which could be made to the ranges and to their calibration targets and process.
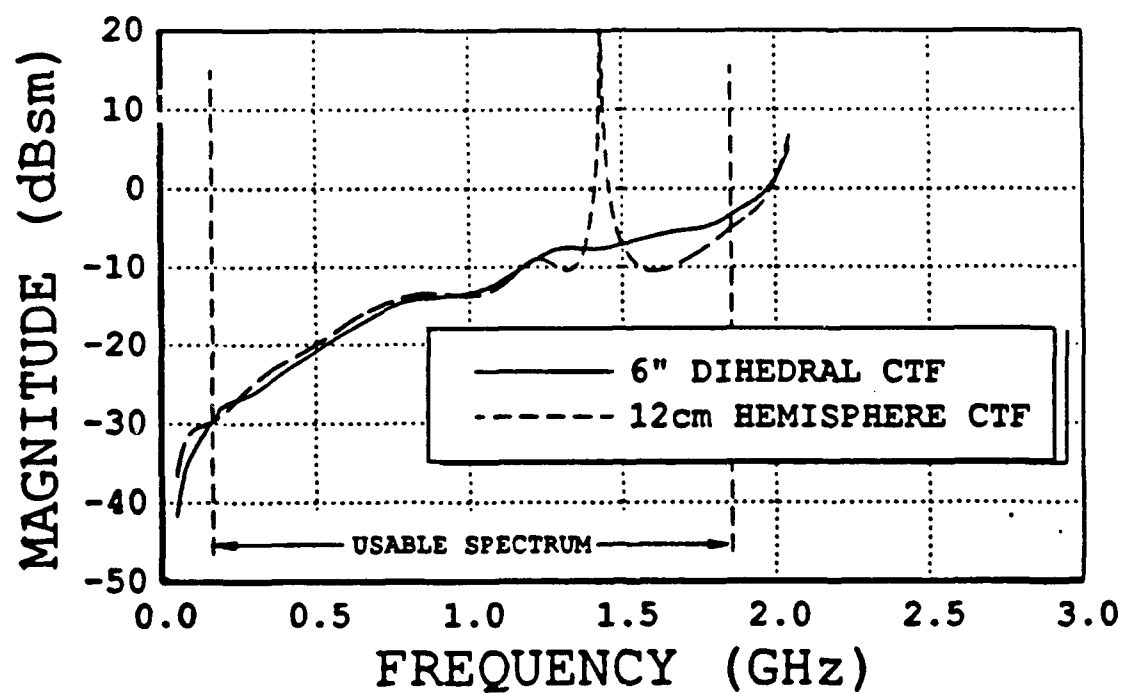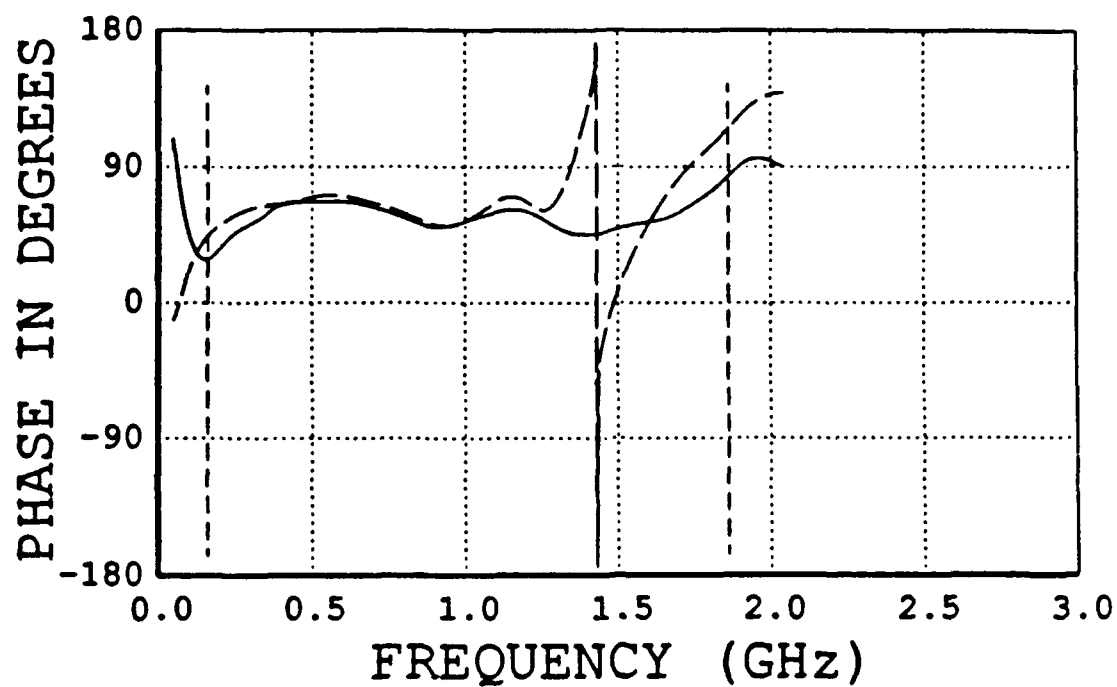
Figure 7.3: Comparison of the measured CTF of the PPTL range obtained from the 6″ dihedral.
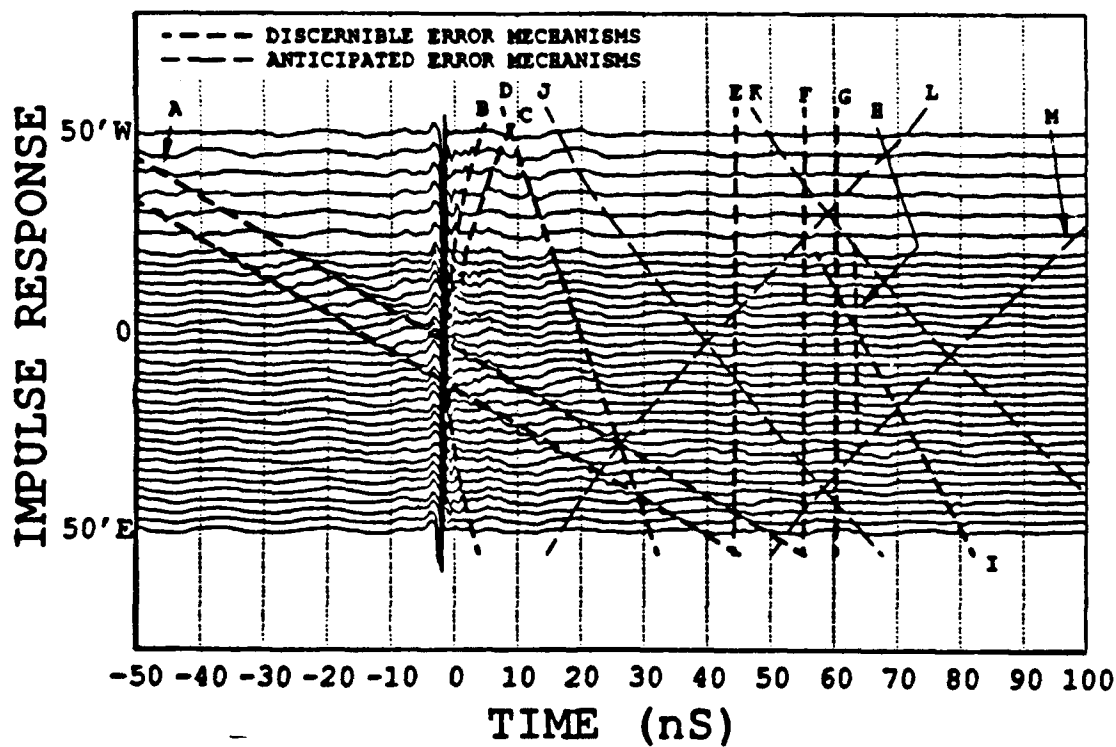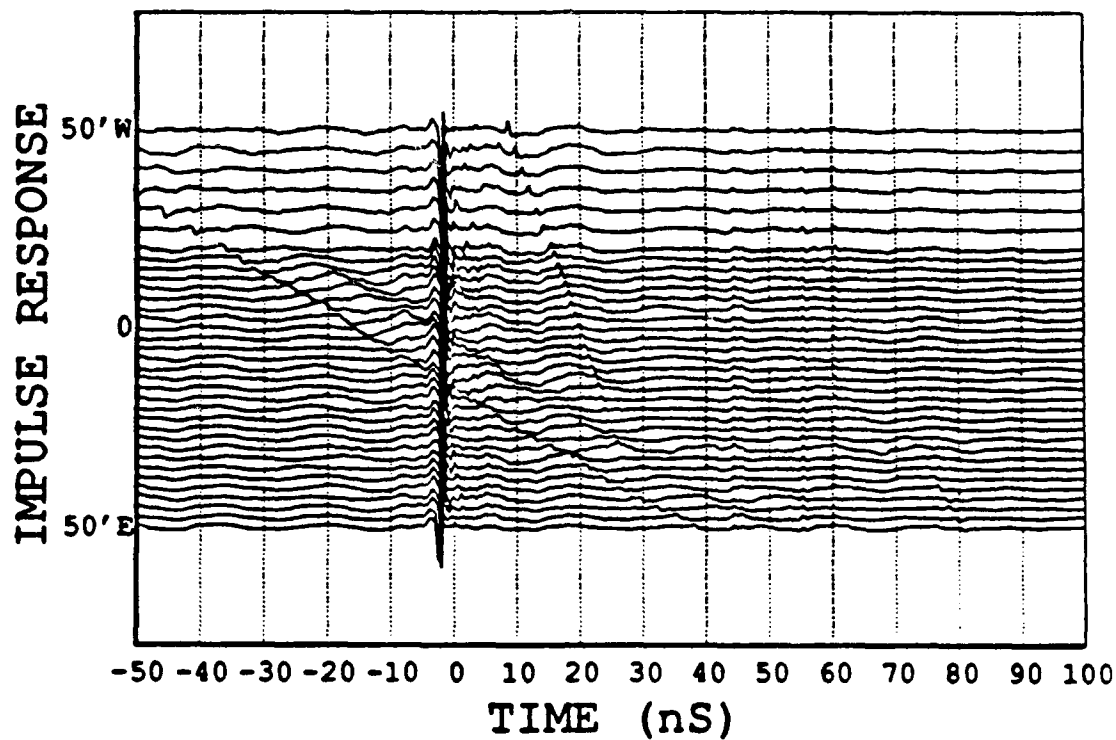
Figure 7.4: Waterfall diagram of cylinder field probing results for the OSURT.
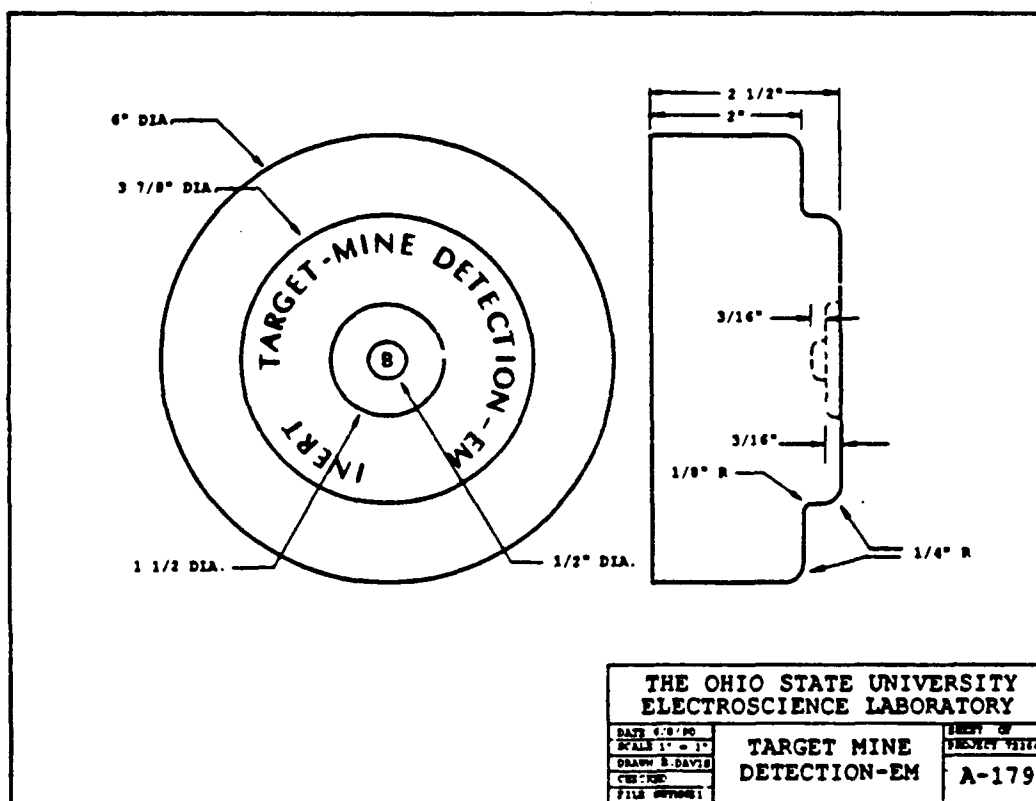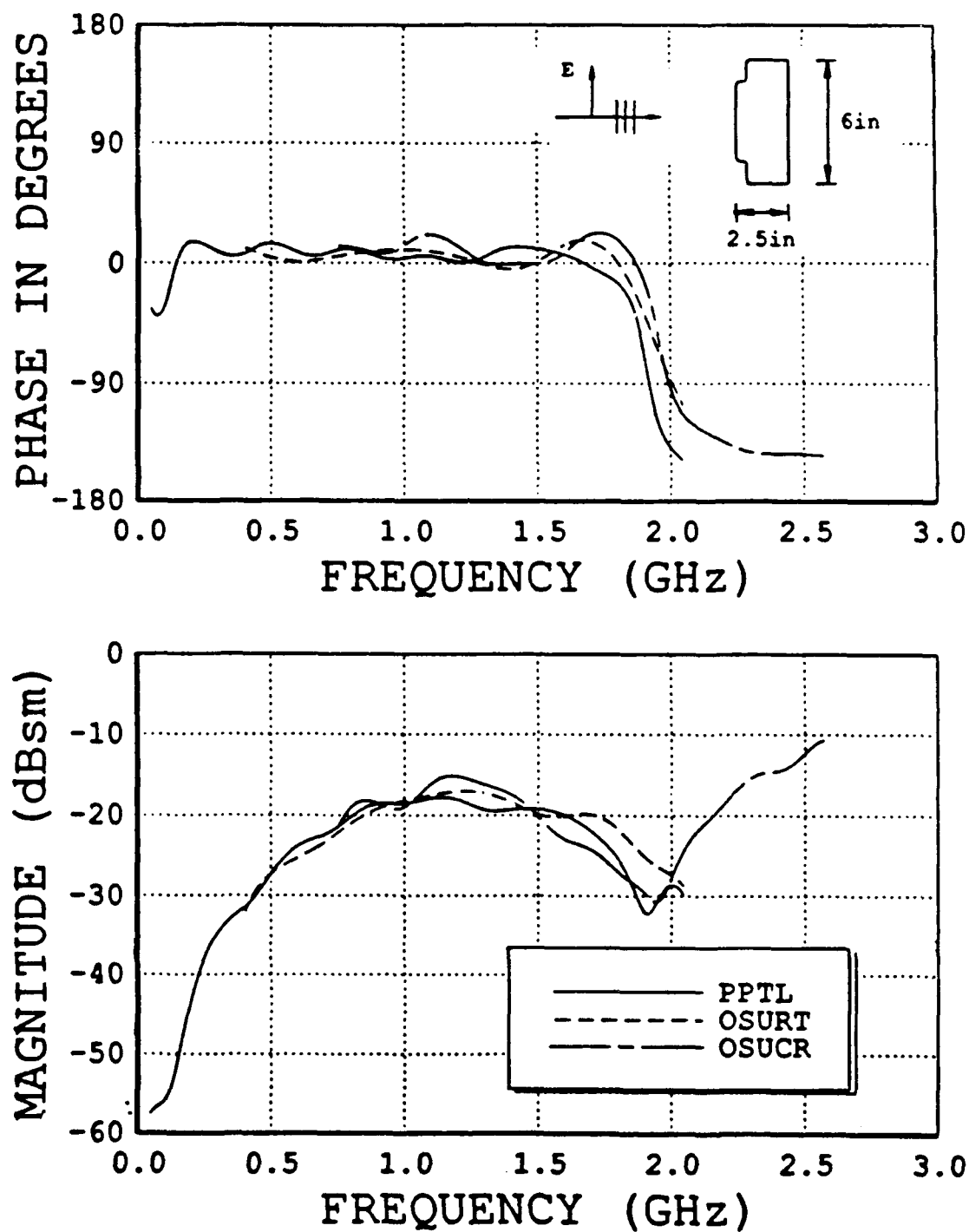
Figure 7.5: Outline drawing of the 6″ mine.

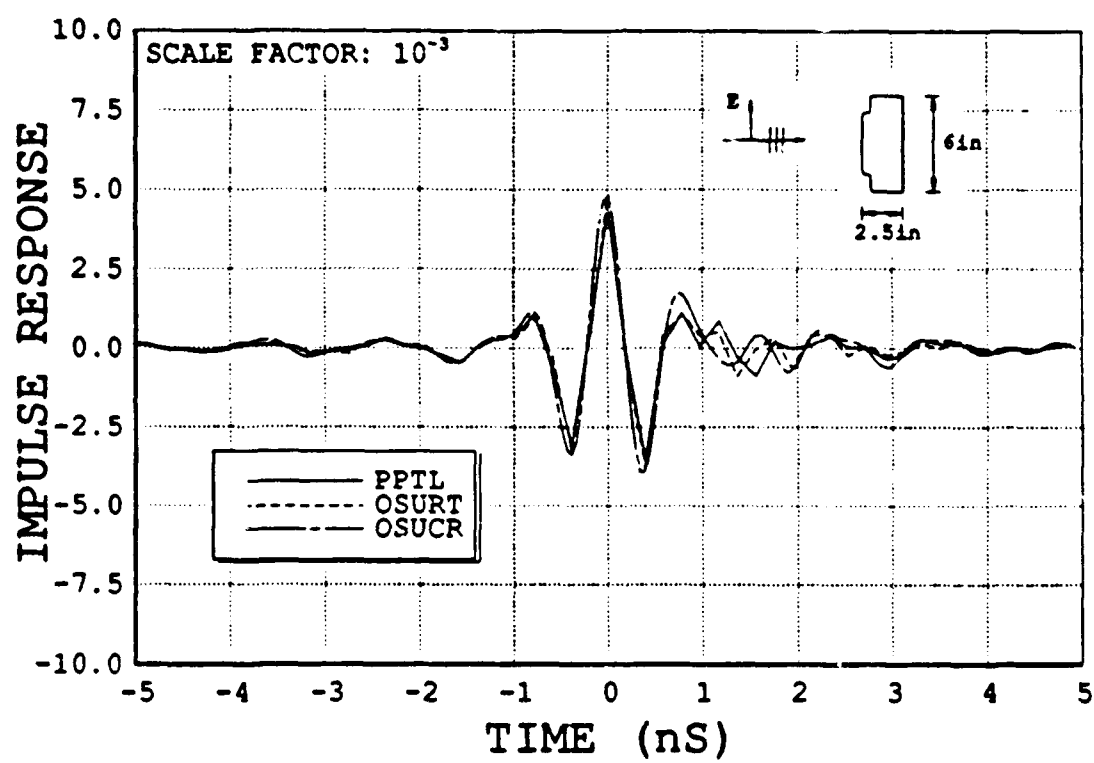Figure 7.6: Measurement example: 6″ mine at broadside-frequency domain.

Figure 7.7: Measurement example: 6″ mine at broadside-time domain.

Chapter 8

Conclusions

This research effort has sought to investigate electromagnetic scattering phenomenology over a wide range of frequencies and polarizations to enhance performance of SAR ground imaging radars for automatic target detection/classification. The effort has involved closely coordinated theoretical and experimental studies, and included expanded data base measurements not envisioned in the original contract work statement.

Analytical results include the following:

- Theoretical models for dihedral scattering signatures have been completed.

- Extensions of the dihedral models have been accomplished for the top-hat, bi-cone, "cake pan," bruderhedral, and "donut" shapes.

- An improved far zone diffraction coefficient for a vertex of an angular sector has been developed.

- Edge wave and double diffraction mechanisms across a plate have been studied to determine their frequency and pattern behavior in images.

- Preliminary double diffraction coefficients for non-coplanar skewed edges necessary for the trihedral analysis have been developed.

Experimental results include the following:

- UWB polarimetric scattering signatures of real and scale model targets were measured.

- UWB diagnostic backscattering images were generated from measured data for both canonic and realistic targets.

- A UWB calibration procedure was developed, and was developed on three different systems.

- A data processing technique to extract the frequency spectrum and pattern behavior of individual scattering centers from UWB diagnostic images was developed and demonstrated.

- The speed, dynamic range, and accuracy of the "Big Ear" compact range radar system were improved. The system was useful for targets as large as 70 ft. long.

In conclusion, the studies have shown that there do exist scattering mechanisms which are strongly related to target geometry and hence are robust over polarization, frequency, and look angle. We have established the procedures for determining a wide variety of such scattering centers for a realistic object, either analytically or experimentally. We recommend that these scattering centers be prime candidates for target discrimination research in the future. We also recommend further studies of the behavior of such mechanisms for targets in foliage and other complex clutter-limited situations.

References

[1] N. Akhter and R. J. Marhefka, "Far zone scattering from rectangular and triangular dihedral in the principal plane," Technical Report 721198-1, The Ohio State University ElectroScience Laboratory, Department of Electrical Engineering, Feb. 1989.

[2] W. Ebihara and R. J. Marhefka, "Bistatic scattering from a cone frustum," Technical Report 716148-16, The Ohio State University ElectroScience Laboratory, Department of Electrical Engineering, Aug. 1986.

[3] K. C. Chiang and R. J. Marhefka, "Bistatic scattering from a finite circular cylinder," Technical Report 714614-4, The Ohio State University ElectroScience Laboratory, Department of Electrical Engineering, July 1984.

[4] R. Tiberio, G. Manara, G. Pelosi, and R. Kouyoumjian, "High-frequency electromagnetic scattering of plane waves from double wedges," *IEEE Trans. Antennas Propagat.*, vol. AP-37, pp. 1172–1180, Sept. 1989.

[5] R. Satterwhite, "Diffraction by a quarter plane, the exact solution, and some numerical results," *IEEE Trans. Antennas Propagat.*, vol. AP-22, pp. 500–503, May 1974.

[6] T. J. Brinkley and R. J. Marhefka, "Comparison of methods for far zone scattering from a flat plate and cube," *Applied Computational Electromagnetics Society*, vol. 3, pp. 57–78, Fall 1988.

[7] L. P. Ivrissimtzis and R. J. Marhefka, "A uniform ray approximation of the scattering by polyhedral structures including higher order terms." Accepted for publication, *IEEE Trans. Antennas Propagat.*

[8] W. B. Gordon, "Far-field approximations to the Kirchoff-Helmholtz representations of scattered fields," *IEEE Trans. Antennas Propagat.*, pp. 590–592, July 1975.

[9] O. M. Buyukdura, R. J. Marhefka, and W. Ebihara, "Radar cross-section studies, Phase III," Technical Report 716622-1, The Ohio State University Electro-

Science Laboratory, Department of Electrical Engineering, Apr. 1986. Prepared under Contract No. N0429A-84-C-0363 for Pacific Missile Test Center.

[10] T. J. Brinkley and R. J. Marhefka, "Far zone bistatic scattering from flat plates," Technical Report 718295-8, The Ohio State University ElectroScience Laboratory, Department of Electrical Engineering, July 1988. Prepared under Contract No. F33615-86-K-1023 for Wright Patterson Air Force Base.

[11] T. J. Brinkley and R. J. Marhefka, "Current near the vertex of a perfectly conducting angular sector." Submitted for publication to *IEEE Trans. Antennas Propagat.*

[12] L. P. Ivrissimtzis, *High Frequency Electromagnetic Scattering by Polyhedral Structures.* Ph.D. dissertation, The Ohio State University, Department of Electrical Engineering, 1990.

[13] W. J. Leeper, *Identification of Scattering Mechanisms from Measured Impulse Response Signatures of Several Conducting Objects.* The Ohio State University, Department of Electrical Engineering, 1983.

[14] A. K. Dominek, L. Peters, Jr., and W. D. Burnside, "A time domain technique for mechanism extraction," *IEEE Trans. Antennas Propagat.*, vol. AP-35, pp. 305–312, Mar. 1987.

[15] G. Dural, "Polarimetric ISAR imaging to identify basic scattering mechanisms using transient signatures," Technical Report 312884-9, The Ohio State University ElectroScience Laboratory, Department of Electrical Engineering, Dec. 1988.